Università degli Studi di Padova

Head Office: Università degli Studi di Padova
Department of Management and Engineering

Ph.D. Course in

Mechatronics and Product Innovation Engineering

Curriculum: Mechatronics
Series: XXXVIII

Advanced Control and Coordination Methods for Power Electronic Converters in Microgrids

---

Coordinator: Prof. Giulio Timelli
Supervisor: Prof. Tommaso Caldognetto
Co-Supervisor: Dr. Davide Biadene

Ph.D. Student: Andrea Lauri

Abstract

Environmental considerations are driving the development of modern power systems, leading to an increasing presence of renewable energy sources and power electronics converters that interface them with the electrical grid. The inherent variability and unpredictability of renewables motivates their clustering into microgrids, which can provide local energy storage and smart load management. In this scenario, proper control of power converters is crucial to enable the required orchestration of the distributed energy resources.

This dissertation addresses critical challenges in terms of functionalities and power control capabilities of distributed power converters, which form the basis of the effective integration of distributed energy resources. Its contributions can be conceptually divided into two parts: the first one tackles classic limitations of grid-forming converters in terms of control flexibility compared to their grid-following counterparts; the second one studies the coordination of multiple converters in a microgrid, leveraging the newly unlocked degrees of freedom to improve its operation and to provide ancillary services to the upstream grid.

More specifically, in the first part two novel control approaches based on droop-control are proposed to provide grid-forming converters with unbalanced operation capabilities, allowing the compensation of non-balanced load conditions or the tracking of unbalanced references. A low-voltage ride through technique is then proposed for flexible grid-forming converters that enables them to withstand balanced and unbalanced faults, still retaining the introduced enhanced control capabilities.

In the second part a coordination algorithm is proposed for converters to optimize their operation in microgrid scenarios. This method minimizes the power losses due to reactive and unbalanced currents, optionally offering their total compensation at the point of common coupling with the upstream grid. The method perfectly integrates with energy managing techniques, as it does not modify the active power exchange. Finally, an experimental setup is developed for the validation of microgrid control methods. The setup employs 10 power electronic devices and a communication network to offer a holistic validation approach, encompassing hardware aspects and all the control layers. It is used to experimentally validate the microgrid coordination approach while integrating the developed local control techniques for the converters.

As power systems undergo fundamental transformation toward power-electronics-dominated, highly distributed architectures, the conducted studies aim to provide critical building blocks for more resilient, efficient, and economically viable distributed energy systems that will help achieve the electrification and environmental goals driving modern power grid development.

Acknowledgments

Despite being the one bearing responsibility for this dissertation and its content, its completion would have been impossible without the invaluable help of people who, in one way or another, walked this path with me and those who supported me along the way.

I would like to begin by thanking my supervisors Prof. Tommaso Caldognetto and Dr. Davide Biadene. As they wisely guided me along this journey, I could benefit from their great support and advice. I owe them my academic achievements, as well as my scientific maturity. I would like to extend this gratitude to *the entire* Power Electronics Group at the University of Padova, particularly to Prof. Paolo Mattavelli for involving me in engaging industry collaborations that allowed me to apply my knowledge while gaining valuable new experience.

I want to express my gratitude to Prof. Ruggero Carli, Mohammed Abdelm Messilem, Xiangchen Zheng, and Diego Rigato for the fruitful and enjoyable collaborations.

I would like to thank the terrific team at Imperix, particularly Simon Strobl, Dr. Nicolas Cherix, and Dr. Simon Delalay. My 6 months research period in their headquarters allowed me to bring my research contributions together in an experimental setup, encompassing all aspects of my research. More importantly, I could benefit from the assistance and mentorship of great colleagues, always open to very stimulating discussions and eager to provide support.

A heartfelt thank you to everyone who has been a colleague of mine in these years for the invaluable memories we crafted. In particular, I would like to thank Andrea Petucco, Roberto Losco, Andrea Zilio, and Massimiliano Bertoni for the warm welcome since day one. Saverio Rigon, Ismaele De Martin, Prof. Fabio Tinazzi, Alessandro Vaccaro, Ezio Gallo, Lazar Stojanović, Ružica Cvetanović, Filip Cvejić, Michele Darisi, Diego Rigato, and Alberto Bregantin for all the adventures we lived together. I also extend my gratitude to all other colleagues who, though not mentioned by name, contributed to making this journey memorable and enriching.

I want to express my gratitude to my dear friends Alessandro, Damiano, Daniela, and Enrico for having been there, always.

I'm grateful to Laura and Simone for their support, advisory and personal.

I'm grateful to my family and relatives for their patience and support throughout my chaotic life, which made everything possible.

I extend my heartfelt thanks to my brother Davide for being a source of inspiration in pursuing what is good, always. I'm thankful to him for inspiring the parts of myself I express with the greatest pride.

Most importantly, I wish to thank Chiara, for having listened to almost all of my presentations, for unconditionally accepting with immense patience her role as a "debug duck", for enduring this journey alongside her own, and for everything else that, if written down, would double the size of this dissertation.

Vicenza, September 2025
Andrea Lauri

Contents

Glossary

DC-ADMM distributed-consensus alternating-direction method of multipliers

EPC electronic power converter

FRT fault ride-through

GFL grid-following
GFM grid-forming

LVRT low-voltage ride-through

PCC point of common coupling
PoC point of connection
PV photovoltaic

1 Introduction

1.1 Historical Background

The first historical example of an electrical plant was the one illuminating Pearl Street in New York, implemented by Thomas Alva Edison in 1882. After a very short time, many other examples appeared. In Europe, for instance, the first electrical line in Germany appeared a few months later, while in 1883 Italy saw its first AC line in Rome [1]. Unlike other energy sources, which require consumption to be close to production sites due to management and transmission difficulties, electrical energy can be easily transported over long distances. This advantage allowed electric plants to quickly establish electrical energy as the main vector for industrial development.

With the development and improvement of semiconductor devices, in particular their higher-power versions, power electronics devices started to become more and more popular. Nowadays more than 70% of the total electrical energy produced passes through power electronic devices at some point in the generation-to-consumption chain [2].

Currently, the development of power systems is primarily motivated by the need to minimize environmental impact—as visible from Figure 1.1 and Figure 1.2—and the need to accommodate an increasing energy demand [3]. The integration of renewable energy sources, energy storage systems, and electric vehicles all rely heavily on power electronic converters. Furthermore, recent geopolitical tensions are making oil and gas less and less favorable as energy resources, accelerating electrification trends that depend on advanced power electronics solutions.

1.2 Microgrids for Renewable Energy Integration

The integration of renewable energy sources like solar photovoltaic (PV) and wind into power systems presents significant challenges, primarily centered around their inherent variability and unpredictability [4]. Unlike traditional power generation that can be dispatched on demand, solar and wind output fluctuates based on weather conditions, creating supply variability that power systems must accommo-

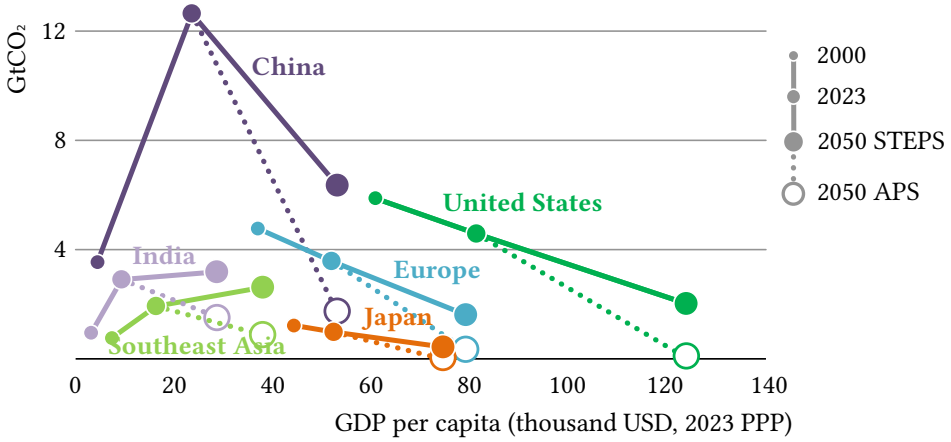

Figure 1.1: CO_2 emissions and GDP per capita in selected countries/regions in the Stated Policies Scenario (STEPS) and Announced Pledges Scenario (APS) [3].

date. While traditional generators have historically managed demand variability, the introduction of renewable energy sources adds a new dimension of complexity by introducing supply-side uncertainty. The timing mismatch between renewable energy production and electricity demand further complicates grid management, as the peak generation may not coincide with high-consumption time windows [5].

A way to tackle these challenges is microgrids: *a group of distributed energy resources, including renewable energy sources and energy storage systems, plus loads that operate locally as a single controllable entity* [6]. By enabling local energy storage and smart load management, microgrids can smooth out the intermittency of solar and wind generation by storing excess energy during peak production periods and releasing it during low production or high demand periods, effectively decoupling generation from consumption timing. Additionally, microgrids can provide valuable grid services [7, 8] such as demand response capabilities [9], voltage regulation and unbalance mitigation [10, 11], and frequency support to the broader power system, while reducing transmission losses and grid congestion. Their ability to operate in islanded mode during adverse grid conditions also enhances overall system resilience, ensuring the continuity of the electrical service.

1.3 Main Challenges and Contribution

This dissertation focuses on advancing the functionalities and control capabilities of distributed power converters to unlock additional services and enhanced contributions that distributed energy resources can offer to modern power systems.

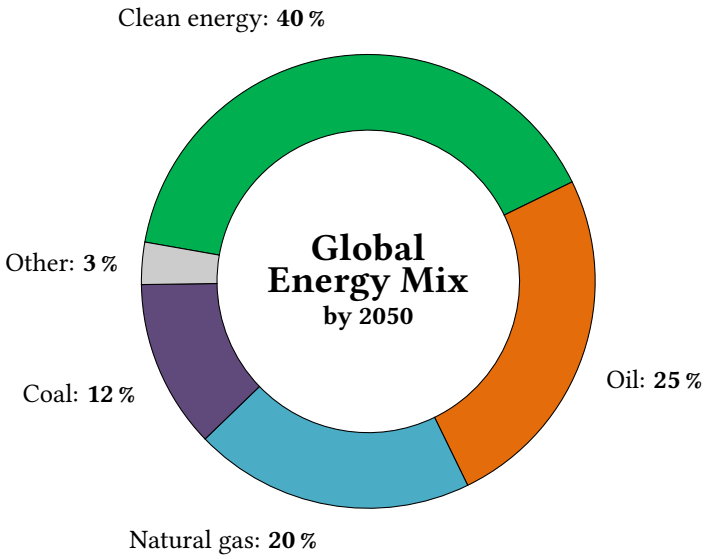

Figure 1.2: Expected global energy mix by 2050. Data from [3].

The first part regarads the control of three-phase grid-forming (GFM) inverters, addressing the limitations in flexible control capabilities that they present with respect to grid-following (GFL) converters. The second part focuses on coordination methods for power converters operating in a microgrid scenario, leveraging on degrees of freedom that are typically not used in GFL converters, as well as newly unlocked ones for GFM converters, thanks to the control techniques developed in the first part. The specific challenges addressed in each part are outlined below, together with the proposed approaches and references to their detailed discussion in relevant sections.

Flexible Control for Grid-Forming Converters

GFM converters typically lack the flexibility of their GFL counterparts. Being usually current-controlled, GFL converters allow for straightforward implementations of features such as flexible power control, unbalance compensation, and harmonic compensation. The implementation of the same features on GFM converters requires non-trivial control approaches to integrate them with islanded operation capability. While an implementation for each of these features was present in the literature, the harmonious integration of these into a single control approach, like in GFL, was missing.

This challenge has been addressed proposing two control techniques [12, 13],

discussed in Chapter 2 and Chapter 3, based on droop control, a technique for GFM converters that inherently supports islanded operation. These methods allow the converters to flexibly control the output quantities, allowing phase by phase power control with the former approach, and unbalanced current injection with the latter.

Fault Ride-Through of Per-Phase Controlled Converters

There are times in which the grid is subject to adverse conditions, and its voltage may abruptly change, presenting sags or phase jumps. These events pose a limited threat to GFL converters, as their regulator typically has full control of their output currents. Conversely, GFM converters behave as voltage sources behind a small impedance: they can safely operate as long as their internal voltage reference is similar to the voltage at their point of connection. How the internal voltage reference is synchronized depends on the particular GFM technique, but it's typically the output active power that acts as a phase detector. During grid adverse conditions, the output current of the GFM converter needs to be limited to avoid the voltage controller requiring unsafe current levels. However, this also limits converter output power, possibly leading to loss of synchronization and transient instability. Fault ride-through (FRT) methods present in the literature are not directly applicable to converters controlled as in Chapter 2.

This challenge has been addressed by leveraging the per-phase control capability of the controller presented in Chapter 2, proposing the method discussed in Chapter 4 that features a straightforward FRT technique to safely limit the converter currents in both balanced and unbalanced faults, avoiding transient instability [14].

Optimization of Microgrid Operation by Converters Coordination

Methods such as the ones proposed in Chapter 2 and Chapter 3 provide GFM converters with control capabilities that were previously exclusively available on GFL converters, allowing GFM to participate in ancillary services such as unbalance and harmonic compensation. Microgrid optimization methods that were present in the literature were focusing either on energy-exchange related aspects, which are not applicable in unbalance compensation, or disregarding the power losses due to converter operating conditions. Indeed, converter power losses vary as different active power, reactive power, or unbalanced current levels are injected.

To address this challenge, a coordination method is proposed in Chapter 5, that leverages on positive, negative, and zero sequence current injection to minimize the power losses due to reactive and unbalanced currents in a microgrid [15]. This method optionally allows for the balancing of the currents at the point of common

coupling in a microgrid. Finally, this method does not constrain the active power flow, leaving it free for energy-exchange related tasks, such as maximum power-point tracking or demand-response management. For instance, it could be used together with other microgrid control methods that regulate the active power flow.

Validation of Microgrid Control Methods

A wide variety of control techniques for converters are present in the literature, enabling important features and provisions for the operation of the converter and for the support of microgrids. The implementation of these features often relies on the interplay between various control loops, and the performance of any of the elements in the control chain may impact the effectiveness of this implementation. Nonetheless, the validation of microgrid-level control approaches is often performed by modeling converters as ideal current or voltage generators, disregarding the impact that the converter control loops may have on the microgrid control method, as well as their impact on parallel operation of converters.

To address this challenge, an experimental testbench has been implemented, illustrated in Chapter 6, that features 10 power electronics devices, 8 of them employing programmable controllers. By using ethernet communication, the setup allows to test arbitrary communication network topologies among converters, eventually with a centralized controller that is made available. This setup is used to test the algorithm proposed in Chapter 5.

Droop-Based Per-Phase Power Controller

2

This chapter describes the operation of a droop-based power controller that is capable of regulating the output power phase by phase, complying with three-phase three-wire systems limitations and supporting islanded (stand-alone) operation. Section 2.2 introduces the basics of active and reactive power flow for both three-phase four-wire and three-phase three-wire systems, highlighting the additional constraint and related reduced control flexibility present in the latter case. The per-phase power control for three-phase three-wire systems proposed herein is then described in Section 2.3, where the operating principles of the three main control loops are described. Section 2.4 shows the experimental validating results, where unbalanced power reference variations and islanded transitions are shown.

2.1 Introduction

Microgrids integrating distributed energy resources connected to the ac grid by means of electronic power converters (EPCs) should support a number of features [7, 16]. The capability of flexibly controlling the exchanged active and reactive power, that is, output power control, and the capability of operating islanded are a couple of important functionalities in scenarios like the one represented in Figure 2.1. Output power control is crucial for the implementation of demand/response and for unbalanced compensation in three-phase systems [9, 17]. Islanded operation is crucial to make the microgrid subsystem resilient against adverse events affecting the main power system [18].

Solutions like the per-phase power control in [19] limited to three-phase four-wires systems allow the control of the output power of grid-connected inverters and also permit their transition to the islanded operation. Considering other relevant solutions described in the literature, such as [20, 21, 22, 23], the per phase-control can harmoniously integrate multiple merits, in terms of: The solution described herein integrates the features indicated above and, in addition, it allows operation in three-phase three-wire systems, where the nuetral connection is absent.

To highlight the features of the presented solution, a comparison with other control approaches is given in Table 2.1. Grid-feeding converters, for example, require the presence of the main grid or, in order to operate in an islanded microgrid,

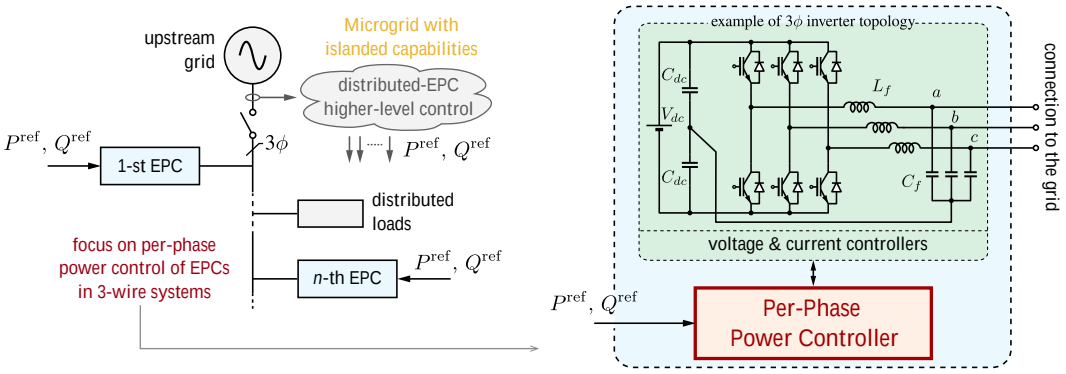

Figure 2.1: Microgrid scenario where distributed EPCs track defined power references and are capable of sustaining the operation of the microgrid in case of disconnection from the upstream grid (i.e., islanding). The control of three-phase three-wire EPCs is considered herein.

of other voltage-forming units [24]. Traditional droop control using P-f and Q-V droop laws allow islanded operation, however total active and reactive power regulation during grid-tied operation is achievable only by control adaptations, as shown in [25] and [26]. In [26], indicated as droop with 3ϕ $P\&Q$ track in Table 2.1, the tracking of the total three-phase inverter output power and the smooth transition to the islanded operation is achieved and shown, however, per-phase power regulation is left unexplored. In fact, it is not possible to independently impose droop laws on each phase: this would lead to different frequencies for each phase of the three-phase system. The approach analyzed herein allows all the functionalities reported above and indicated in Table 2.1, but it was exclusively presented in [19] only restricting to the case of three-phase four-wire networks.

While operation with neutral connection is of significant importance and gives full flexibility for output power control [23, 27, 28, 29], the case *without the neutral connection* is still of interest and can be commonly found in grid-tied applications [30, 31, 32]. For this latter case originally considered herein, independent control of the output active and reactive power phase-by-phase, which results in six variables in total, is not possible and only a subset of the output powers can be controlled instead. As shown herein, four variables can be controlled in three-wire systems and exploited, for example, for distributed power balancing or for control needs of local distribution system operators or microgrid controllers [11, 33], as recommended in modern microgrids standards [34].

Table 2.1: Comparison with other approaches

Control kind	islanded operation	grid-tied / island. trans.	three-phase power-tracking	per-phase power-tracking	3ϕ-4w & 3ϕ-3w operation
Grid-following	–	–	+	+	+
Traditional droop	+	+	–	–	+
Droop with 3ϕ $P\&Q$ track	+	+	+	–	+
Per-phase control in [19]	+	+	+	+	–
Technique proposed *herein*	+	+	+	+	+

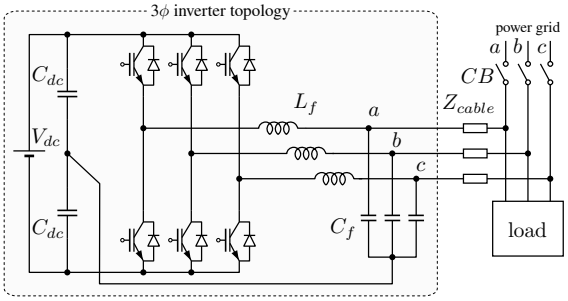

Figure 2.2: EPC connected to a three-phase low-voltage network *without* the neutral connection (i.e., three-phase three-wire connection, 3ϕ-3w) whose per-phase output power control is proposed herein.

2.2 Basics of Power Control

2.2.1 Three-Phase Four-Wires Networks

In an ideal three-phase four-wire system, each of the phases can be considered separately, as the neutral wire provides a return path for the current $i_a + i_b + i_c$. This allows the study of these systems using a single-phase equivalent scheme. Let us consider the power exchange of a single-phase inverter connected to the grid. Be $V_i \angle \varphi_i$ the inverter voltage phasor, $V_g \angle 0$ the grid voltage phasor. Considering the Thevenin model of the inverter connected to the grid, namely, a voltage generator with its equivalent series impedance, the equations for active and reactive power exchange can be derived. Assuming the grid frequency $\omega = 2\pi f$, and inductive interconnection impedances, it is possible to express the transfer of complex power from the inverter to the grid as [35, 36]:

$$\dot{S} = \frac{V_i V_g}{\omega_g L} \sin(\varphi_i) + j \frac{V_g}{\omega_g L} \left[V_i \cos(\varphi_i) - V_g \right] \tag{2.1}$$

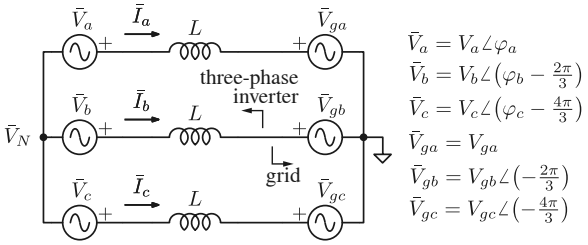

Figure 2.3: Thevenin model of a grid-tied three-phase three-wire inverter.

where $V_i\angle\varphi_i$ and $V_g\angle 0$ are, respectively, the inverter and the grid voltage phasors, and ω_g the grid frequency. Assuming small φ_i and small $\Delta V_i \triangleq V_i - V_g$, by linearizing (2.1) it yields:

$$P \approx \gamma_p \varphi_i; \quad Q_{1\phi} \approx \gamma_q \Delta V_i; \tag{2.2}$$

where $\gamma_p \triangleq \frac{V_g^2}{\omega_g L}$ and $\gamma_q \triangleq \frac{V_g}{\omega_g L}$.

Such relations hold for each of the phases of a three-phase system with neutral connection, that is P_a, P_b, P_c and Q_a, Q_b, Q_c can be computed using (2.1) and (2.2) In this case, the power exchange at one phase does not affect the power exchange at the other phases. This is not the case in three-wire systems, without neutral connection.

2.2.2 Three-Phase Three-Wires Networks

Consider the three-phase three-wire connection of Figure 2.3 with the indicated nomenclature for voltage phasors. In this case full independent power control is not physically possibile. That is, the power exchanged by one generator is affected by the phase and voltage differences imposed by the others, being the neutral point voltage $\bar{V}_N = -(\bar{V}_a + \bar{V}_b + \bar{V}_c)/3$, under the hypothesis of a symmetric grid voltage.

By the linearized relations (2.2) and from the model in Figure 2.3, it yields:

$$S = M \cdot \Theta \tag{2.3}$$

where vectors $S = [P_a,\ P_b,\ P_c,\ Q_a,\ Q_b,\ Q_c]^T$ and $\Theta = [\varphi_a,\ \varphi_b,\ \varphi_c,\ \Delta V_a,\ \Delta V_b,\ \Delta V_c]^T$,

with $\Delta V_x = V_x - V_{gx}$, and M the matrix defined as:

$$M = \frac{1}{6}\begin{bmatrix} 4\gamma_p & \gamma_p & \gamma_p & 0 & \sqrt{3}\gamma_q & -\sqrt{3}\gamma_q \\ \gamma_p & 4\gamma_p & \gamma_p & -\sqrt{3}\gamma_q & 0 & \sqrt{3}\gamma_q \\ \gamma_p & \gamma_p & 4\gamma_p & \sqrt{3}\gamma_q & -\sqrt{3}\gamma_q & 0 \\ 0 & -\sqrt{3}\gamma_p & \sqrt{3}\gamma_p & 4\gamma_q & \gamma_q & \gamma_q \\ \sqrt{3}\gamma_p & 0 & -\sqrt{3}\gamma_p & \gamma_q & 4\gamma_q & \gamma_q \\ -\sqrt{3}\gamma_p & \sqrt{3}\gamma_p & 0 & \gamma_q & \gamma_q & 4\gamma_q \end{bmatrix} \tag{2.4}$$

The rank of $M \in \mathbb{R}^{6\times 6}$ is 4, that is, only four variables can be arbitrarily regulated, whilst it is not possible to simultaneously control the total six active and reactive powers for phases a, b, and c as in case of presence of the neutral connection [19]. A possibile choice of variables to be controlled for output power tracking may be P_a, P_b, Q_a, Q_b, or, equivalently, P_a, P_b, P_c, $Q_{3\phi} = \sum Q_x$. This latter option is considered herein, yielding:

$$\begin{bmatrix} P_a \\ P_b \\ P_c \\ Q_{3\phi} \end{bmatrix} = \frac{1}{6}\begin{bmatrix} 4\gamma_p & \gamma_p & \gamma_p & 0 \\ \gamma_p & 4\gamma_p & \gamma_p & 0 \\ \gamma_p & \gamma_p & 4\gamma_p & 0 \\ 0 & 0 & 0 & 18\gamma_q \end{bmatrix} \cdot \begin{bmatrix} \varphi_a \\ \varphi_b \\ \varphi_c \\ \Delta V \end{bmatrix} \tag{2.5}$$

To avoid control actions related to the homopolar components, which are not controlled by the approach, such components can be removed by processing the voltage measurements with a decoupling matrix [e.g., like the one used in the following in (2.9)].

2.3 Per-Phase Power Control in Three-Phase Three-Wires Systems

The block diagram of the proposed controller is displayed in Figure 2.4. On top, a P-f droop relation processes the total three-phase power $P_{3\phi}$ exchanged at the inverter output and provides the phase $\varphi_{3\phi}$, which is the integral of the angular frequency given by the droop characteristic:

$$\omega^* = \omega_0 + k_{p,3\phi}\left(P^*_{3\phi} - P_{3\phi}\right) \tag{2.6}$$

In this way, the droop controlled-converter can synchronize to the grid voltage, keeping the known synchronization characteristics of the P-f droop, as shown, for

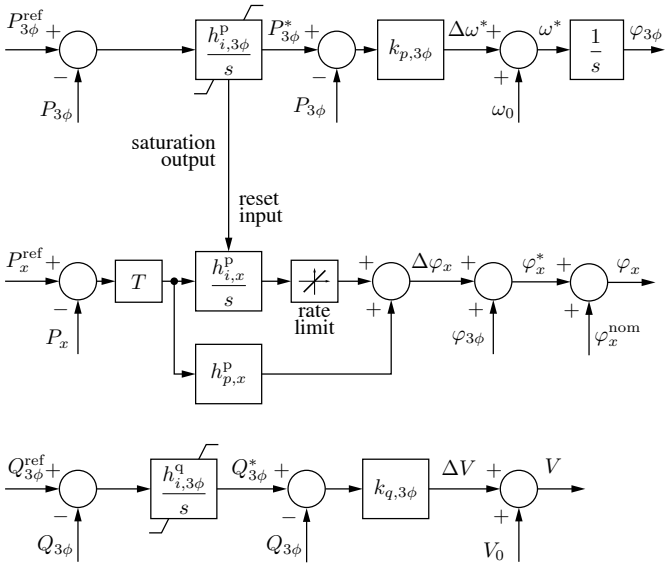

Figure 2.4: Per-phase power controller. The top, synchronization branch provides a reference angle $\varphi_{3\phi}$ to the three phases, represented by the generic symbol x (i.e., a, b, c). The angle and amplitude of each phase are adjusted for per-phase power control. The resulting references $V \sin \varphi_x$ are given to EPC current and voltage regulators (zero-level control) for output voltage control.

example, in [37]. The top branch in Figure 2.4 is referred to as synchronization branch in the following. Then, two different behaviors establish considering grid-connected and islanded operation.

2.3.1 Grid-Connected Operation

While grid-connected, output power tracking is possible due to the presence of the main grid [38]. The total $P^*_{3\phi}$ is adjusted by a three-phase power regulator:

$$H^{\mathrm{p}}_{3\phi}(s) = \frac{h^{\mathrm{p}}_{i,3\phi}}{s} \tag{2.7}$$

whose output $P^*_{3\phi}$ modifies the total three-phase output power of the inverter, by shifting the droop characteristic (2.6).

To achieve output power tracking of the controllable quantities P_a, P_b, P_c, $Q_{3\phi}$, the obtained $\varphi_{3\phi}$ is then adjusted phase-by-phase as displayed by the central blocks in Figure 2.4 referring to the generic x-th phase. Here, a proportional-integral controller, denoted as:

$$H^{\mathrm{p}}_{x}(s) = h^{\mathrm{p}}_{p,x} + \frac{h^{\mathrm{p}}_{i,x}}{s} \tag{2.8}$$

produces the phase shift $\Delta\varphi_x$ that adds to the instantaneous three-phase angle $\varphi_{3\phi}$ and allows the phase power P_x to follow the respective reference power P^{ref}_x during grid-tied operation. In order to decouple balanced active power control and unbalanced power control, making the first component relevant only to the top, synchronization loop, it is possibile to use a decoupling matrix T to remove the balanced terms from the per-phase control loop. The matrix can be defined as:

$$T = \begin{bmatrix} 2/3 & -1/3 & -1/3 \\ -1/3 & 2/3 & -1/3 \\ -1/3 & -1/3 & 2/3 \end{bmatrix} \tag{2.9}$$

Finally, the total delivered output reactive power is adjusted by acting on the amplitude of the generated three-phase voltages, using the regulator:

$$H^{\mathrm{q}}_{3\phi}(s) = \frac{h^{\mathrm{q}}_{i,3\phi}}{s} \tag{2.10}$$

2.3.2 Islanded Operation

Operation during islanded operation is very similar to what described in [19]. Notably, the generated and dissipated power must balance exactly within an islanded subsystem, then, a transition into islanded operation makes output power control no more possible and automatically leads the power regulator $H^{\mathrm{p}}_{3\phi}$ into saturation. Consistently, the integral part of the per-phase regulator H^{p}_{x} is also disabled. The saturation limits $P^{*\,\max}_{3\phi}$ or $P^{*\,\max}_{3\phi}$ can be designed as discussed in [19]. Remarkably, during the islanded mode of operation, the controller behaves as a traditional droop controller, by which the converter frequency ω^* changes linearly with the total delivered three-phase power:

$$\omega^* = \omega_0 + k_{p,3\phi}\left(P^{*\mathrm{sat}}_{3\phi} - P_{3\phi}\right) \tag{2.11}$$

where $P^{*\mathrm{sat}}_{3\phi}$ is a constant saturation limit, namely, $P^{*\,\max}_{3\phi}$ or $P^{*\,\min}_{3\phi}$. In the same way, the reactive power controller $H^{\mathrm{q}}_{3\phi}$ saturates too:

$$V = V_0 + k_{q,3\phi}\left(Q^{*\mathrm{sat}}_{3\phi} - Q_{3\phi}\right) \tag{2.12}$$

leading the control to operate as a traditional droop scheme with a smooth transition to the islanded operation.

2.4 Experimental Results

The proposed controller was tested in simulation and by means of a laboratory-scale experimental prototype implementing the system in Figure 2.2. The used setup is the one detailed in [19].

Figure 2.5 and Figure 2.6 display the most significant experimental waveforms to show the chief features of the control. The instantaneous three-phase voltages and currents are reported on the subfigures placed on the left, while the subfigures on the right display the related active power P_a, P_b, P_c, and reactive power $Q_{3\phi}$, the voltage amplitudes deviation ΔV, the frequency deviation $\Delta\omega^*$ and the phase displacement with respect to the first phase (i.e., $\varphi^*_b - \varphi^*_a$ and $\varphi^*_c - \varphi^*_a$).

The per-phase powers are computed using the definition for single-phase power:

$$P_x = \frac{1}{T^*}\int_{t-T^*}^{t} v_x(\tau)i_x(\tau)d\tau; \quad Q_x = \frac{1}{T^*}\int_{t-T^*}^{t} v_x\left(\tau - \frac{T^*}{4}\right)i_x(\tau)d\tau; \tag{2.13}$$

(a)

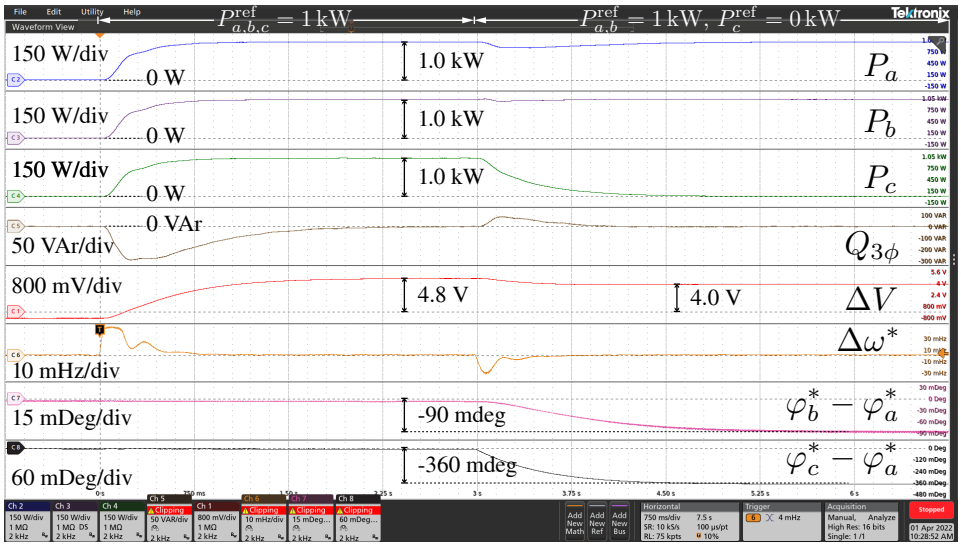

(b)

Figure 2.5: Experimental results with EPC in Figure 2.2 implementing the proposed control scheme in Figure 2.4. (a)-(b) reference step change P_a, P_b, P_c^{ref} : $0 \rightarrow 1\,\text{kW}$ @ $0\,\text{s}$ and P_c^{ref} : $1 \rightarrow 0\,\text{kW}$ @ about $3\,\text{s}$ while connected to the grid.

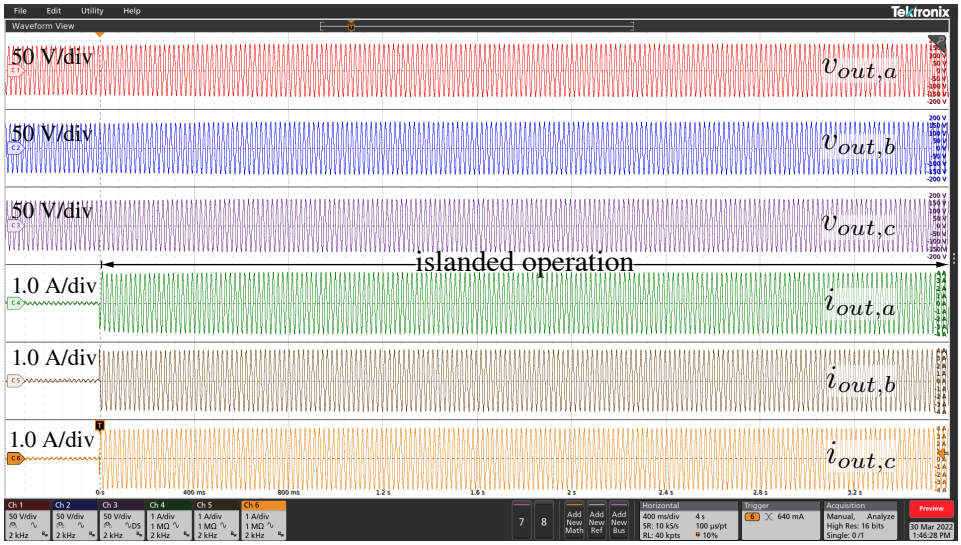

(a)

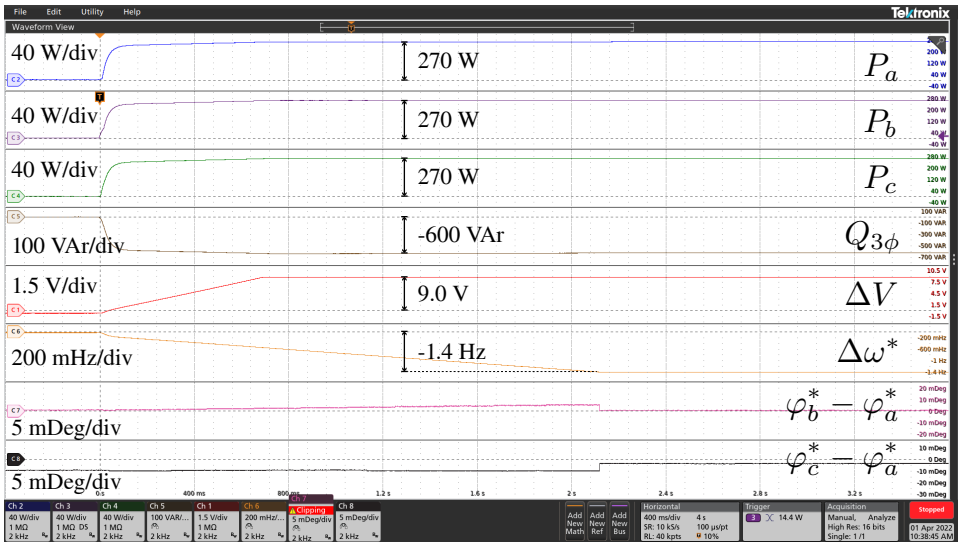

(b)

Figure 2.6: Experimental results with EPC in Figure 2.2 implementing the proposed control scheme in Figure 2.4. (a)-(b) Transition into the islanded operation with a balanced local load connected.

Then, $P_{3\phi} = P_a + P_b + P_c$, and $Q_{3\phi} = Q_a + Q_b + Q_c$. Using this definition allows to avoid oscillating components that are typically seen using instantaneous power theory in unbalanced three-phase systems [39]. The results are discussed next.

2.4.1 Balanced and Unbalanced Power References Variations

Figure 2.5(a)-(b) show the response of the system to a power reference step change. Specifically, the response to a balanced reference step change P_a, P_b, $P_c : 0 \longrightarrow 1\,\text{kW}$ is shown first. Then, a subsequent transient is displayed in which solely phase-c is subject to a reference change $P_c : 1\,\text{kW} \longrightarrow 0$, making the system to operate unbalanced. The total requested reactive power reference is kept fixed to zero. Figure 2.5(b) demonstrates the expected transient in terms of active and reactive power, with zero steady-state tracking errors. As expected, during balanced power reference tracking, phase displacements $\varphi_b^* - \varphi_a^*$ and $\varphi_c^* - \varphi_a^*$ are not affected by balanced power references, being the necessary phase-shift to allow the desired active power exchange the same in the three phases and included in variations of the instantaneous phase $\varphi_{3\phi}$ related to the integral of the shown $\Delta\omega^*$. Besides, in this transient, the decoupling matrix T in (2.9) prevents any reaction of the per-phase control loops involving P_x. Some voltage variations ΔV can be noticed as a secondary effect, due to residual resistive components of the interconnection impedance among the inverter and the grid of the experimental setup. The following unbalanced transient $P_c : 1\,\text{kW} \longrightarrow 0$ stimulates the reaction of the per-phase control loops, which introduces the required phase deviation $\varphi_c^* - \varphi_a^*$ in order to allow the unbalance power flow at phase-c. Due to the decoupling matrix T, which prevents the per-phase loops from regulating balanced power terms, the variation of the resulting total power and balanced power stimulates the response of the synchronization loop too. This brings to a transient variation of the instantaneous frequency ω^* that gives the instantaneous phase $\varphi_{3\phi}$ and a corresponding further adjustment of $\varphi_b^* - \varphi_a^*$.

2.4.2 Grid-tied to islanded transition

Figure 2.6(c)-(d) show the response of the system to a sudden disconnection from the main grid, namely, a transition to the islanded operation. In this test, the local load is balanced, composed of three $50\,\Omega$ resistors in parallel with three $50\,\mu\text{F}$ capacitors, star connected at the output of the inverter. At the opening of the circuit breaker CB, in Figure 2.2, the proposed controller is capable of maintaining the local voltage, without any discontinuity in the supply of the load. Due to the absence of the main grid ensuring the balance among power generation and absorption, power tracking,

which makes the active and reactive power regulators to deviate toward the set saturation limits. Notably, this does not impact the quality of the supplied voltage, producing voltage deviations ΔV and frequency deviations $\Delta\omega^*$ that are within tolerable limits by design.

2.5 Conclusions

Despite the limitations of three-phase three-wire systems, where fully independent per-phase power control is not possible as it is in four-wire systems, the available degrees of freedom still allow for good flexibility. This chapter has shown a technique that allows the independent control of four out of six active and reactive per-phase power components. This unlocks possibilities such as unbalance compensation in three-phase three-wire systems.

Summary

In this chapter:

- power flow in three-phase ac circuits is briefly reviewed, and three-wire systems limitations are discussed;
- a droop-based per-phase power controller is illustrated, discussing its capability of regulating the per-phase power in three-phase three-wire systems while still complying with their limitations;
- its islanded transition and operation mechanisms are discussed;
- experimental results validate its ability to handle unbalanced power references and seamless transitions to stand-alone operation.

Droop-Based Power and Unbalanced-Currents Controller 3

This chapter presents an alternative droop-based power controller capable of unbalanced operation and smooth islanded transition. Differently from the one discussed in Chapter 2, which allows the control of the output power phase-by-phase, this controller regulates the positive-sequence active and reactive powers. Then, negative-sequence current components can be injected during grid-connected operation. Section 3.3 describes the operating principles of the proposed approach and derives the small-signals loop gains; Section 3.4 illustrates basic guidelines for the design of the controller parameters; Section 3.5 and Section 3.6 show simulation and experimental results respectively, validating the control approach.

3.1 Introduction

As discussed in Section 2.1, flexible power control is a crucial feature of EPCs in microgrids, enabling the system react to power references issued by controllers for local power flow optimizations [40], to provide demand-response services requested to the microgrid, or to participate in transactive energy markets [41, 42]. A second crucial feature is the availability of suitable EPC controllers endowing the microgrid capability of operating islanded from the main grid, which is valuable in several modern circumstances [43, 44]. Last, unbalanced current control should be included considering the control of fundamental quantities at the output of EPCs for power quality enhancements. This control flexibility can be exploited to compensate unbalanced currents measured at the connection with the upstream grid in three-phase systems populated by unbalanced or single-phase loads, which is a common issue in low-voltage grids. The outlined scenario is schematically represented in Figure 3.1.

The analysis of the literature reveals that the cohesive integration of these features presents a relevant challenge. The main difficulty stems from the fundamentally different control requirements for grid-tied operation and islanded operation. In grid-tied operation, the goal of reference tracking must be achieved regardless of grid conditions. On the other hand, if islanded, inverters must adapt to grid conditions to properly operate in parallel with other units and support grid voltage.

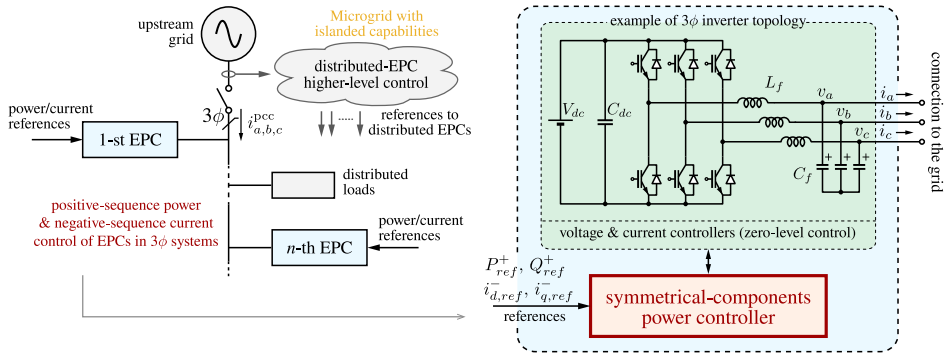

Figure 3.1: Schematic overview of the future smart microgrid scenario. Differently from Chapter 2, positive-sequence power and negative-sequence current are considered herein.

Droop control is widely used to implement grid-forming converters and achieve islanded operation capabilities. However, when droop control is applied, output power tracking is not automatically obtained, and controlling unbalanced output currents requires dedicated provisions. While current controllers [24] allow the most flexible control during grid-tied operation, the islanded operation is not supported. An example is provided in [45], in which a control for grid-tied converters is proposed that is capable of injecting unbalanced and harmonic currents, but it does not allow islanded operation. On the other hand, droop control approaches like [46] allow islanded operation but do not support unbalanced compensation. Similar limitations can be found in [47] and [48]. In [20], a compensation method is proposed that allows to share the unbalanced power so that the total power on each phase is distributed among converters in proportion to their nominal power. Still, the additional flexibility of directly controlling the converters' contributions based on given references may be required for network optimizations [31, 40]. Several works discuss the concept of virtual synchronous machines (VSMs), like, for example, [49, 50, 51]. In this case too, the capability of supporting phase-by-phase power control, to provide, for example, unbalanced compensation, coupled with the grid-forming function is typically not achieved. In [52, 53] the virtual-oscillator control (VOC) technique is modified to enhance the operation in three-phase unbalanced grids. Nevertheless, the testing of operation with distinct power references for each phase has not been conducted.

Preliminary solutions to couple power control and islanded operation are documented in [26], where a total output power controller is proposed that also allows seamless transitions toward the islanded operation. As a prosecution of this work, output power control performed on the three-phases (i.e., per-phase) aiming at unbalance power compensation is introduced in [19] and [12]. The latter in par-

ticular, is the work presented in Chapter 2. In these works, per-phase active and reactive power control in three-phase four-wire systems, the former, and three-wire systems, the latter, are tackled. The approach in these two methods, however, assumes that the unbalance compensation is performed providing unbalanced power, as in [17]. However, symmetrical-components give a more natural approach to unbalance compensation, as in [54], and allow a unique controller implementation for three-phase EPCs with or without the neutral wires. Remarkably, three-wire systems with the neutral wire and also without the neutral wire are both relevant in low-voltage networks [55], and the controller proposed herein is compatible with both configurations.

Approaching the problem through a positive- and negative-sequence power controller would be ineffective. While, during normal operation, positive-sequence voltage has a well-defined and bounded amplitude value, this is not true for negative-sequence voltage. The negative-sequence power loop-gain would vary with the negative-sequence voltage amplitude, and may reduce to zero in case of perfectly balanced three-phase voltages. For this reason, droop control on negative-sequence powers can not be performed as commonly done for positive-sequence powers. The solution proposed in this chapter controls positive-sequence powers, for active and reactive output power tracking, and injects negative-sequence currents, to provide unbalanced compensation, by generating a suitable negative-sequence voltage component. In the control, the active-power control loop is used to synchronize the generated voltages with the grid, exploiting the feature discussed in [37], and to derive the negative-sequence instantaneous phase used to regulate the injected negative-sequence currents. In summary, the proposed method features:

i: active and reactive power tracking;

ii: unbalance current regulation;

iii: grid-forming capability;

iv: parallel operation with multiple grid-forming units;

v: smooth and seamless transition toward islanded operation;

3.2 Key AC Power Transfer Relations

As seen in Section 2.2, the per-phase output power flow in three-phase systems can be expressed as (2.2) in four-wire systems, and as (2.3) in three-wire systems.

In this case, the focus is on the power flow as a result of positive-sequence components. In both three-wire and four-wire systems, under this assumption, the total complex power flow can be expressed as:

$$\dot{S} = 3\frac{V_i V_g}{\omega_g L}\sin(\varphi_i) + 3j\frac{V_g}{\omega_g L}\left[V_i\cos(\varphi_i) - V_g\right] \tag{3.1}$$

which can be linearized, for small φ_i and $\Delta V_i \triangleq \left(V_i - V_g\right)$ as:

$$P^+ \approx 3\gamma_p\varphi_i; \quad Q^+ \approx 3\gamma_q\Delta V_i. \tag{3.2}$$

As in Section 2.2, $\gamma_p \triangleq \frac{V_g^2}{\omega_g L}$ and $\gamma_q \triangleq \frac{V_g}{\omega_g L}$. These relations are considered in the following sections to describe the proposed controller.

It is worth remarking that the power-flow relations (3.2), holding with inductive interconnection impedances, allow the use of P-f and Q-V droop laws [36]. These laws are preferred, over other alternatives, because they allow accurate active power sharing, and they preserve the desirable active-power *versus* frequency relations characteristic of synchronous generators [56]. If necessary, the inductive behavior is commonly enforced through impedance emulation, by a suitable design of the EPC output voltage regulator, or by adding a dedicated virtual-impedance loop as done, for example, in [56, 57, 58].

3.3 Proposed Control Technique

Power control is achieved via droop control, which assumes in this case inductive line impedance. As discussed in Section 3.2, this is an assumption commonly verified. Moreover, it is possible to enforce this condition via impedance emulation techniques.

3.3.1 Controller Structure

The controller can be divided into three sections, as shown in Figure 3.2 and explained in the following.

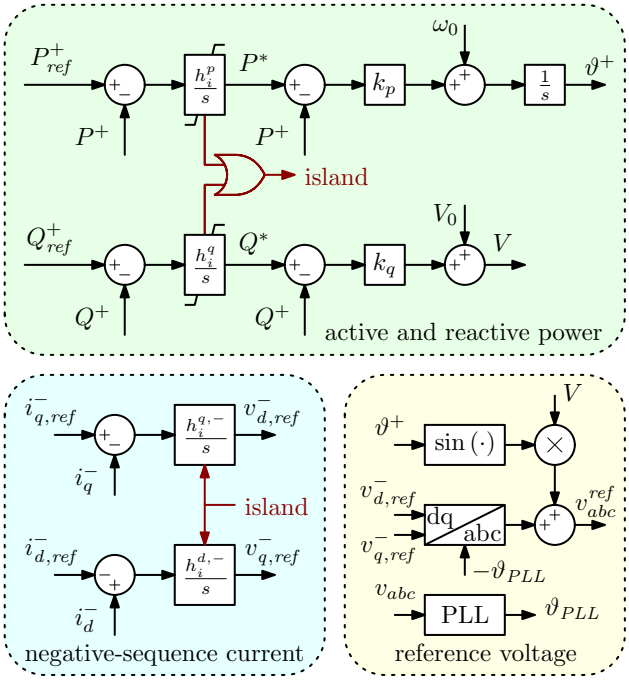

Figure 3.2: Block scheme of the proposed controller.

Active and Reactive Power Controllers

first, the active power controller is composed of an inner loop that implements the classical P-f droop characteristic:

$$\omega = \omega_0 + k_p\left(P^* - P^+\right) \tag{3.3}$$

where ω_0 and ω are the reference and actual grid frequencies, k_p is the droop coefficient, P^* is the power reference, and P^+ is the direct-sequence measured active-power. Then, an outer control loop adjusts P^* to track the reference signal and achieve $P^+ = P^+_{\text{ref}}$. This loop is responsible for the synchronization with the instantaneous phase of the voltage at the point of connection of the EPCs with the grid [37].

Similarly, the reactive power controller is composed of an inner loop that implements the Q-V droop characteristic:

$$V = V_0 + k_q\left(Q^* - Q^+\right) \tag{3.4}$$

where V_0 and V are the reference and the actual grid voltages, respectively, k_q is the

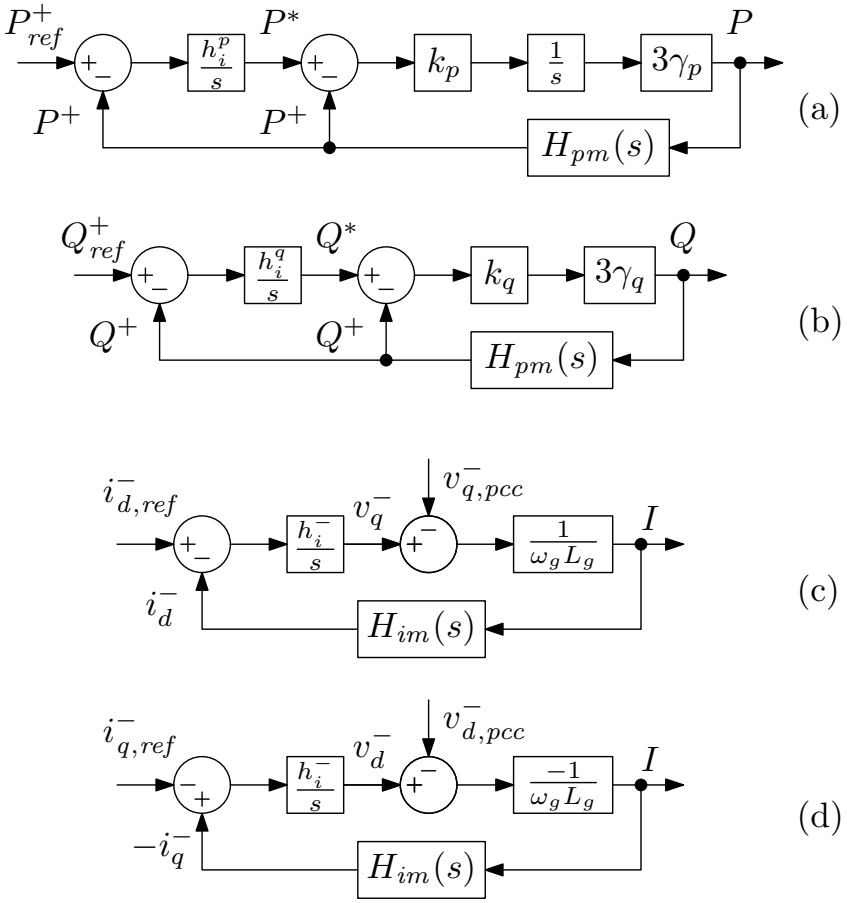

Figure 3.3: Small-signals block schemes of a grid-tied converter controlled with the proposed method. Figures (a) — (b) are the active and reactive power loops, while (c) — (d) are the negative-sequence current loops.

droop coefficient, Q^* is the power reference, and Q^+ is the measured direct-sequence reactive power. Then, an outer control loop adjusts Q^* to track the given reference signal and achieve $Q^+ = Q^+_{\text{ref}}$. Then, the positive-sequence voltage reference is defined by the instantaneous phase given by the active power controller and the voltage amplitude given by the reactive power controller.

The small-signals block diagrams for the active and reactive power loops are shown in Figure 3.3 (a) — (b). The loop gains can be written as:

$$T_{P^+}(s) = \frac{h_i^p}{s} \cdot \frac{3\gamma_p k_p H_{\text{pm}}(s)}{s + 3\gamma_p k_p H_{\text{pm}}(s)} \tag{3.5}$$

$$T_{Q^+}(s) = \frac{h_i^q}{s} \cdot \frac{3\gamma_q k_q H_{\text{pm}}(s)}{1 + 3\gamma_q k_q H_{\text{pm}}(s)} \tag{3.6}$$

where $3\gamma_p$ and $3\gamma_q$, as defined in (3.2), are plant parameters describing the inverter response to phase-shift and voltage amplitude variations, while $H_{\text{pm}}(s)$ models the dynamics of the power measurement.

Negative-Sequence Currents Controller

This controller adds a negative-sequence voltage component to the reference produced by the power controllers, in order to enforce the flow of a set negative-sequence current that can be exploited for unbalance control. Assuming inductive line impedances, the voltages v_d^- and v_q^-, together with the components $v_{d,\text{pcc}}^-$ and $v_{q,\text{pcc}}^-$ at the point of common coupling (PCC), determine the negative-sequence current, as represented in Figure 3.3 (b) — (c). Herein, a clockwise rotating instantaneous phase, where d-axis is leading the q-axis, is used. From the scheme, considering the PCC voltage as an exogenous input, the loop gains of the negative-sequence current controller are:

$$\begin{aligned} T_{i_d^-}(s) &= -\frac{h_i^{q,-}}{s} \cdot \frac{1}{\omega_g L_g} \cdot H_{\text{im}}(s); \\ T_{i_q^-}(s) &= \frac{h_i^{d,-}}{s} \cdot \frac{1}{\omega_g L_g} \cdot H_{\text{im}}(s); \end{aligned} \tag{3.7}$$

where $1/(\omega_g L_g)$ represents the plant, that is, the dq impedance seen by the converter when injecting negative-sequence components.

Reference Voltage Generation

the generation of the voltage reference $v_{\text{abc}}^{\text{ref}}$ is built by adding the contribution from the active and reactive power controller and the negative-sequence current controller. The former contribution constitutes the positive sequence component of the voltage reference; it presents amplitude V and instantaneous phase ϑ^+. The latter contribution constitutes the negative sequence component of the voltage reference and it is derived from the components $v_{d,\text{ref}}^-$ and $v_{q,\text{ref}}^-$. It is worth remarking that the final reference provided by the proposed controller is a voltage reference for the EPCs, which are always controlled as voltage sources.

3.3.2 Grid-Tied Operation

During grid-tied operation EPC output power regulation is physically possible, because the presence of the main grid ensures the presence of a slack node that can supply the mismatch among the power absorbed by the loads and the generation by the distributed EPCs [38]. The integrators in the active and reactive power loops will adjust the reference values P^* and Q^* in order to set the output power to the reference values P^+_{ref}, Q^+_{ref}. This is needed in case the grid voltage frequency and amplitude are differ from the nominal value.

The negative-sequence instantaneous phase is computed using a phase-locked loop (PLL) fed with the output capacitor voltages v_a, v_b, v_c and providing the phase ϑ_{PLL}, as shown in Figure 3.2. In fact, the phase ϑ^+ may differ from the phase of the actual output voltages due to the implemented virtual output impedances and the non-ideality of the voltage regulator.

Active and reactive power reference values, together with negative-sequence current ones, are provided externally with respect to this controller, as foreseen in the scenario represented in Figure 3.1.

3.3.3 Islanded Transition and Operation

When the main grid disconnects, the conditions highlighted at the beginning of Section 3.3.2 decay, and the generated power within the microgrid must automatically match loads consumption. Being power regulation no more possible, the power regulation error increases, leading the integrators in the power regulation loop to saturate. Eventually, the system enters islanded operation with fixed droop characteristics

$$\begin{cases} \omega = \omega_0 + k_p\left(P^*_{\text{sat}} - P_d\right) \\ V = V_0 + k_q\left(Q^*_{\text{sat}} - Q_d\right) \end{cases} \tag{3.8}$$

which allows automatic load sharing among the EPCs connected to the islanded microgrid. The transition, from the point of view of the output voltage, happens in a smooth and seamless way. When at least one integrator reaches saturation, a reset signal is sent to the negative-sequence current controller, disabling it. Remarkably, the island detection is performed independently by each inverter, so that no coordination is needed, neither among converters nor toward a centralized controller.

3.4 Controller Design

The main equations for the design of the controller are derived in this section, and the design process is discussed, starting from the choice of the saturation thresholds, through the design of the power regulation loops, to the negative-sequence current loops design.

3.4.1 Droop Coefficients and Saturation Thresholds

Droop coefficients can be chosen in various ways, and in general there is a trade off between the error in the drooped quantities and the speed of the dynamic response of the system. A simple design procedure is to consider the nominal power of the inverter S_N (assuming to be both nominal absorbed and supplied output power) and the width of the interval in which ω and V can vary, then:

$$k_p = \frac{\omega_{\max} - \omega_{\min}}{2S_N}; \quad k_q = \frac{V_{\max} - V_{\min}}{2S_N} \tag{3.9}$$

as it is commonly done. More sophisticated methods exist, allowing the investigation of small-signals behavior of multiple parallel-connected droop-controlled ac sources, like, for example, [59, 60].

Once droop coefficients are determined, it is possible to define the saturation values for the integrators in the power loops. Starting with the active power, from (3.3) it is possible to write

$$P^* = \frac{\omega - \omega_0}{k_p} + P^+$$

which is the droop characteristic reference value needed to generate a particular value P^+ of active power when the actual grid frequency is ω. By knowing the minimum and maximum ω value of the tolerable grid frequency and the maximum and minimum P^+ that the inverter can generate (or absorb), it is possible to find

$$P^*_{\min} = \frac{\omega_{\min} - \omega_0}{k_p} - S_N; \quad P^*_{\max} = \frac{\omega_{\max} - \omega_0}{k_p} + S_N \tag{3.10}$$

Similarly for Q^*, from (3.4):

$$Q^* = \frac{V - V_0}{k_q} + Q^+$$

then

$$Q^*_{\min} = \frac{V_{\min} - V_0}{k_q} - S_N; \quad Q^*_{\max} = \frac{V_{\max} - V_0}{k_q} + S_N \tag{3.11}$$

by knowing $V_{\min}$, $V_{\max}$, $Q_{\min}$, and $Q_{\max}$. It is worth remarking that, in order to track all the references for the reactive power, it may be necessary to extend the considered thresholds, as voltage amplitude is not the same along the whole microgrid.

3.4.2 Power Regulation Loops

The active-power loop and the reactive-power loop have different dynamic behavior, because the former includes an additional pole in the origin due to the integrator computing the instantaneous-phase signal ϑ.

From (3.5), the value of h_i^p can be chosen based on desired specifications of control bandwidth and phase margin. Neglecting the power measurement dynamics $H_{\text{pm}}(s)$, initial licit solutions are $h_i^p = 3\gamma_p k_p/4$, to achieve a critically damped (i.e., coincident real poles) closed-loop transfer function, or $h_i^p = 3\gamma_p k_p/2$, to achieve a 2-nd order Butterworth poles placement (i.e., $\xi = 1/\sqrt{2}$).

For what concerns the reactive-power loop, it is possible to achieve wider control bandwidths, which are limited only by the power measurement block while the process to be regulated is static. Considering (3.6), and neglecting the dynamics of the power measurement, one can write

$$T_{Q^+}(s) = \frac{h_i^q}{s} \cdot \frac{3\gamma_q k_q}{1 + 3\gamma_q k_q} = \frac{h_i^q}{s} A_{Q^+}$$

and then choose $h_i^q = \omega^*/A_{Q^+}$ where ω^* is the target bandwidth, which, for example, may be set to match the active-power loop bandwidth.

3.4.3 Negative-Sequence Current Loop

The negative-sequence current regulation is performed by decomposing the currents into symmetrical components, using a reference frame synchronized with the instantaneous phase ϑ^- provided by the PLL. As discussed in the previous section, i_d^- is regulated adding a v_q^- component, while i_q^- by adding a v_d^- component. From (3.7), and neglecting the current decomposition dynamics, the design is straightforward. For example, the target bandwidth ω^* can be set first and, subsequently, choose $h_i^{q,-} = h_i^{d,-} = \omega^* \omega_g L_g$.

3.4.4 Poles Trajectories

Figure 3.4 shows the poles trajectories of the closed-loop system with respect to the design of the outer integral regulator. In particular, Figure 3.4 a shows the closed-loop pole locations of the active-power loop (3.5) as h_i^p is varied. The same is shown in Figure 3.4 b for the reactive-power loop (3.6), varying h_i^q. Similarly, the location of the poles for negative-sequence current-loops are shown, assuming the same regulator gain h_i^- for both loops (3.7). The power measurement and current decomposition dynamics are considered to be first-order filters, as follows:

$$H_{\text{pm}}(s) = \frac{1}{1 + s/\omega_{\text{pm}}}; \quad H_{\text{im}}(s) = \frac{1}{1 + s/\omega_{\text{im}}} \tag{3.12}$$

3.5 Simulation Results

The proposed controller has been validated by simulation results, discussed in this section, and experimental results, discussed in Section 3.6. The simulation results are carried out in order to validate the parallel operation of two inverters implementing the proposed control method.

The test is devised to validate all the capabilities of the proposed method, namely, *a)* grid-tied operation, *b)* active power reference tracking, *c)* reactive power reference tracking, *d)* unbalance current compensation at the PCC, *e)* transition into islanded operation, and *f)* islanded operation. In the test, two inverters are connected in parallel and initially operating in grid-tied mode. The two inverters have identical control parameters, reported in Table 3.2. Two different loads are connected at the PCC, namely, an unbalanced three-phase Y resistive load, composed of two 10 Ω and one 30 Ω resistors, and a balanced three-phase Y capacitive load, composed of three 100 µF capacitors. The test scenario corresponds to the one depicted in Figure 3.1, assuming $n = 2$.

Figure 3.5 reports the main quantities of the EPCs along the performed test and a table that describes the succession of events. From top to bottom, the left side of Figure 3.5 displays active powers, reactive powers, and the current amplitudes at the PCC; the right side of Figure 3.5 displays the grid frequency, the voltage measured at the output of an EPC and the instantaneous PCC voltage across the disconnection from the main grid disconnection, which happens at $t = 15$ s. Steps of power references are applied during intervals (b), considering active power, and (c), considering reactive power. Interval (d) shows the unbalanced current control capability of the proposed controller exploited with the goal of compensating the

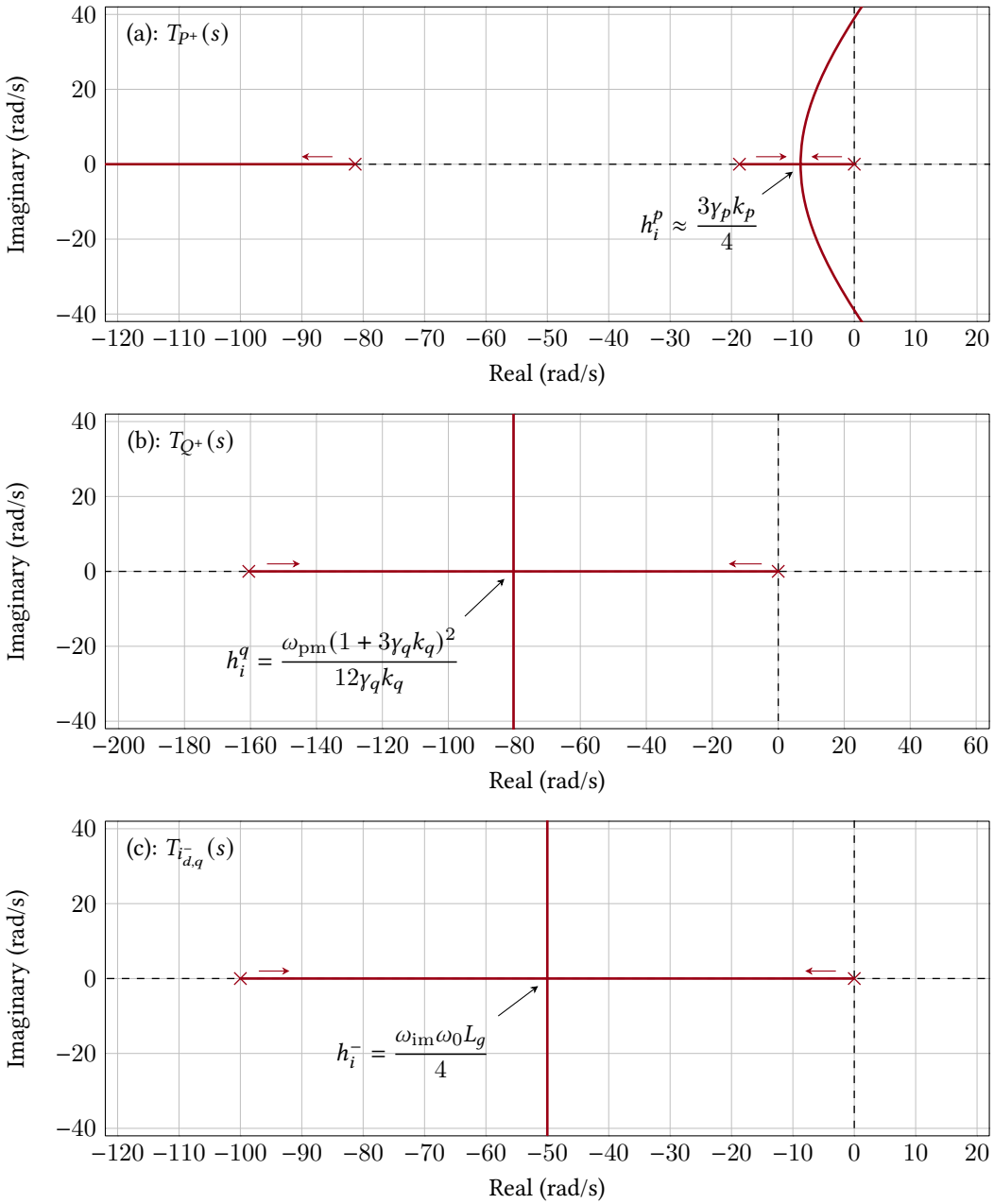

Figure 3.4: Trajectories of the closed-loop poles varying the design of the integral regulators. (a) Shows trajectories for active-power loop (3.5), (b) for reactive-power loop (3.6), and (c) for negative-sequence current loops (3.7). The power measurement and current decomposition dynamics are assumed to be first-order low-pass filters, with cut-off frequencies respectively ω_{pm} and ω_{im}, as shown in (3.12).

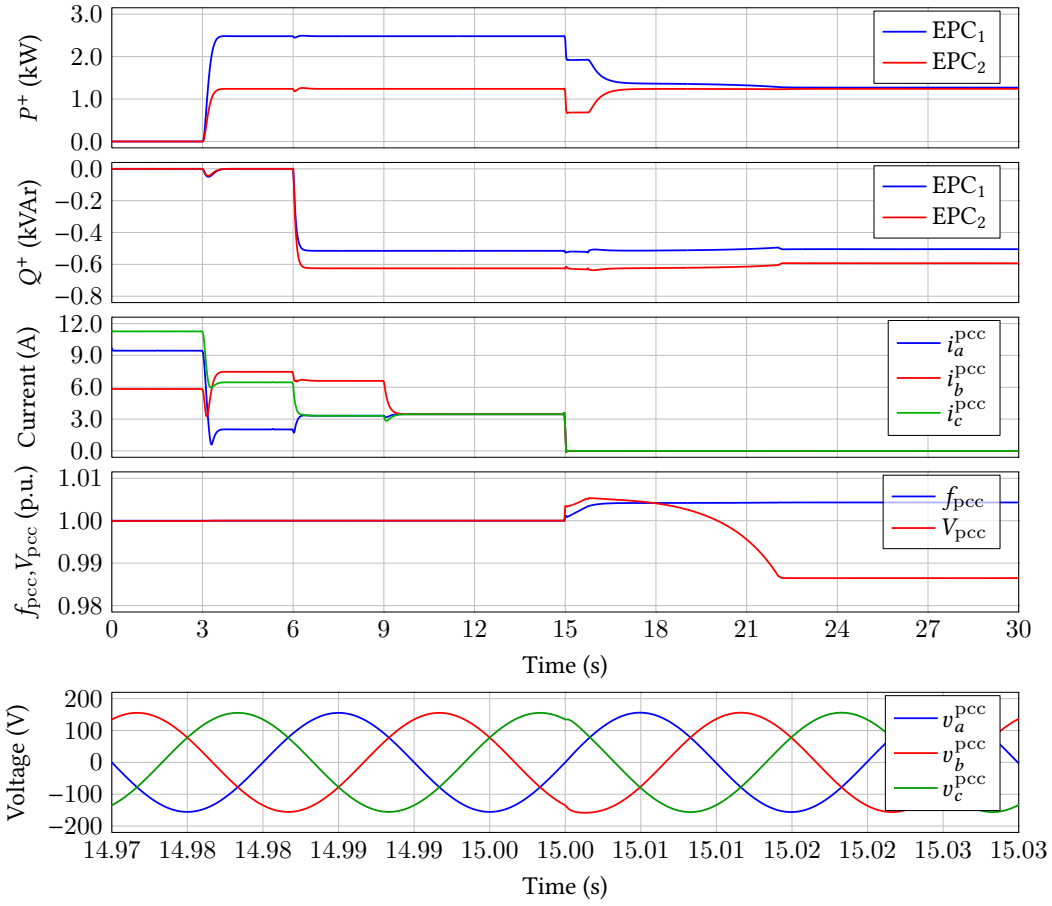

(a) $0 \leq t < 3$ s Start	**(b)** $3 \leq t < 6$ s $P_1^+ : 0 \rightarrow 2480$ W $P_2^+ : 0 \rightarrow 1240$ W	**(c)** $6 \leq t < 9$ s $Q_1^+ : 0 \rightarrow -515$ VAr $Q_2^+ : 0 \rightarrow -625$ VAr
(d) $9 \leq t < 15$ s Unbalanced PCC current compensation	**(e)** $15 \leq t < 22.2$ s Grid disconnection transition to island	**(f)** $t \geq 22.2$ s Islanded operation

Figure 3.5: Simulation test with two parallel-operating inverters, initially operating in grid-tied condition. Unbalanced three-phase Y load is connected at the PCC, composed of two 10 Ω and one 30 Ω resistors, and three 100 µF capacitors. Nomenclature as in Figure 3.1.

unbalanced current at the PCC. To this end, the negative-sequence currents at the PCC are measured and then used as reference for the signals $i^-_{q,\text{ref}}$ and $i^-_{d,\text{ref}}$. The reference signals are set at the same value for EPC_1 and EPC_2, equal to half of the negative-sequence currents initially measured at the PCC, in order to evenly share the compensation effort; remarkably, the measured current during this interval (d) are balanced, as desired and expected based on the set references. In (e), at $t = 15\,\text{s}$, the main grid is disconnected. The two inverters start the transition to islanded operation, which is completed at the beginning of (f), at $t = 15\,\text{s}$.

3.6 Experimental Results

The proposed controller has been validated experimentally under different operating conditions. The results reported in the following were obtained using the experimental setup displayed in Figure 3.6. It includes two EPCs, implemented by using a rapid prototyping system that is described in detail in [61]. Each EPC embeds an Imperix® BBoard Pro™ digital controller and three half-bridge power boards based on 600 V, 50 mΩ GaN FETs by Texas Instruments (LMG341xR050). Each EPCs is supplied by a dedicated power supply Keysight RP7962A. The upstream main grid is emulated by a Cinergia ac voltage source, model GE/EL+20 vAC/DC. Data acquisition is performed by Dewesoft SIRIUSi digital acquisition systems.

The parameters of the EPCs as defined in Figure 3.1 are listed in Table 3.1, and control parameters are listed in Table 3.2.

In the following, three test configurations are reported, namely, Section 3.6.1) power regulation in grid-connected operation with balanced load plus a transition toward islanded operation, Section 3.6.2) negative-sequence current regulation for supplying an unbalanced three-phase load plus a transition toward islanded operation, Section 3.6.3) power and unbalance regulation of two parallel-connected inverters connected to a grid with unbalanced voltages plus a transition toward islanded operation. The first two configurations are meant to show the principle of operation of the controller in a simple application example with a single EPC. The third configuration shows the operation of the controller in a more realistic condition and considers two EPCs.

3.6.1 Power Regulation with a Single Inverter

In this test, a three-phase inverter, namely, EPC 1, is tied to the three-phase ac grid; EPC 2 is disconnected. A three-phase balanced 27 Ω resistive load is locally

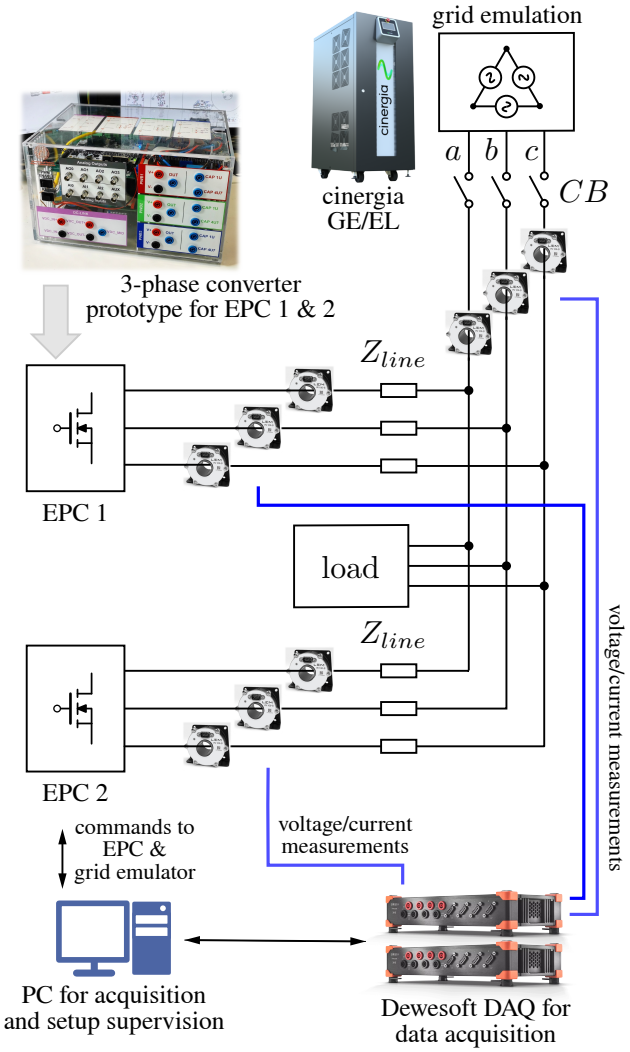

Figure 3.6: Scheme of the experimental setup.

Table 3.1: Inverter and grid parameters

Parameter		Value	
DC-Link voltage	V_{dc}	370	V
Switching frequency	f_{sw}	50	kHz
Output filter inductor	L_f	340	µH
Output filter capacitor	C_f	5.7	µF
Nominal power rating	S_N	3	kV A
Grid frequency	ω_g	$2\pi \cdot 50$	rad s^{-1}
Grid rms voltage	V_g	110	V
Line impedance	Z_{line}	26.6 mΩ, 48 µH	

Table 3.2: Controller parameters

Parameter		Value	
Inductive output impedance	L_g	3.18	mH
P-f droop coefficient	k_p	0.419	
Q-V droop coefficient	k_q	1.83	
Active-power integral gain	h_i^p	5	
Reactive-power integral gain	h_i^q	30	
Negative-sequence curr. int. gain	h_i^i	6.28	
Active power sat.	$P^*_{\text{max,min}}$	±4.5	kW
Reactive power sat.	$Q^*_{\text{max,min}}$	±4.5	kVAr
Negative-sequence volt. sat.	$v^-_{\text{max,min}}$	±15	V
Frequency reference value	ω_0	$2\pi \cdot 50$	rad s^{-1}
Voltage reference rms value	V_0	110	V

connected. The main waveforms are shown in Figure 3.7, which reports the direct-sequence active and reactive powers, the rms values of output voltage and current, and the frequency. Initially, both P^+_{ref} and Q^+_{ref} reference values are equal to zero. At $t = 6.2$ s, a step change $P^+_{\text{ref}} : 0\,\text{W} \longrightarrow 2.4\,\text{kW}$ is performed, and at $t = 9.2$ s the inverse step change $P^+_{\text{ref}} : 2.4\,\text{kW} \longrightarrow 0\,\text{W}$ is applied. At $t = 12.2$ s the same step change is done for $Q^+_{\text{ref}} : 0\,\text{VAr} \longrightarrow 2.4\,\text{kVAr}$, and then again $Q^+_{\text{ref}} : 2.4\,\text{kVAr} \longrightarrow 0\,\text{VAr}$. The first graph in Figure 3.7 shows that the system correctly tracks the given power reference values. At $t = 19.6$ s the grid is disconnected by opening the circuit breaker *CB* in Figure 3.6 and the EPC automatically initiates its transition to the island operation. Being some active power absorbed by the local load, the output frequency decreases until the integrator in the active-power regulation loop saturates. Similarly, a small value of reactive power is absorbed by the system, thus the integrator in the reactive power loop saturates too toward its upper limit. After $t \geq 23$ s, the system operates with a fixed droop characteristic.

3.6.2 Unbalance Regulation with a Single Inverter

In this test, an unbalanced three-phase load is connected to the grid. EPC 1 is connected, while EPC 2 is disconnected. The load is constituted of a 108 Ω resistive load connected between phase *b* and phase *c* only. Figure 3.8 shows the negative sequence *d*-axis and *q*-axis currents for the grid and for the EPC, and the grid rms current values. Initially, the unbalanced load is supplied by the grid, both in balanced and unbalanced components: the positive-sequence power and negative-sequence current references of the EPC are set to zero. At $t = 14.5$ s a step-change in the negative-sequence current references is performed, in order to compensate the negative-sequence current absorbed by the load. Remarkably, for $15\,\text{s} \leq t \leq 25\,\text{s}$, the grid current is mainly a positive sequence current; in fact, the EPC supplies only negative-sequence components, whilst the positive-sequence power is still supplied by the grid. At $t = 25.5$ s, the grid is disconnected, and the load is entirely supplied by the EPC. The EPC performs its transition toward island operation as in the previous test.

3.6.3 Multiple Inverters Operating in an Unbalanced Scenario

In this test, an unbalanced three-phase load is connected to the grid. The load is constituted of a 108 Ω resistive load connected between phase *b* and phase *c* only. The grid voltage is unbalanced, with an unbalance factor (UF) equal to 2.5 %, defined as the magnitude ratio of negative-sequence to positive-sequence voltage.

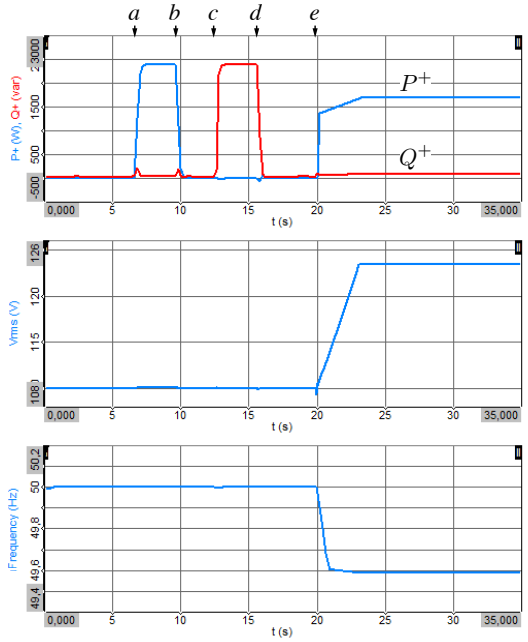

Figure 3.7: Experimental waveforms for the power regulation test.
(a) $P^+ : 0 \longrightarrow 2.4\,\text{kW}$;
(b) $P^+ : 2.4\,\text{kW} \longrightarrow 0$;
(c) $Q^+ : 0 \longrightarrow 2.4\,\text{kVAr}$;
(d) $Q^+ : 2.4\,\text{kVAr} \longrightarrow 0$;
(e) disconnection form the main grid.
With symmetrical PCC voltages, P^+, Q^+ equal total active and reactive powers.

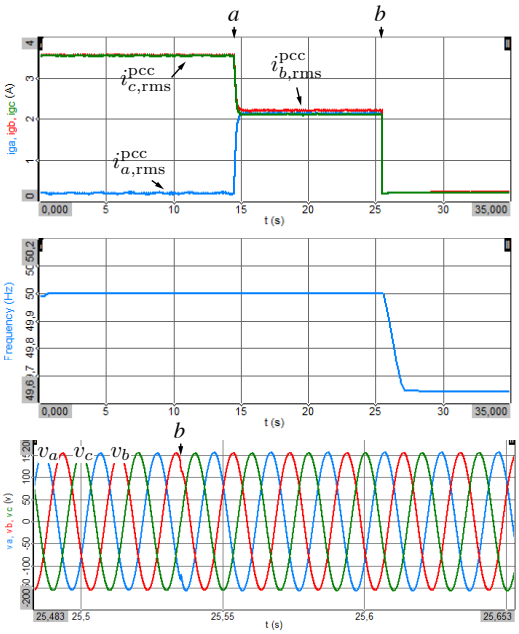

Figure 3.8: Experimental waveforms showing unbalanced compensation capabilities of the proposed controller.
(a) $i^-_{d,q}$ are set to compensate unbalanced current flow at PCC;
(b) disconnection from the main grid.
Bottom figure shows clean voltage waveforms at (b).

Both EPC 1 and EPC 2 are connected and controlled with the proposed method. The experimental waveforms are shown in Figure 3.9 and Figure 3.10.

Initially, both the inverters are set to zero output power and unbalanced current. At $t = 5\,\text{s}$, a step of active power reference is applied to both the EPCs, such that $P^{+}_{\text{ref},1} : 0\,\text{W} \longrightarrow 600\,\text{W}$, and $P^{+}_{\text{ref},2} : 0\,\text{W} \longrightarrow 900\,\text{W}$. The EPCs track the given power references and, as expected, the provided phase currents are all balanced. At $t = 8\,\text{s}$, the negative-sequence current references are set to compensate the unbalanced current absorbed by the grid. This means $i^{-}_{q,\text{ref},1} : 0\,\text{A} \longrightarrow -0.84\,\text{A}$, and $i^{-}_{q,\text{ref},2} : 0\,\text{A} \longrightarrow -0.6\,\text{A}$. Remarkably, even in an unbalanced scenario, the controller is capable of regulating the positive-sequence power and negative-sequence currents with the same dynamical performances as in the balanced case. At $t \approx 16\,\text{s}$, the main grid is disconnected, by opening the circuit breaker *CB* displayed in Figure 3.6. The inverters are involved in the transition toward islanded operation, which is completed at around $t \approx 17.5\,\text{s}$ when the integrators in the power loops reach saturation levels. At this point, the negative-sequence current loop is disabled. This creates a transient visible on the inverters rms currents in the time interval $17.5\,\text{s} \leq t \leq 18.5\,\text{s}$. Subsequently, the system reaches a steady state and the transition can be considered complete. Voltage waveforms taken around $t = 20\,\text{s}$ are shown in Figure 3.8, to prove the stability among multiple grid-forming inverters connected together.

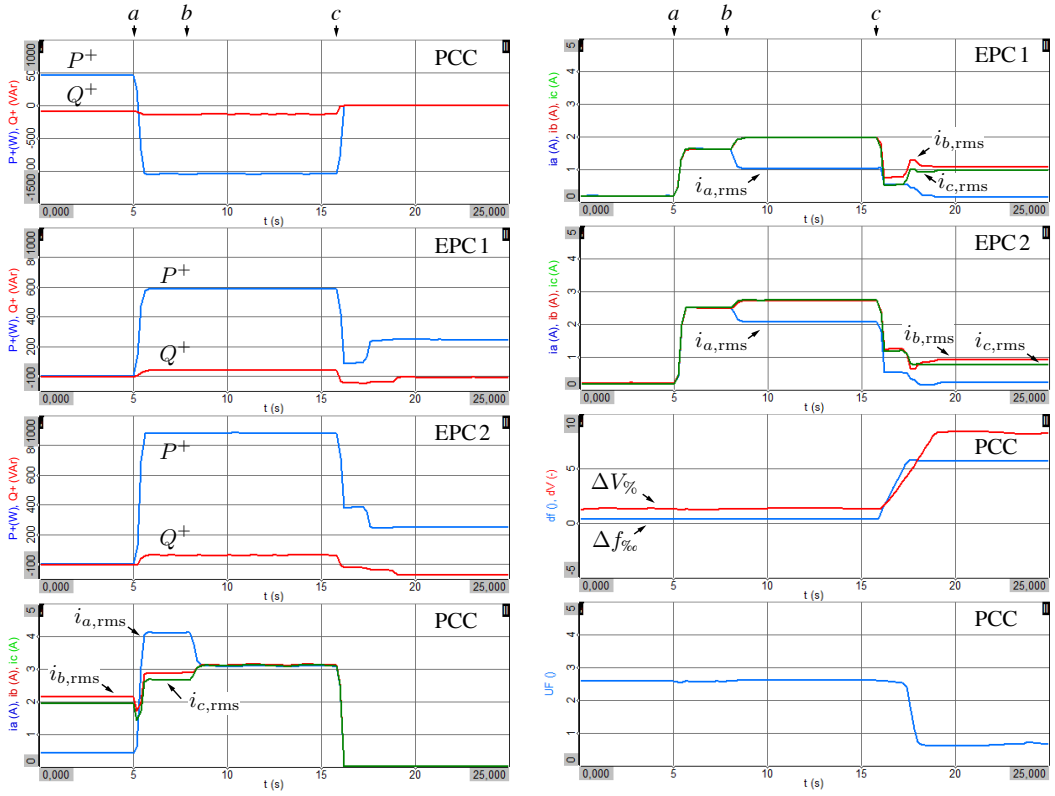

Figure 3.9: Experimental tests with two grid-tied inverters: (a) $P_1^+ : 0\,\mathrm{W} \longrightarrow 600\,\mathrm{W}$, $P_2^+ : 0\,\mathrm{W} \longrightarrow 900\,\mathrm{W}$; (b) Unbalance compensation; (c) Main grid disconnection and islanded operation.

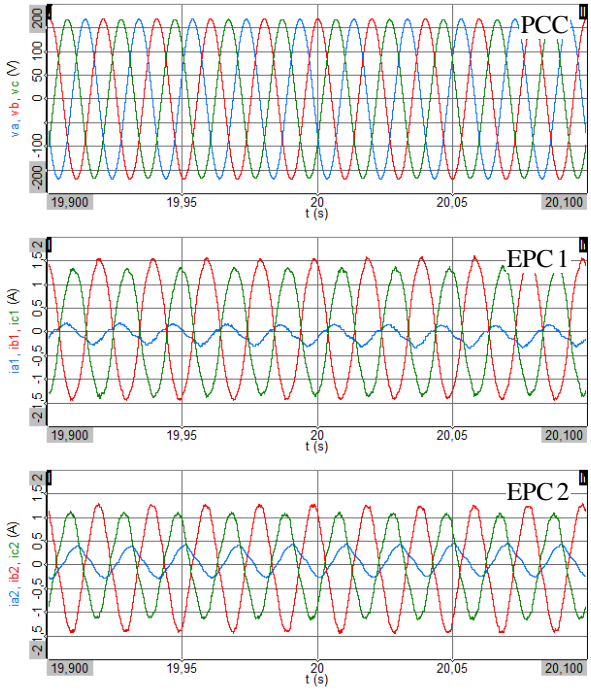

Figure 3.10: Experimental waveforms showing the islanded operation in Figure 3.9 around $t = 20$ s.

3.7 Conclusions

The solution finds applications in microgrid inverters controllers to implement active and reactive power control, unbalanced power control, and islanded operation capability of distributed three-phase inverters. Remarkably, the approach is applicable to both three-wire and four-wire systems; besides, in the latter case, it is possible to add a further loop for controlling the output homopolar current of the EPC.

Summary

In this chapter:

- a grid-forming control method for electronic power converters is presented; as the one proposed in Chapter 2, it is based on droop laws applied to positive-sequence powers, and allows smooth islanded transition and operation;
- the capability of injecting negative-sequence currents is presented and discussed, showing its application in provisions such as unbalance compensation;
- a straightforward design procedure is presented;
- simulations and experimental tests are conducted with multiple parallel-operating units, validating the unbalance compensation feature and the parallel islanded operation capability.

Fault Ride-Through in Per-Phase Controlled Converters

4

This chapter introduces a fault ride-through strategy specifically tailored for controllers of the type discussed in Chapter 2. Traditional techniques are inadequate for such controllers, as they fail to accommodate their advanced functionalities and consequently necessitate the forfeiture of certain features. The approach proposed herein, by contrast, leverages these capabilities to implement a fault ride-through mechanism that is robust under both balanced and unbalanced fault conditions.

Section 4.2 describes the assumed control technique, Section 4.3 illustrates the proposed strategy, Section 4.4 shows simulation results comparing simple current limitation against the proposed technique, and Section 4.5 shows experimental results validating the proposed technique in balanced and unbalanced faults.

4.1 Introduction

EPCs capable of supporting grid operation are crucial in smart electricity systems. Grid-forming converters present such a capability and can form the grid voltage to allow operation islanded from the main grid. Nonetheless, besides providing voltage regulation, suitable operation must be ensured also during abnormal conditions like voltage dips. However, with an operation analogous to a voltage source behind a small impedance, voltage dips can lead grid-forming EPCs to potentially unsafe output currents and real challenges in ensuring a desirable behavior. Several provisions may be implemented, as described below highlighting the pros and cons.

Switching to grid-following mode to perform low-voltage ride-through (LVRT) allows for the easy limitation of output currents, but transients may arise during mode switching. For example, in [62], the transition is smoothly achieved, although losing the voltage regulation capability and decreasing the grid strength due to the transitioning to the grid-following mode.

The typical output voltage control structure described in [63], where an inner current controller receives reference signals from an outer voltage controller, allows to act on the current reference signals to limit system operation within safe conditions, with the disadvantage that hard current limitation in stationary *abc* frame is not suitable in grid-tied operation, as it would lead to heavily distorted currents. The synchronous *dq* frame, on the contrary, allows to directly limit the

current reference values, as done in the current saturation algorithm [64]. However, transient stability is not guaranteed after the voltage dip. To tackle this issue, [65] proposes a reactive-power synchronization strategy.

Solutions based on the use of virtual-impedances are available in the literature, such as [66, 67, 68]. While effective in limiting the output converter current, the voltage regulation performances and grid strength are reduced due to the added virtual impedance.

In stationary *abc* frame circular current limiting (CCL) can be applied, where current references are multiplied by a current-limiting gain to not exceed safe values and to avoid distortions. CCL on its own is affected by transient instability, as maximum output power is reduced [64], and voltage regulation performances are degraded. For this reason, CCL is commonly employed as a fast current limitation strategy, combined with slower techniques to limit the output current by modifying the power/voltage references, as done in [69, 70, 71]. In [69] the power references are modified but the current limitation is still performed only by the CCL, and the power references are modified to meet grid-code requirements and avoid transient instability.

The approach in [70] can be applied to converters with different control schemes. It is tested with the method proposed in [47], and successfully preserves voltage regulation capabilities. However, it is not trivial how to achieve the same in flexible droop-controllers such as [13, 19] while preserving islanded operation capability. Finally, the approach in [71] preserves voltage-regulation performances too, but prevents the islanded operation.

The goals of this method for converters capable of transitioning into islanded operation are:

1. to limit output currents during voltage dips;
2. to retain voltage regulation capabilities;
3. to preserve smooth islanded transition and operation.

4.2 Converter Control Structure

The converter control structure is shown in Figure 4.1. A couple of boolean variables select the mode of operation; the variables are LV, to signal, if asserted, a low-voltage ride-through operation, and IS, to signal, if asserted, an islanded operation. The scheme supports the normal operation mode, the low-voltage ride-through operation mode, and the islanded operation mode.

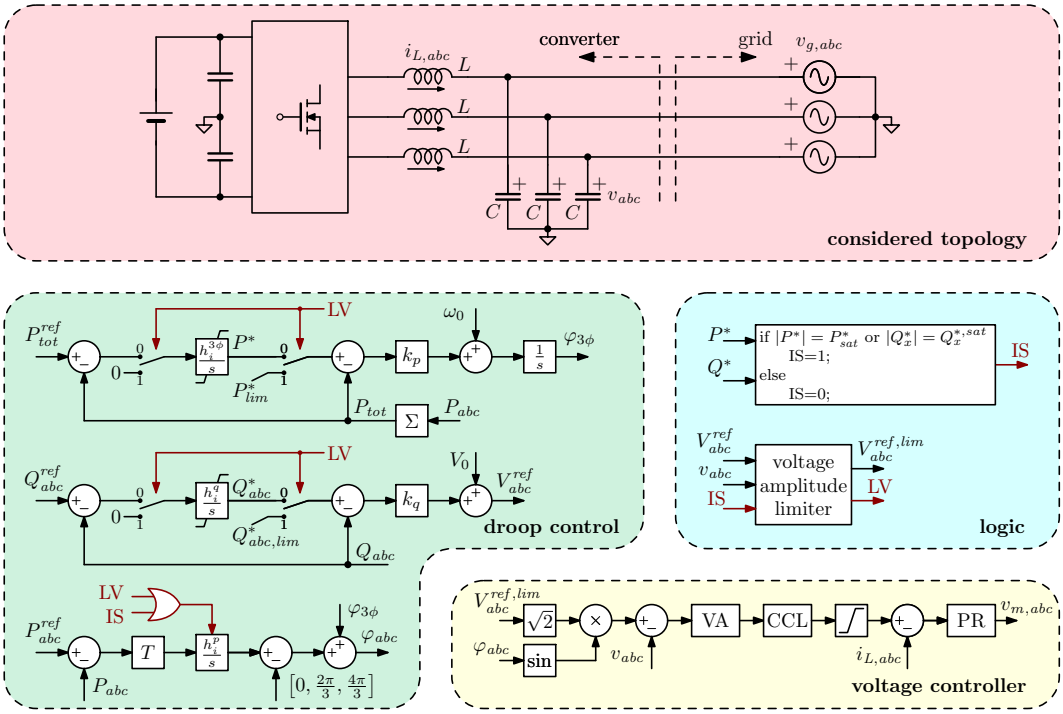

Figure 4.1: Proposed low-voltage ride through technique integrated in the control scheme described in [19].

4.2.1 Voltage Controller

The voltage controller is composed of an inner proportional-resonant current regulator, and an outer virtual admittance to emulate a mainly inductive output impedance around 50 Hz:

$$H_{\mathrm{VA}}(s) = \left(R_1 + \frac{sL_vR_2}{sL_v + R_2}\right)^{-1} = k_{\mathrm{VA}}\frac{1 + s/\omega_z}{1 + s/\omega_p} \tag{4.1}$$

with $k_{\mathrm{VA}} = 0.0942$, $\omega_p = 2\pi(5\,\mathrm{Hz})$, and $\omega_z = 2\pi(1\,\mathrm{kHz})$. Placing the pole away from the origin (i.e., adding R_1) allows to reject dc components due to grid disturbances, while the zero (i.e., non-infinite R_2) increases the closed-loop phase margin.

4.2.2 Basic Per-Phase Control Operation

During normal grid-tied operation, that is, with LV and IS equal to zero, the voltage reference signal is generated by the per-phase power control proposed in [19]. Such a control features active and reactive output power tracking for each of the three EPC phases during grid-connected operation and smooth transitions and operation in islanded conditions. By the per-phase power control, the P-f droop-law is implemented considering the total output active power:

$$\omega = \omega_0 + k_p(P^* - P_{\mathrm{tot}}) \tag{4.2}$$

and an outer loop regulates the value of P^* to track the reference signal $P_{\mathrm{tot}}^{\mathrm{ref}}$, which is the sum of the per-phase reference signals P_{abc}^{ref}. This generates the instantaneous phase signal $\varphi_{3\phi}$. While the frequency must be the same for all the phases, the voltage amplitudes may differ, allowing the implementation of a Q-V droop law phase-by-phase:

$$V_x^{\mathrm{ref}} = V_0 + k_q\left(Q_x^* - Q_x\right), \quad x = a, b, c \tag{4.3}$$

An outer regulation loop adjusts Q_x^* in order to track the reference signals Q_x^{ref}, $x = a, b, c$. This generates the per-phase voltage amplitude reference signals V_{abc}^{ref}. Finally, a per-phase regulation loop generates the phase signals φ_{abc}. During normal operation, the signals LV and IS are zero, and $V_{abc}^{\mathrm{lim}} = V_{abc}^{\mathrm{ref}}$.

When the main grid is disconnected, the island condition is reached, and converters must promptly identify it, to take appropriate control actions. In this case, the slack-bus action of the main grid is lost and power control is no longer possible. The variables P^* and Q_{abc}^* start diverging until the integrators reach the saturation limits ($\pm P^{*,\mathrm{sat}}$ or $\pm Q_{abc}^{*,\mathrm{sat}}$). At this point, the signal IS is asserted, the per-phase

active-power regulation is deactivated, and the system works with fixed droop laws:

$$\begin{cases} \omega & = \omega_0 + k_p\left(\pm P^{*,sat} - P_{\text{tot}}\right) \\ V_x^{\text{ref}} & = V_0 + k_q\left(\pm Q_x^{*,sat} - Q_x\right) \qquad x = a, b, c \end{cases} \tag{4.4}$$

The EPC behavior is then adapted to contribute to forming the voltage of the islanded system.

As presented, the controller does not adequately behave in case of voltage dips, as any other strategies based on the traditional droop control.

4.3 Proposed Low-Voltage Ride Through Strategy

The strategy described in the following is applied to the control structure described in the previous section and endows it the capability of *i)* limiting the output currents during voltage disturbances; *ii)* avoiding transient instability and reducing post-fault transients; *iii)* preserving the voltage regulation performances; *iv)* supporting the islanded operation.

4.3.1 Output Current Limitation

The output current limitation is achieved first by a hard current limiter, which is the solution with the fastest response time. Then the CCL measures the peak current value in each phase current reference and provides a different limiting gain for each of the phases, such that:

$$k_{x,\text{lim}} = \begin{cases} I_{\text{max}}/\hat{I}_x^{\text{ref}} & \text{if } \hat{I}_x^{\text{ref}} > I_{\text{max}} \\ 1 & \text{otherwise} \end{cases} \tag{4.5}$$

The CCL limits the currents after less than a grid cycle, reason why the hard current limiter is actually activated only for a short amount of time.

4.3.2 Robustness Against Transient Instability

To increase the robustness against transient instability, it is necessary to limit the angle displacement between the converter and the grid during the voltage dips. This not only prevents transient instability, but allows a faster resynchronization

after the voltage disturbance. If δ is this angle displacement, then:

$$\frac{d\delta}{dt} = \omega_0 - \omega_g + k_p(P^* - P_{\text{tot}}) \tag{4.6}$$

where ω_g is the grid angular frequency. Being the per-phase current limited to $I_{\max}$, then the maximum output power is reduced during the voltage dip, leading to an increase of (4.6). This can be eluded by decreasing the value of P^* based on the level of the voltage dip. Assuming that $S_n/3$ is the nominal per-phase output power, in the presence of voltage dips S_n should decrease to:

$$S_{n,\text{lim}} = \frac{S_n}{3} \cdot \left(\sum_{x=a,b,c} \frac{V_x}{V_0} \right) \tag{4.7}$$

where V_x is the measured rms voltage at phase x. For this reason, P^* is then limited to:

$$P^*_{\text{lim}} = \begin{cases} S_{n,\text{lim}} \cdot \text{sign}(P^*) & \text{if } |P^*| > S_{n,\text{lim}} \\ P^* & \text{otherwise} \end{cases} \tag{4.8}$$

4.3.3 Restoration of Voltage Regulation Capabilities

The larger the current references, the smaller the CCL gain cascaded to the virtual admittance block or, equivalently, the voltage regulator. This results in an overall lower equivalent output admittance or, equivalently, a lower voltage regulator gain; in both cases, the EPC capability of regulating the output voltage is lessened. To limit the magnitude of the current references, the voltage reference signal should be adapted. The previous subsection is a step toward this goal, however the voltage magnitude should be limited as well.

The voltage amplitude is limited here by limiting the value of Q^*_{abc}, and by directly limiting the amplitude of the voltage via a voltage limiting gain (VLG). The combination of the two provisions limits the current references and also mitigates the reactive power disturbances.

Let us consider $Q^*_{abc} = \left[Q^*_a, Q^*_b, Q^*_c\right]$ and $Q^* = \sum Q^*_x$, $x = a,b,c$. The maximum value of Q^* can be computed as:

$$Q^*_{\text{lim}} = \left(1 + \frac{\omega_0 L_v}{k_q V_0}\right) \sqrt{S^2_{n,\text{lim}} - P^{*2}_{\text{lim}}} \tag{4.9}$$

where the term in the brackets compensates for the static error of the transfer

function from Q_x^* to Q_x. It is possible to limit Q_{abc}^* as:

$$Q_{abc\text{lim}}^* = \begin{cases} Q_{abc}^* \cdot \frac{Q_{\text{lim}}^*}{Q^*} & \text{if } |Q^*| > Q_{\text{lim}}^* \\ Q_{abc}^* & \text{otherwise} \end{cases} \tag{4.10}$$

To limit the voltage amplitude level, the VLG is computed according to the output voltage level. When designing droop controller, one assumes a tolerable voltage amplitude deviation level ΔV. Here, this value is used as a threshold for the activation of the voltage amplitude limiter (VAL):

$$V_x^{\text{ref,lim}} = \begin{cases} V_x^{\text{ref}} \cdot \frac{V_x}{V_0}\left(1+\frac{\Delta V}{V_0}\right) & \text{if } V_x\left(1+\frac{\Delta V}{V_0}\right) < V_0 \\ V_x^{\text{ref}} & \text{otherwise} \end{cases} \tag{4.11}$$

for $x = a, b, c$, where V_x is the measured rms voltage at phase x. In the first case of (4.11), the signal LV is set to asserted.

4.3.4 Management of Islanded Operation

Voltage amplitude limitation is based on measured output voltage: this could bring the voltage amplitude to zero if the limiter is triggered when it is the converter itself imposing the output voltage, as in islanded operation. For this reason, in case the islanded operation signal IS is asserted, the block VAL is deactivated, and $V_{abc}^{\text{ref,lim}} = V_{abc}^{\text{ref}}$.

Otherwise, during grid-tied operation, if a voltage disturbance happens, it could last long enough that either P^* or Q_{abc}^* reach the saturation level. To avoid this situation, which would deactivate the VAL, the input of integrators computing P^* and Q_{abc}^* are clamped to 0 when LV is asserted. Remarkably, this is possible because the identification of a voltage disturbance by the VAL is much faster (i.e., less than a grid cycle) than the identification of the islanded operation.

4.4 Simulation Results

The proposed LVRT strategy is tested in simulation considering two different scenarios, and is compared with the controller in [19] implementing just the CCL. The considered topology is depicted in Figure 4.1, with the parameters reported in Table 4.1. These simulations are meant to highlight the advantages of the proposed strategy in terms of output power regulation and prompt recovery after the voltage dip event, compared to a CCL-only strategy.

Parameter	Symbol	Value	
Output inductor	L	340	µH
Output capacitor	C	5.7	µF
Virtual inductor	L_v	3	mH
Virtual resistor 1	R_1	94.2	mΩ
Virtual resistor 2	R_2	18.8	Ω
Nominal power	S_n	3	kVA
Grid nominal rms voltage	V_0	110	V
Grid nominal frequency	ω_0	$2\pi 50$	rad s^{-1}
P-f droop coefficient	k_p	0.698	mrad/(Ws)
Q-V droop coefficient	k_q	1.83	mV VAr^{-1}
Total active power integral gain	$h_i^{3\phi}$	10	s^{-1}
Reactive power integral gain	h_i^q	30	s^{-1}
Per-phase integral gain	h_i^p	1	mrad/(Ws)

Table 4.1: Parameters of the system under consideration.

4.4.1 Balanced Voltage Dip

The first test consists of a 50% balanced voltage dip lasting 1.5 s. The resulting waveforms are reported in Figure 4.2(a). The proposed strategy effectively prevents transient instability, which otherwise leads to long re-synchronization time after the fault and high power disturbances. Such an undesired behavior is actually observed in the waveforms related to the case with the LVRT strategy disabled. The mitigation is due both to the clamping strategy on the P^* and Q^*_{abc} integrators, and to the voltage limiting strategy that reduces the static error of the droop regulation.

The recovery time T_{rec} after the voltage dip is reduced, from $T_{\text{rec}} = 2.2$ s without LVRT strategy to $T_{\text{rec}} = 0.6$ s using the proposed method.

4.4.2 Unbalanced Voltage Dip

The second test consists of a 50% voltage dip on phase b lasting 1.5 s, while the other phases are unaffected. The resulting waveforms are reported in Figure 4.2(b). The proposed strategy effectively limits the angle drift between the converter and the grid, mitigating power disturbances and increasing the robustness against transient instability. In this case too, the recovery time after the voltage dip is reduced using the proposed strategy: from $T_{\text{rec}} = 0.75$ s to $T_{\text{rec}} = 0.4$ s.

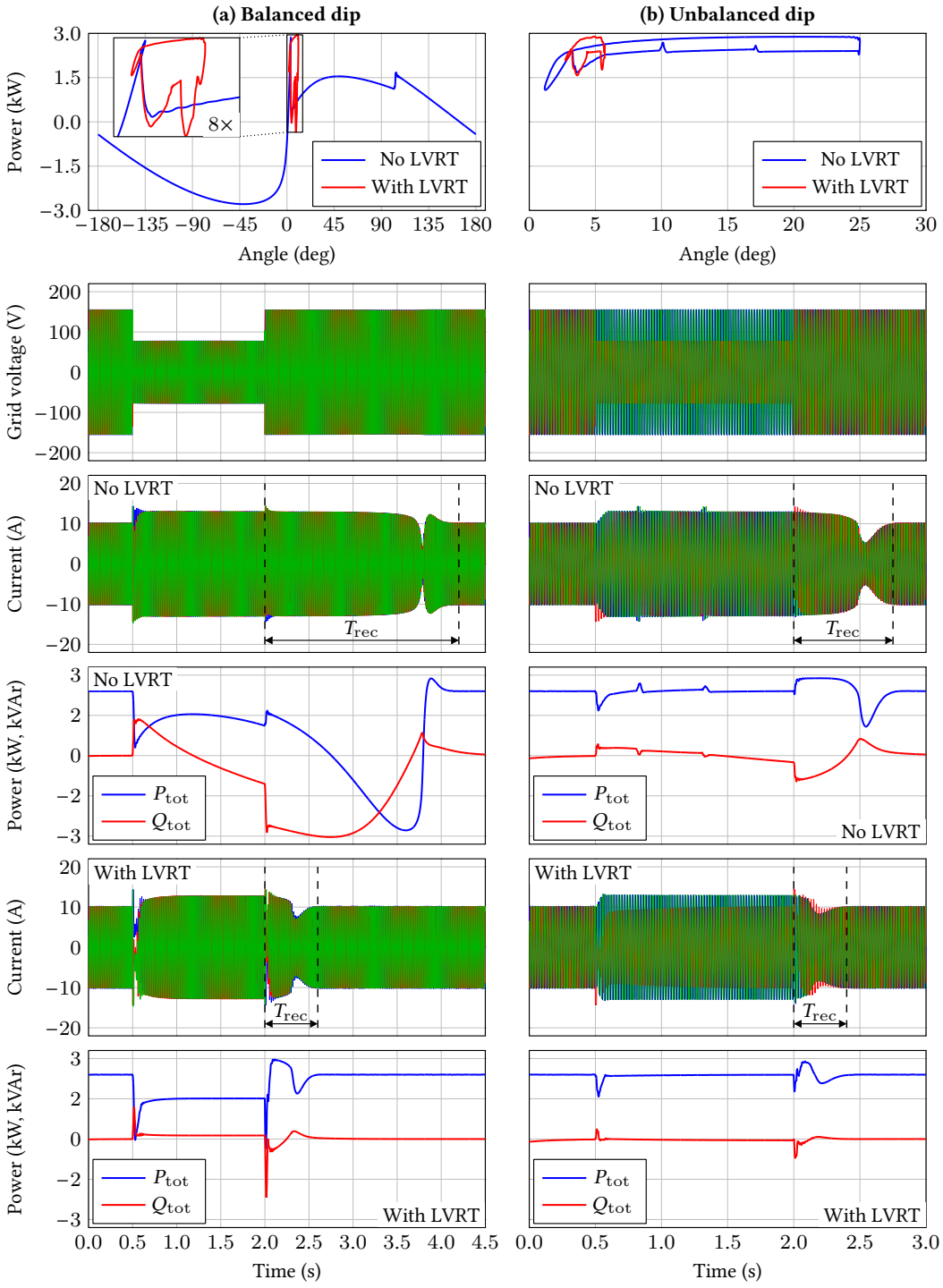

Figure 4.2: Simulation tests of the proposed LVRT strategy. (a) shows the proposed strategy under a 1.5 s 50% balanced voltage dip. (b) shows the strategy under a 1.5 s 50% voltage dip on phase *b*, leaving the other phases unaffected. The plots on the first row show the power-angle trajectories of the droop controller during the fault; PCC voltages are shown on the second row. Third and fourth rows show, respectively, output currents and output powers with just the current limiter, without any fault ride-through strategy. The same quantities are shown in fifth and sixth rows, for the proposed strategy.

4.5 Experimental Tests

Experimental tests have been conducted on a 3 kVA grid-forming converter, implementing the proposed strategy. The setup consists of two rapid prototyping systems [61], one constituting the grid-forming converter under test, the other performing as grid emulator and imposing the grid voltage. The converter has parameters as shown in Table 4.1.

4.5.1 Balanced Voltage Dip

The first test is a balanced 50% voltage dip, lasting 1.5 s. Initially, the converter is in steady-state, injecting a balanced active power of 1 kW into the grid. The results are shown in Figure 4.3(a). The top plot shows the output power, the middle plot shows the output voltage, while the bottom one shows the output currents. The proposed strategy effectively limits the output current, restoring the full voltage control capabilities during the voltage dip, and allows a prompt recovery after the dip. The non-ideal grid, with its non-zero impedance, lowers the actual phase-margin in the droop-loop, leading to a slightly longer time to reach the same steady-state condition as before the voltage dip (around 0.8 s in this case).

4.5.2 Unbalanced Voltage Dip

The second test is a 50% voltage dip on phase b solely, lasting 1.5 s. As in the balanced test, the converter is initially injecting 1 kW active power into the grid. The results are shown in Figure 4.3(b). The system is shown to correctly ride-through the voltage dip, limiting the output current and recovering promptly after the fault.

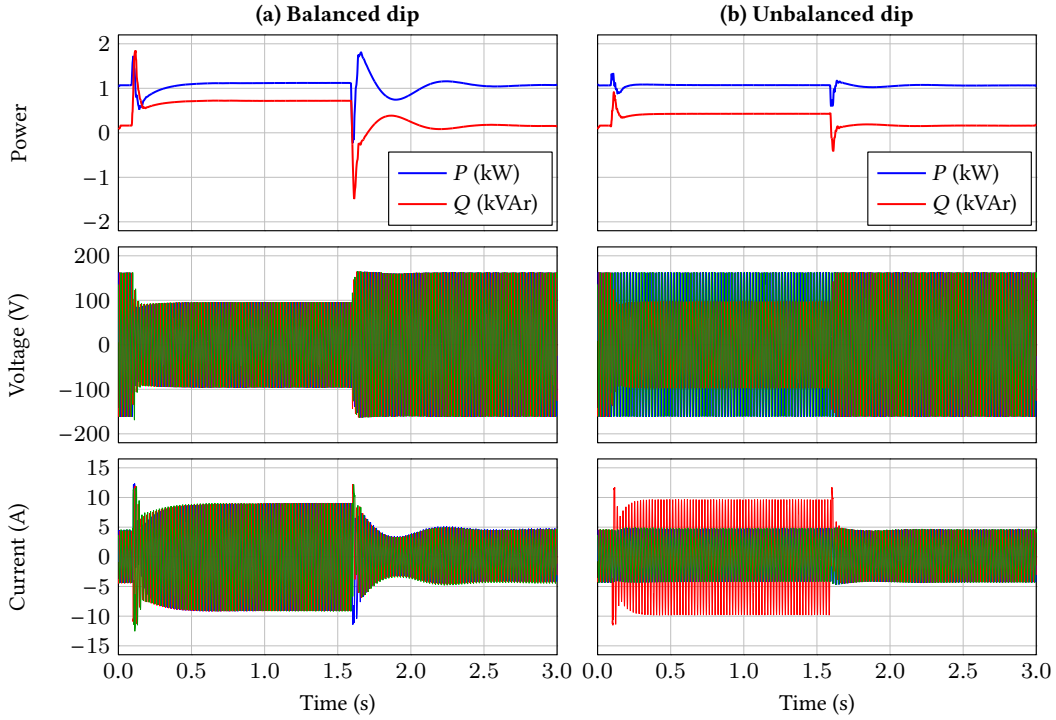

Figure 4.3: Experimental results of the proposed LVRT strategy. (a) 1.5 s 50% balanced voltage dip. (b) 1.5 s 50% voltage dip on phase *b*.

4.6 Summary

In this chapter:

- a technique that permits a safe and stable low-voltage ride-through of three-phase inverters that implement the per-phase power control is presented;
- the mechanisms that limit output current, prevents transient instability, and restore voltage regulation capability are described;
- the advantages of the proposed technique with respect to simple current limitations are shown in simulation;
- the method is validated in experimental tests, using a 3 kW rapid prototyping system.

5 Primal-Dual Based Coordination

This chapter presents a method for the coordination of multiple electronic power converters in microgrids. Leveraging on the degrees of freedom unlocked by control techniques such as the one proposed in Chapter 2 or in Chapter 3, this method allows to optimize on the microgrid operation acocunting for the converter losses, and mitigating the unbalance at the PCC. Section 5.2 describes the considered scenario and control problem, which is solved by the optimization method presented in Section 5.3. Section 5.4 describes the experimental setup used to derive a cost function representing converters' power losses, herein considered to demonstrate the proposal. Section 5.5 illustrates the specific implementation of the proposed primal-dual based coordination method. The method is verified in Section 5.6, which also describes the simulation tests and benchmark used for the validation.

5.1 Introduction

The wide selection of control techniques for EPCs creates new degrees of freedom in the management of electrical quantities. The ability to perform unbalance regulation in three-phase EPCs, which is easily supported by grid-following converters, has also been demonstrated in grid-forming converters [12, 19, 20, 53, 72].

The goal of this research is to explore the optimal exploitation of the control flexibility of EPCs in pursuing valuable services for the upstream grid, such as, power loss reduction and unbalance compensation at the PCC with the main grid. This should be done without altering the active power flow, typically driven by other economic-related or energy-related requirements [73, 74, 75, 76, 77, 78, 79, 80, 81, 82, 83].

Several approaches in the literature aim at optimizing the operation of EPCs in microgrids. Some focus on microgrids connected to upstream grids, which typically prioritize energy management aspects and target transactive operations (e.g., optimal bidding or energy scheduling) [73, 75, 77, 78, 82, 83], or ancillary services markets such as frequency/voltage regulation [73, 74, 75, 76, 78, 81, 82]. However, since energy exchange is not directly related to unbalanced and reactive power, dedicated optimization strategies are required.

The method proposed in [84] mitigates the voltage unbalance by minimizing

the sum of squared negative-sequence components. Still, the objective should also consider the impact on the distributed EPCs to optimize the compensation effort. A model-free consensus-based power control algorithm is proposed in [85], where a power-sharing proportional to the generators capabilities is achieved, focusing on the compensation of current unbalance at the PCC. A multiobjective optimization approach is proposed in [86], which includes stochastic aspects. The approach targets benefits in costs, reliability, and impact on the environment; the voltage unbalance is constrained inside tolerance bands. In [87], two different control levels realize voltage unbalance compensation. A bus is selected as critical, and its compensation is achieved by the lowest control level, equally sharing the compensation effort among units. Then the higher level corrects unbalance factors at other buses, bringing their value within tolerance bands; the method considers islanded operation.

None of the aforementioned methods considers that changing the operating point of distributed EPCs affects the efficiency of the generation units and, consequently, the overall system losses. Converter losses are usually modeled as quadratic functions, and Lagrange-multipliers based methods are commonly employed when solving such problems [88]. In [89], the optimal sharing of current among distributed converters is computed by solving in closed-form the Lagrange-multipliers problem. The approach is limited to the provision of active and reactive power in grid-tied operation. In [90], the Lagrange-multipliers problem is formulated to compute the droop coefficients that optimally share the reactive power in single-phase islanded microgrids. The problem is then solved iteratively using the dual-ascent algorithm.

Here, a technique based on dual-ascent algorithm is employed. The proposed methodology is applied in the outlined scenario, contributing in:

1. a primal-dual coordination algorithm for the optimal coordination of distributed power converters in three-phase microgrids;

2. formulating the control problem to provide services like reactive and unbalanced currents while minimizing power losses and avoiding constraining the active power flows;

3. demonstrating the operation of the algorithm considering a cost function including the converters' power losses with respect to the operating point.

The method proposed herein minimizes the overall power losses, allowing to choose whether or not to constrain the PCC current flow to be perfectly balanced, with no reactive power flow. Remarkably, different convex cost functions can be considered, allowing the employment of the presented method in a vast class of problems.

5.2 Problem Description

5.2.1 Assumptions

Figure 5.1 shows a typical application scenario for the proposed method. The microgrid is composed of N_x controllable units $\boldsymbol{x}_i$ and N_u uncontrollable units $\boldsymbol{u}_i$. The following assumptions are made:

1. a central microgrid controller (MC) is present, capable of exchanging information with the controllable units $\boldsymbol{x}_i$, $i = 1, \ldots, N_x$, by low-bandwidth communication;
2. controllable units exploit the communication link to send to the MC data about their cost function and operating point;
3. periodically, the MC runs an optimization algorithm, and then dispatches optimal reference values to the controllable units;
4. phasors representing the voltages at the nodes of the grid have approximately equal phases along the distribution lines.

By assumption 4), it is possible to consider active power equivalent to positive-sequence d-axis current (i.e., active current), as done in other works, like [33, 40]. This is also valid for reactive power and q-axis current (i.e., reactive current), recalling that the reactive power is proportional to $-I_q^+$, according to common definitions of reactive power with d-axis aligned to grid voltage phasor and q-axis leading it by 90°. It is worth noting that the method pursued herein deals with quantities at the fundamental frequency, for which quantities like reactive power and unbalance are defined. Distributed converters are assumed to be capable of tracking given current references, no other assumptions are necessary on the converters local controllers.

Let $\boldsymbol{x} \triangleq \left[\boldsymbol{x}_0, \ldots, \boldsymbol{x}_i, \ldots, \boldsymbol{x}_{N_x}\right]^\top \in \mathbb{R}^{(N_x+1)\times 1}$ be the column vector of all the optimization variables, with $\boldsymbol{x}_i = \left[I_{q,i}^+, I_{d,i}^-, I_{q,i}^-, I_{d,i}^0, I_{q,i}^0\right] \in \mathbb{R}^{1\times 5}$, namely, the rms value of the positive sequence reactive current, of the negative sequence d and q currents, the zero sequence d and q currents. Vector $\boldsymbol{x}_0$ collects the same quantities measured at the PCC. Notice that the PCC can be regarded, as commonly done, as a slack bus that provides the mismatch between absorbed and injected currents. Consequently, its contribution can be indirectly controlled by choosing the operating points $\boldsymbol{x}_i$, $i = 1, \ldots, N_x$, since (5.4) holds. For this reason, the PCC is included among the controllable units. The vectors containing quantities referring to uncontrollable units

are defined as $\boldsymbol{u}_i \triangleq \left[\tilde{I}^+_{q,i}, \tilde{I}^-_{d,i}, \tilde{I}^-_{q,i}, \tilde{I}^0_{d,i}, \tilde{I}^0_{q,i}\right] \in \mathbb{R}^{1\times 5}$, where $\tilde{\cdot}$ denotes a non-controllable quantity.

5.2.2 Cost Function

The goal of the method is to optimally provide controllable quantities, minimizing herein a cost function representing power losses. Other cost functions may be considered for the implementation of the approach.

The considered cost function accounts for converter losses and the power losses at the PCC interface as:

$$F(\boldsymbol{x}) = P^0_{\text{loss}}(\boldsymbol{x}_0) + \sum_{i=1}^{N_x} P^i_{\text{loss}}(\boldsymbol{x}_i) \tag{5.1}$$

where $P^0_{\text{loss}}(\boldsymbol{x}_0)$ is the term accounting for PCC interface losses, while $P^i_{\text{loss}}(\boldsymbol{x}_i)$, $i = 1, \ldots, N_x$ is the power loss of the i-th converter. The modeling of converter losses will be discussed in the next section. Regarding losses at PCC interface, a grid resistance R_g is assumed. To model loss terms it is convenient to define an extended vector $\boldsymbol{x}^e_i \in \mathbb{R}^{1\times 6}$ formed of $\boldsymbol{x}_i$ plus the extra element $I^+_{d,i}$:

$$\boldsymbol{x}^e_i = \left[I^+_{d,i}, \boldsymbol{x}_i\right] = \left[I^+_{d,i}, I^+_{q,i}, I^-_{d,i}, I^-_{q,i}, I^0_{d,i}, I^0_{q,i}\right] \tag{5.2}$$

Then, the losses on the grid resistance can be modeled as

$$P^0_{\text{loss}}(\boldsymbol{x}_0) = 3R_g\left\|\boldsymbol{x}^e_0\right\|^2 \tag{5.3}$$

where $\|\cdot\|$ denotes the 2-norm operator.

5.2.3 Constraints

The considered microgrid is populated by uncontrollable units, which include loads (e.g., households, offices) and generators (e.g., wind turbines, photovoltaic panels), and by controllable units. In addition, the microgrid is tied to the main grid at the PCC. By the Kirchhoff current laws, the total contribution from the grid and the controllable units must sum to the net power absorption by the uncontrollable units $\boldsymbol{g} \in \mathbb{R}^{5\times 1}$:

$$\boldsymbol{g}^\top = \sum_{i=1}^{N_u} \boldsymbol{u}_i = \boldsymbol{x}_0 + \sum_{i=1}^{N_x} \boldsymbol{x}_i \tag{5.4}$$

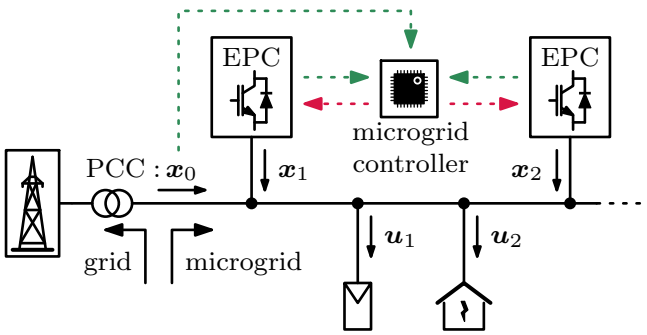

$$\text{controllable: } \boldsymbol{x}_i = \left[I^+_{q,i}, I^-_{d,i}, I^-_{q,i}, I^0_{d,i}, I^0_{q,i}\right]$$
$$\text{uncontrollable: } \boldsymbol{u}_i = \left[\tilde{I}^+_{q,i}, \tilde{I}^-_{d,i}, \tilde{I}^-_{q,i}, \tilde{I}^0_{d,i}, \tilde{I}^0_{q,i}\right]$$

Figure 5.1: Typical application scenario for the proposed approach. Dashed paths represent communication links.

Being $\boldsymbol{x} = \left[\boldsymbol{x}_0, \boldsymbol{x}_1, \ldots, \boldsymbol{x}_{N_x}\right]^\top$, it is possible to impose the constraint (5.4) as $\boldsymbol{G}\boldsymbol{x} - \boldsymbol{g} = \boldsymbol{0}$, with

$$\boldsymbol{G} = [\underbrace{\boldsymbol{I}_{5\times5}, \boldsymbol{I}_{5\times5}, \ldots, \boldsymbol{I}_{5\times5}}_{(N_x+1) \text{ times}}] \tag{5.5}$$

where $\boldsymbol{I}_{5\times5}$ is the identity matrix of size 5-by-5, being 5 the number of quantities contributed by each unit.

Converters have a maximum rated output current on each of its phases (i.e., phase a, b, and c). The algorithm shall not compute solutions where the reference values lead converters outside their safe operating region. Assuming a maximum output current on each phase $I_{\text{max},i}$ for the i-th converter, the following constraint should be met:

$$I^2_{a,i}, I^2_{b,i}, I^2_{c,i} \leq I^2_{\text{max},i} \tag{5.6}$$

with $i = 1, \ldots, N_x$. The next step is to determine the value of $I^2_{a,i}, I^2_{b,i}, I^2_{c,i}$ from the vectors $\boldsymbol{x}^e_i$. By using suitable matrices $\boldsymbol{A}, \boldsymbol{B}, \boldsymbol{C} \in \mathbb{R}^{6\times6}$, it yields:

$$\begin{aligned} I^2_{a,i} &= \boldsymbol{x}^e_i \boldsymbol{A} \left(\boldsymbol{x}^e_i\right)^\top \\ I^2_{b,i} &= \boldsymbol{x}^e_i \boldsymbol{B} \left(\boldsymbol{x}^e_i\right)^\top \\ I^2_{c,i} &= \boldsymbol{x}^e_i \boldsymbol{C} \left(\boldsymbol{x}^e_i\right)^\top \end{aligned} \tag{5.7}$$

The definition (A.3) and derivation of these matrices is reported as an appendix at the end of this chapter.

To provide services to the upstream grid by exploiting the resources installed within the microgrid, additional constraints can be imposed, to achieve desired operating modes. In this chapter, the following additional operating modes are considered:

1. zero reactive power flow at the PCC;
2. perfectly balanced currents at the PCC.

Achieving 1) means that the first element of $\boldsymbol{x}_0$ is null, because that element represents the reactive power exchanged at the PCC. Achieving 2) means that the last four elements of $\boldsymbol{x}_0$ are null, since they are related to negative and zero sequence currents exchanged at the PCC. These two operating modes can be obtained by adding additional constraints. To selectively activate the operating modes, two boolean inputs σ_1, σ_2 are used, where $\sigma_i = 1$ means that the i-th condition is enabled, otherwise $\sigma_i = 0$. The conditions 1) and 2) can be formulated as:

$$\boldsymbol{\sigma} \odot \boldsymbol{x}_0^\top = \boldsymbol{0} \tag{5.8}$$

where $\boldsymbol{\sigma} = [\sigma_1, \sigma_2, \sigma_2, \sigma_2, \sigma_2]^\top \in \mathbb{R}^{5\times 1}$, and $\odot$ indicates the element-wise multiplication (i.e., Hadamard product).

5.2.4 Problem Formulation

Based on the presented modeling, the optimization problem can be formulated as:

$$\begin{cases} \min\limits_{\boldsymbol{x}} & F(\boldsymbol{x}) \\ \text{s.t.} & \boldsymbol{G}\boldsymbol{x} - \boldsymbol{g} = \boldsymbol{0}; \\ & \boldsymbol{\sigma} \odot \boldsymbol{x}_0^\top = \boldsymbol{0}; \\ & \text{for } i = 1, \dots, N_x: \\ & \boldsymbol{x}_i^e \boldsymbol{A} \left(\boldsymbol{x}_i^e\right)^\top \leq I_{\max,i}^2 \\ & \boldsymbol{x}_i^e \boldsymbol{B} \left(\boldsymbol{x}_i^e\right)^\top \leq I_{\max,i}^2 \\ & \boldsymbol{x}_i^e \boldsymbol{C} \left(\boldsymbol{x}_i^e\right)^\top \leq I_{\max,i}^2 \end{cases} \tag{5.9}$$

It is worth to remark that, assuming F be a convex function, whose actual expression and derivation are shown in Section 5.4, and being the constraints convex, the optimization problem (5.9) is convex [88].

5.3 Solution Method

The solution method proposed herein is derived from *dual-ascent* technique. The resulting algorithm to solve the problem in (5.9) is described in this section, while its actual implementation is discussed in Section 5.5.

The dual-ascent method is an asymptotically optimal method to solve convex optimization problems using Lagrange multipliers [91, 92]. Dual-ascent is suitable for problems that exhibit a separable structure. In this case, the cost function is the sum of terms associated with different units, each depending solely on itself, so its application becomes natural.

Considering the problem in (5.9), its Lagrangian can be expressed as:

$$\begin{aligned}\mathcal{L}\{\boldsymbol{x},\boldsymbol{\lambda},\boldsymbol{\nu},\boldsymbol{\mu}\} = F(\boldsymbol{x}) + \boldsymbol{\lambda}^\top(\boldsymbol{G}\boldsymbol{x}-\boldsymbol{g}) + \\ + \boldsymbol{\nu}^\top\left(\boldsymbol{\sigma}\odot\boldsymbol{x}_0^\top\right) \\ + \boldsymbol{\mu}^\top(\boldsymbol{\Upsilon}_{\text{abc}}-\boldsymbol{\Upsilon}_{\text{max}})\end{aligned} \tag{5.10}$$

where $\boldsymbol{\lambda}\in\mathbb{R}^{5\times1}$, $\boldsymbol{\mu}\in\mathbb{R}^{3N_x\times1}$, and $\boldsymbol{\nu}\in\mathbb{R}^{5\times1}$ are column vectors containing Lagrange multipliers, and $\boldsymbol{\Upsilon}_{\text{abc}},\boldsymbol{\Upsilon}_{\text{max}}\in\mathbb{R}^{3N_x\times1}$ are the vectors containing the squares of the per-phase currents and maximum currents of all controllable units:

$$\boldsymbol{\Upsilon}_{\text{abc}} = \begin{bmatrix} I_{a,1}^2 \\ I_{b,1}^2 \\ I_{c,1}^2 \\ \vdots \\ I_{a,N_x}^2 \\ I_{b,N_x}^2 \\ I_{c,N_x}^2 \end{bmatrix}; \quad \boldsymbol{\Upsilon}_{\text{max}} = \begin{bmatrix} I_{\text{max},1}^2 \\ I_{\text{max},1}^2 \\ I_{\text{max},1}^2 \\ \vdots \\ I_{\text{max},N_x}^2 \\ I_{\text{max},N_x}^2 \\ I_{\text{max},N_x}^2 \end{bmatrix} \tag{5.11}$$

The dual-ascent is traditionally implemented by iteratively updating the solution $\boldsymbol{x}$ as follows:

$$\boldsymbol{x}(k+1) = \arg\min_{\boldsymbol{x}} \mathcal{L}\{\boldsymbol{x},\boldsymbol{\lambda}(k),\boldsymbol{\nu}(k),\boldsymbol{\mu}(k)\} \tag{5.12}$$

When the solution exists in closed form, (5.12) can be solved as $\nabla_{\boldsymbol{x}}\mathcal{L}=0$, as done in [90]. If a closed-form solution is not available, other strategies should be applied. A simplex method (see, e.g., [93]) is employed in [94] for solving (5.12); the drawback of that approach is the computation burden of the simplex algorithm's iterative nature, involved in each dual-ascent iteration.

Differently, it is worth noting that, even if the solution of $\nabla\mathcal{L}_{\boldsymbol{x}}=0$ can not be computed, it is still possible to compute the expression of $\nabla_{\boldsymbol{x}}\mathcal{L}$. By exploiting the

values of $\nabla_{\boldsymbol{x}}\mathcal{L}$, the update of $\boldsymbol{x}(k+1)$ can be performed by taking a finite number of steps in the opposite direction of $\nabla_{\boldsymbol{x}}\mathcal{L}$ with a fixed step-size. A single-step update is performed herein, obtaining:

$$\boldsymbol{x}(k+1) = \boldsymbol{x}(k) - \alpha\nabla_{\boldsymbol{x}}\mathcal{L}\{\boldsymbol{x}(k), \boldsymbol{\lambda}(k), \boldsymbol{\nu}(k), \boldsymbol{\mu}(k)\} \tag{5.13}$$

where α is the step size. Equation (5.13) resembles the updating step of the primal variable implemented in the primal-dual algorithm [95].

The update of the Lagrange multipliers for equality constraints is performed as:

$$\begin{cases} \boldsymbol{\lambda}(k+1) = \boldsymbol{\lambda}(k) + \beta[\boldsymbol{G}\boldsymbol{x}(k+1) - \boldsymbol{g}] \\ \boldsymbol{\nu}(k+1) = \boldsymbol{\nu}(k) + \delta\left[\boldsymbol{\sigma}(k) \odot \boldsymbol{x}_0^{\top}(k+1)\right] \end{cases} \tag{5.14}$$

where β, δ are the step sizes of the update. By Karush-Kuhn-Tucker (KKT) conditions, the update of the Lagrange multipliers related to inequality constraints has to be performed by setting 0 as their lower bound:

$$\boldsymbol{\mu}(k+1) = \min\{0,\ \boldsymbol{\mu}(k) + \gamma[\boldsymbol{\Upsilon}_{\text{abc}} - \boldsymbol{\Upsilon}_{\text{max}}]\} \tag{5.15}$$

where γ is the step size.

After the considerations done above, the $(k+1)$-th iteration of the primal-dual algorithm can be performed as:

$$\begin{cases} \boldsymbol{x}(k+1) = \boldsymbol{x}(k) - \alpha\nabla_{\boldsymbol{x}}\mathcal{L}\{\boldsymbol{x}(k), \boldsymbol{\lambda}(k), \boldsymbol{\nu}(k), \boldsymbol{\mu}(k)\} \\ \boldsymbol{\lambda}(k+1) = \boldsymbol{\lambda}(k) + \beta[\boldsymbol{G}\boldsymbol{x}(k+1) - \boldsymbol{g}] \\ \boldsymbol{\nu}(k+1) = \boldsymbol{\nu}(k) + \delta\left[\boldsymbol{\sigma}(k) \odot \boldsymbol{x}_0^{\top}(k+1)\right] \\ \boldsymbol{\mu}(k+1) = \min\{0,\ \boldsymbol{\mu}(k) + \gamma[\boldsymbol{\Upsilon}_{\text{abc}} - \boldsymbol{\Upsilon}_{\text{max}}]\} \end{cases} \tag{5.16}$$

5.4 Cost Function Based on Converter Losses

The power losses of a typical three-phase half-bridge topology have been characterized with respect to the operating conditions.

For a single-phase converter, power losses can be modeled as a quadratic function of the rms output current [90]:

$$P_{\text{loss}}^{1\phi} = a \cdot I_{rms}^2 + b \cdot I_{rms} + c \tag{5.17}$$

The topology considered herein is displayed in Figure 5.2.

The characterization for the three-phase converter aimed to find a fitting function

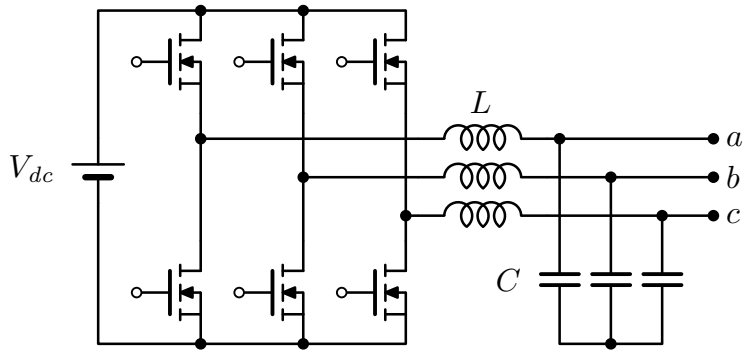

Figure 5.2: Topology considered for the power losses characterization.

f such that losses can be expressed as:

$$P^i_{\text{loss}} = f\left(I^+_{d,i}, I^+_{q,i}, I^-_{d,i}, I^-_{q,i}, I^0_{d,i}, I^0_{q,i}\right) \tag{5.18}$$

namely, as a function of dq components of symmetric sequences.

5.4.1 Overview of the Experimental Setup

A 3 kW experimental rapid prototyping system [61] has been employed to perform the characterization of the losses. Figure 5.2 shows the topology considered. A Dewesoft® Sirius-i data acquisition system is used to acquire the data and perform the computation of power loss, by means of the dedicated software run on a desktop PC. A 30 kW Cinergia® grid emulator is employed to emulate the ac side, while a Keysight® RP7962A is used as the dc source for the converter under test. A schematic representation of the setup is shown in Figure 5.3.

5.4.2 Power Losses Measurement

Power losses have been measured on the converter under test in about 4500 different operating points $\left[I^+_d, I^+_q, I^-_d, I^-_q\right] \in \mathbb{R}^4$. These points are determined by uniformly sampling $\mathbb{R}^4$ over the nominal converter ratings, removing all the points in which at least one of the per-phase currents exceeds the maximum value allowed. When steady state is reached, the converter losses are measured.

In light of the analysis done in [90], the following fitting function is considered:

$$f(|I|) = a \cdot |I|^2 + b \cdot |I| + c \tag{5.19}$$

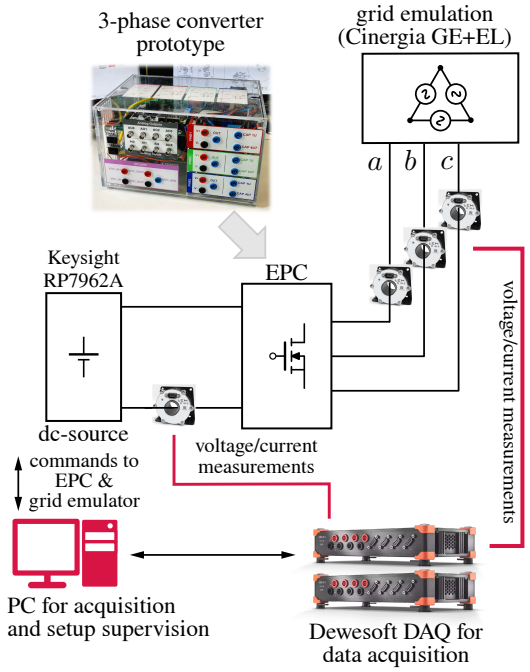

Figure 5.3: Schematic representation of the employed setup.

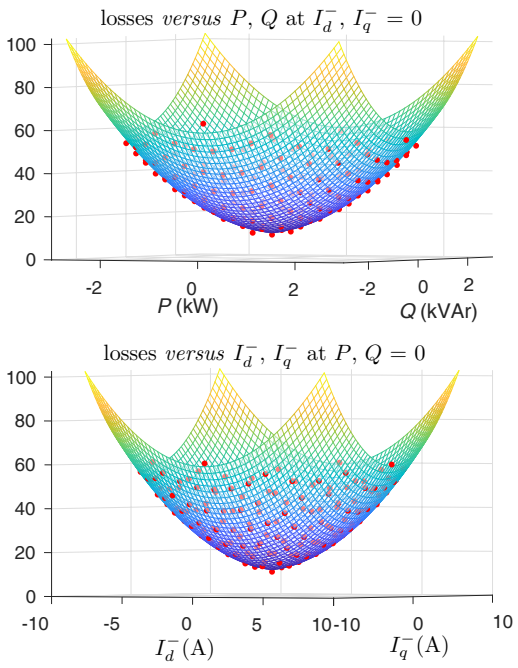

Figure 5.4: Experimental data (red dots) correctly fitted by the considered loss function Equation (5.19).

where $|I|^2 = \left|I_d^+\right|^2 + \left|I_q^+\right|^2 + \left|I_d^-\right|^2 + \left|I_q^-\right|^2$ is three-phase current mean-square value. The chosen function (5.19) correctly fits the measured data, as shown in Figure 5.4.

The expression in (5.19) shows the dependence of power losses on the rms three-phase current. Generalization of (5.19) may be possible considering also zero-sequence components. This latter case is included in this chapter assuming the model:

$$P_{\text{loss}}^i(I) = a_i \cdot |I_i|^2 + b_i \cdot |I_i| + c_i \tag{5.20}$$

where $|I_i|^2 = |I_{d,i}^+|^2 + |I_{q,i}^+|^2 + |I_{d,i}^-|^2 + |I_{q,i}^-|^2 + |I_{d,i}^0|^2 + |I_{q,i}^0|^2$.

5.5 Algorithm Implementation

A flowchart of the algorithm is shown in Figure 5.5. At the beginning, each controllable EPC sends to the MC the coefficients of its cost function a_i, b_i, c_i and the current operating point $\boldsymbol{x}_i^e$. The MC also receives the measured quantities at the PCC $\boldsymbol{x}_0^e$. It is assumed that the MC knows the maximum per-phase current $I_{\max,i}$ for each EPC.

As in (5.4), the MC can compute the value of $\boldsymbol{g}$ based solely on the operating points of the controllable units:

$$\boldsymbol{g}^\top = \boldsymbol{x}_0 + \sum_{i=1}^{N_x} \boldsymbol{x}_i \tag{5.21}$$

To compute the optimal solution, a fixed number of iterations $N_k = 1000$ is chosen, in which (5.16) is run. When N_k is reached, the current solution $\boldsymbol{x}(k)$ is dispatched as reference operating point for the EPCs. Then the algorithm is iterated. To better clarify all the steps involved more in detail, the pseudocode is shown in Algorithm 1.

As mentioned in Section 5.2, the approach assumes low bandwidth communication links between each controllable unit and the microgrid controller where the optimization algorithm is implemented. The execution rate of the algorithm is set to 6 executions per hour, which is suitable for the considered power profiles variation. Remarkably, the computational burden of such an algorithm allows a much higher execution rate on modern digital controllers, as further elaborated in Section 5.6. This allows sufficient time for the controller to receive the data from controllable units, compute and dispatch the new optimal solution, and allow converters to reach the new operating point. Remarkably, each execution is a different optimization problem. This allows interrupt-based variable-rate implementation, where the MC executes the optimization algorithm as soon as all the new data is

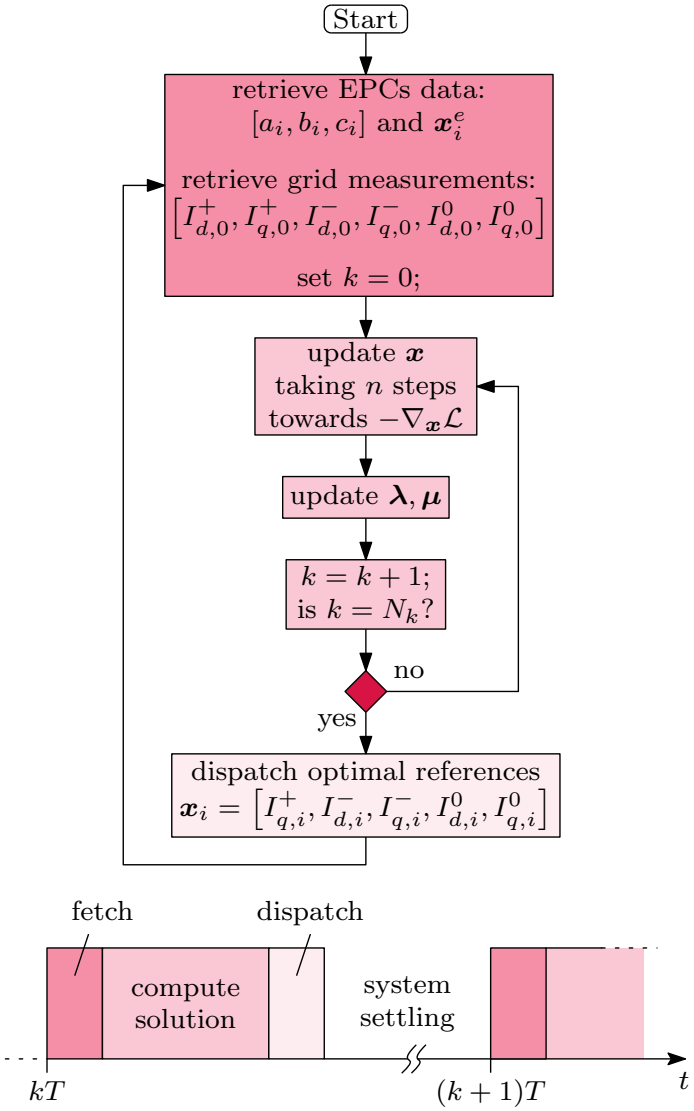

Figure 5.5: Flowchart of the proposed primal-dual based coordination algorithm. Temporal sequence of executed tasks represented on the bottom.

Algorithm 1: Pseudocode of the proposed approach, illustrated in Figure 5.5.

Start: go to Fetch
Fetch:
    Receive $\boldsymbol{x}_e^i$ and $[a_i, b_i, c_i]$ from EPCs
    Receive $\boldsymbol{x}_e^0$ from PCC
    Initialize $\boldsymbol{x}$ to system current state
    Compute $\boldsymbol{g}$ using (5.4)
    $k \leftarrow 0$
    go to **Compute**
Compute:
    Update $\boldsymbol{x}$ using (5.13)
    Update $\boldsymbol{\lambda}, \boldsymbol{\nu}$ using (5.14)
    Compute Υ_{abc} using (5.7) and (5.11)
    Update $\boldsymbol{\mu}$ using (5.15)
    $k \leftarrow k + 1$
    if $k < N_x$ **then**
        go to **Compute**
    else
        go to **Dispatch**
    end
Dispatch:
    Send optimal reference points to EPCs
    while *settling not reached* **do**
        wait
    end
    go to **Fetch**

received. Converters can manage their own settling time by sending the data only after their transient is completed.

5.6 Application Example

To show the effectiveness of the proposal, the low-voltage microgrid benchmark proposed by Cigre [55] is taken as a benchmark, and the proposed method is tested in a scenario where the units in the grid are provided with a varying power profile along 24 hours.

5.6.1 Benchmark Description

The microgrid, shown in Figure 5.6, is composed of unbalanced loads, wind turbines, photovoltaic panels, and energy storage systems (batteries). In the considered tests, only battery-sourced converters EPC1 and EPC2 are considered as dispatchable, so the algorithm runs optimizing their operating point. Loads and non-controllable converters are considered non-controllable units.

The loads and generators of the microgrid are considered with a variable power profile, along 24 hours. The photovoltaic sources, at nodes C and D, and wind turbines, at node E, in Figure 5.6, have power profiles obtained from real data [96] and [97], respectively, with nominal peak power as indicated in the same figure.

The loads in the microgrid are buildings, either residential or commercial. In particular, the loads at nodes D and E represent offices with three-phase connection, while each phase of all the other loads represents houses, each having an independent randomly generated power profile, which causes unbalanced power absorption considered the three-phase network. Load absorptions from offices and houses are generated using a Matlab-based app [98]. The nodes D and E have a power factor equal to 0.95, while all the other loads have a power equal to 0.85. Distribution lines are made of six different types of conductors, with R/X-ratio ranging from 1.76 to 7.48; the line impedance values are detailed in [55]. Finally, the active power of EPC1 and EPC2 are assumed to be managed by an energy management system, which supplies 15 kW active power during peak demand (i.e., from 6 a.m. to 6 p.m.) and recharges the batteries at 15 kW for the remaining time. The total power is then shared among EPC1 and EPC2 proportionally to their nominal powers.

The profiles for the various units in the microgrid are reported in Figure 5.7, where P_{loads} is the total power absorbed by the loads (i.e., offices and houses), P_{gen} is the generated power from PV panels and wind turbine, and P_{ems} is the total active power output of EPC1 and EPC2.

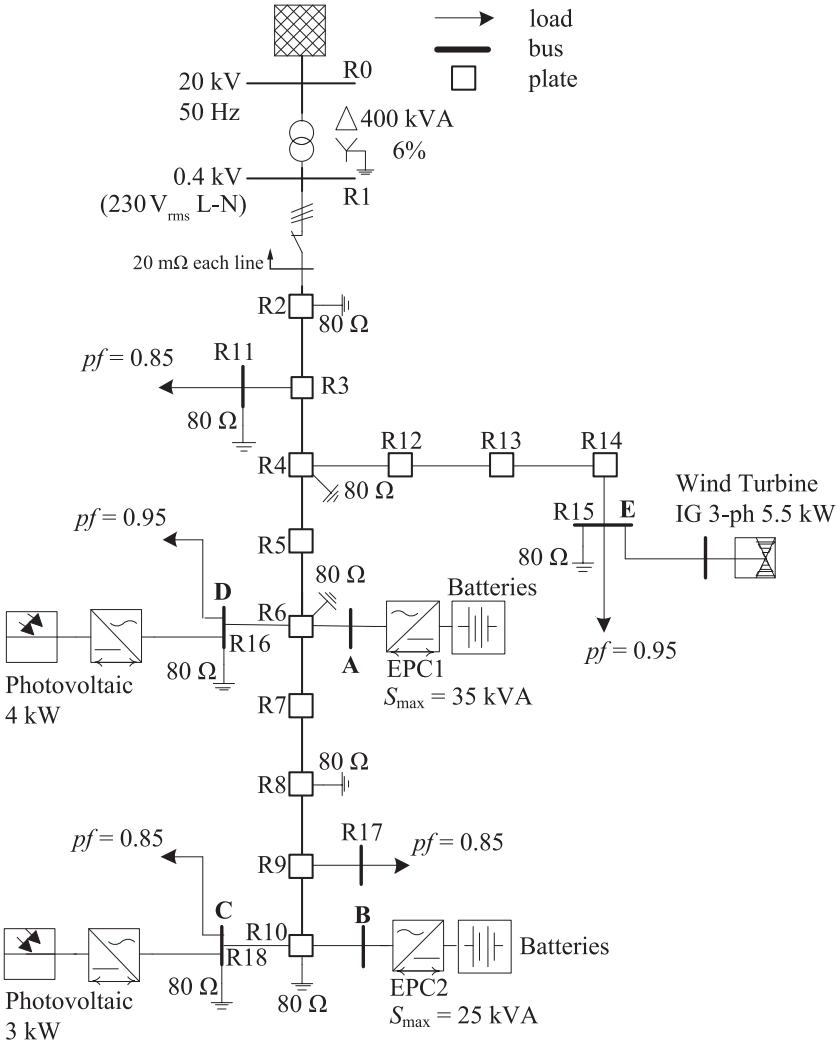

Converters Cost Functions

Grid resistance	R_g	20 mΩ
EPC1 cost function	$[a_1, b_1, c_1]$	[0.0411, 4.46, 123]
EPC2 cost function	$[a_2, b_2, c_2]$	[0.0797, 6.80, 114]

Figure 5.6: Considered microgrid benchmark, adapted from [55]. The table on the bottom illustrates the cost functions for the controllable units.

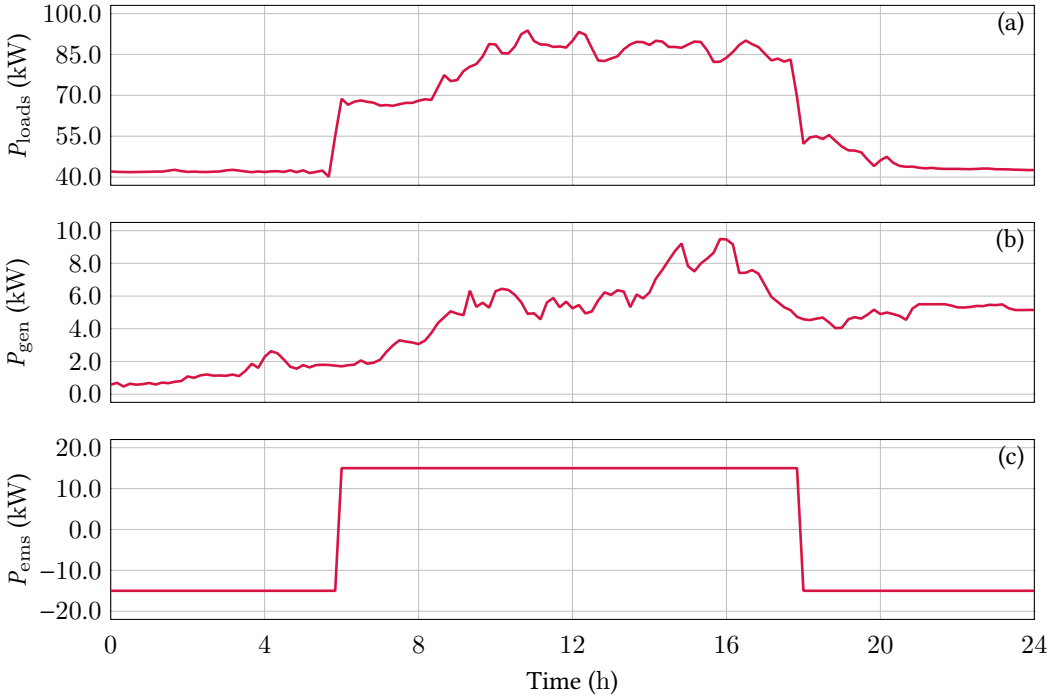

Figure 5.7: Aggregated active power profiles of units in the considered microgrid: (a) total power absorbed by the loads; (b) total power generated by renewable sources; (c) active output power of EPC1 and EPC2.

The coefficients a_i, b_i, c_i for controllable EPCs are derived from the efficiency curves versus percentage output power of two commercially available inverters, namely [99] for EPC1 and [100] for EPC2. From the efficiency curves, the curve of power loss with respect to three-phase rms current is derived, and fitted using (5.20) to obtain a_i, b_i, c_i. Figure 5.8 shows the efficiency data and the fitting curves. A 20 mΩ resistance is considered on each phase at the PCC to model grid losses.

5.6.2 Test Results

Four different scenarios are considered and compared in the following:

- **Case 1**: algorithm disabled, controllable EPCs only exchange active power as in Figure 5.7(c);
- **Case 2**: the algorithm provides optimal reference values to controllable EPCs;

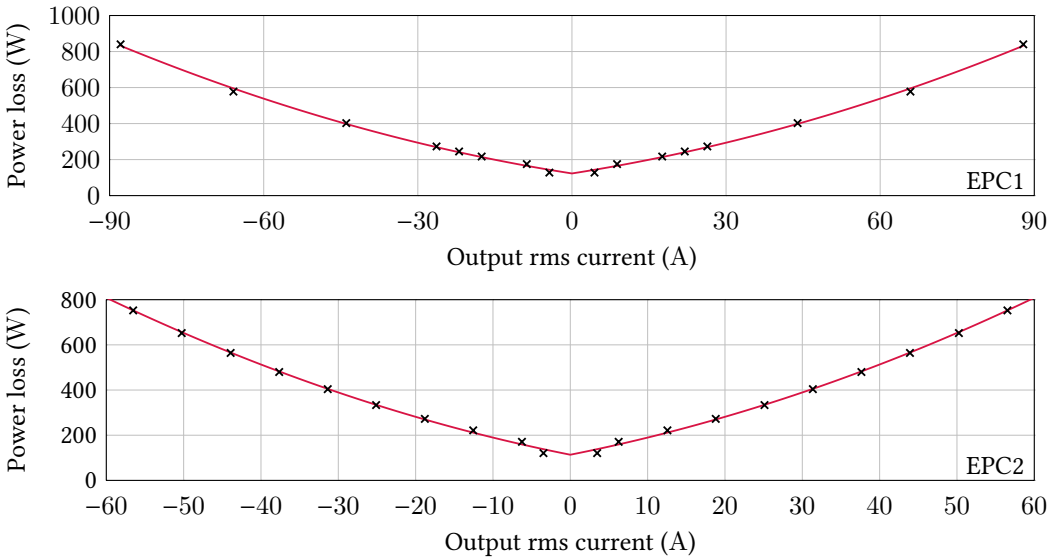

Figure 5.8: Efficiency curves (black crosses) from data reported in [99] and [100], respectively, and fitting curves (red curves) from Equation (5.20).

- **Case 3**: the algorithm provides optimal references to achieve balanced currents at PCC;
- **Case 4**: the algorithm provides optimal references to achieve balanced currents and zero reactive-power flow at PCC.

Figure 5.9 collects and allows the comparison of the results from the different test cases considered. To compute an unbalance factor that accounts for both negative and zero sequence currents, the following formula is used:

$$UF_{\%} = \frac{\sqrt{|I^{-}|^2 + |I^{0}|^2}}{|I^{+}|} \cdot 100 \tag{5.22}$$

The power factor is instead computed as PF $= P/S$.

The results show that the most efficient operation is achieved in **Case 2**, as expected. The power loss is reduced by more than 5% with respect to **Case 1**, during peak demand. It is worth remarking that the efficiency gains depend on the actual microgrid structure and operating conditions, and may vary based on the compensation effort required to the converters. In this case, the loads with higher power absorption present a higher power factor, namely, 0.95. Of course, if such a PF is decreased, then a greater reduction in losses is expected with respect

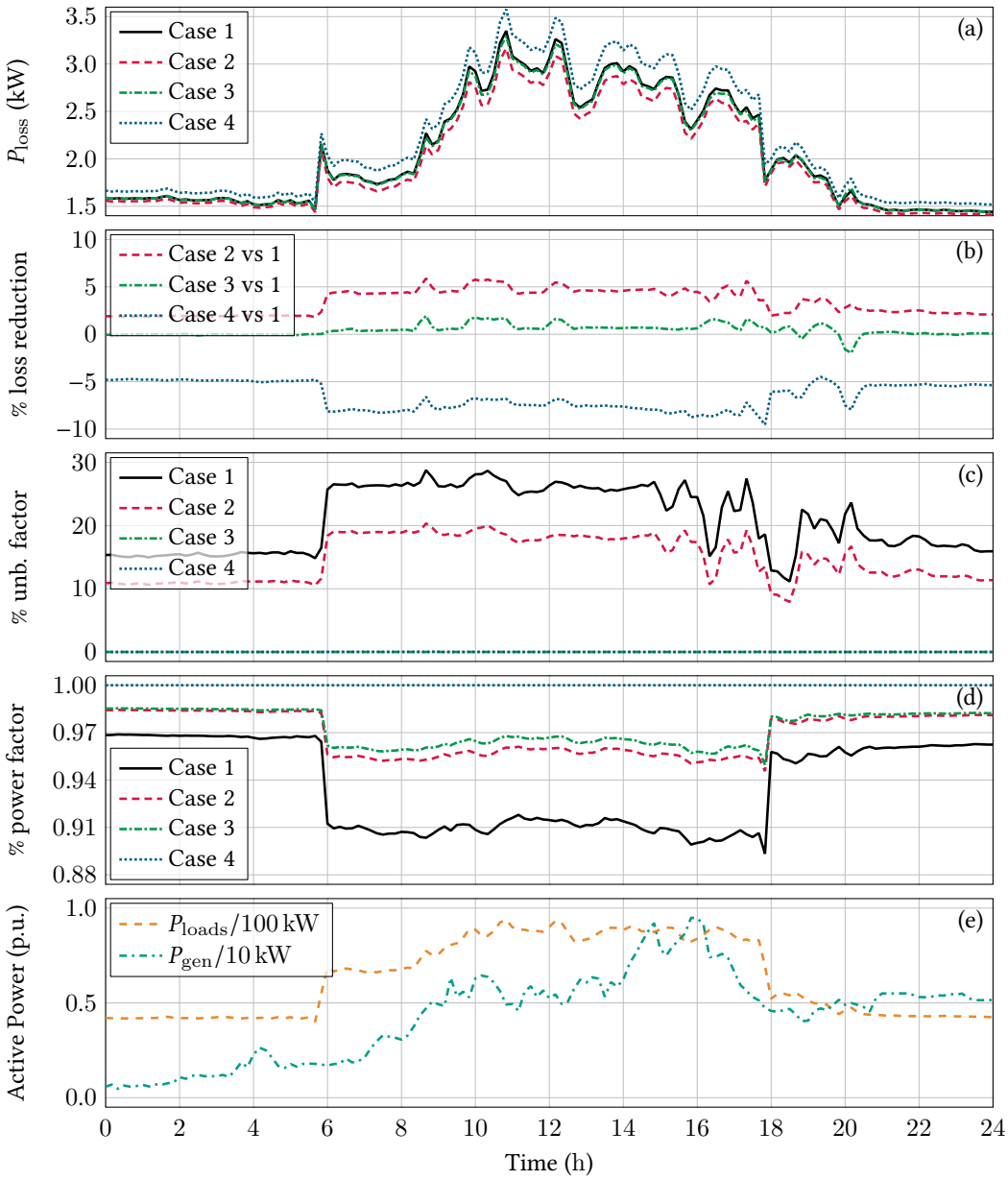

Figure 5.9: Simulation results: (a) total power loss of the system; (b) percentage loss reduction with respect to Case 1; (c) unbalance factor of currents at PCC; (d) power factor at PCC; (e) power demand and generation in the microgrid.

to **Case 1**. **Case 2** also leads to improvements in power factor and PCC current unbalance factor, because now part of the reactive power and unbalanced currents are provided by EPC1 and EPC2, thanks to the coordination algorithm.

Case 3 considers the service of imposing balanced current flow at PCC, by means of the constraints presented in Section 5.2-Section 5.2.3. This setting of the control algorithm achieves perfectly balanced currents at the PCC, while limiting the power loss.

Finally, operation in **Case 4** allows to achieve unitary power factor at the PCC, with PCC currents perfectly balanced. This operation mode engages the distributed controllable units with a higher effort, which brings to a loss increase with respect to **Case 1**. In fact, this mode of operation requires EPC1 and EPC2 to supply the full unbalanced currents and reactive power required within the microgrid.

5.6.3 Algorithm Performance

The algorithm's convergence performance has been assessed to verify its effectiveness. The assessment encompasses all the algorithm executions in all four cases considered.

Figure 5.10 shows the result. On the x-axis, the plot reports the number of iterations, with $k \in [0, 1000]$; on the y-axis, the plot reports the percentage of setpoints $\boldsymbol{x}$ that, after k iterations, are closer than a threshold ϵ_t to the ideal final solution $\boldsymbol{x}^*$ (i.e., the convergence value), over all the executions of the considered cases along the 24 h. The threshold ϵ_t is a given relative-error, computed as the 2-norm of the difference between the ideal final solution and the solution found after k iterations, divided by the 2-norm of the ideal final solution:

$$\varepsilon_{\%} = \frac{\|\boldsymbol{x}(k) - \boldsymbol{x}^*\|_2}{\|\boldsymbol{x}^*\|_2} \cdot 100 \tag{5.23}$$

Several thresholds are considered herein, namely, 5%, 1%, and 0.1%. Notably, after 200 iterations, the error is always below 5%, while after less than 400 iterations the error is always below 1%. It takes slightly more than 600 iterations to keep the error below 0.1%.

Moreover, the computational effort needed to run the algorithm has also been evaluated. Specifically, the proposed algorithm has been implemented in an Imperix® B-Board Pro™ control board [101], which embeds two 1 GHz ARM CPUs. The real-time execution rate has been set to 50 kHz, and is responsible for the local control task of regulating the converter output quantities by the grid-forming control method presented in [13], while the proposed algorithm runs at 1 Hz. The

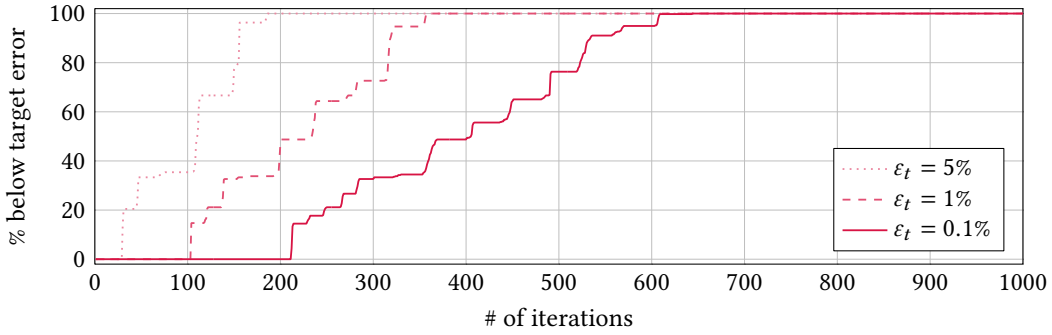

Figure 5.10: Convergence performance of the proposed algorithm. Percentage of intermediate solutions, after the indicated # of iterations, that are closer than the threshold ϵ_t to the ideal final solution (i.e., the convergence value).

timing analysis tool of the control platform reports an average usage of the controller of 39.94%, with a peak of 47.23%. This shows the method described herein can be, for instance, executed by the control board of one of the converters present in the considered microgrid alongside the local control tasks, without the need for a dedicated centralized control unit. Still, in applications, dedicated microgrid controllers may be available, as foreseen by relevant standards [34], and employed for running the optimization algorithm.

5.7 Toward a Distributed Implementation

In recent years, distributed control methods gained attention for their scalability and suitability for decentralized systems like microgrids. Unlike centralized approaches [86, 90], distributed control allows each converter to manage its operation autonomously while coordinating with neighboring units to achieve global objectives.

Compared to centralized approaches, distributed algorithms offer notable advantages in terms of system robustness and privacy. In centralized schemes, all data must be gathered at a central node, where a single large-scale optimization problem is solved. This architecture can create significant computational, memory, and communication bottlenecks as the number of agents grows. Distributed algorithms, such as the primal-dual method, allay these issues by decomposing the global problem into smaller sub-problems that are solved locally by each agent using only its own data and neighbor communications. This reduces the computational

burden on any single node and supports parallel execution, making the approach well-suited for systems with many geographically dispersed agents.

Still, distributed optimization is not without drawbacks. In some scenarios, centralized methods may achieve faster convergence since they avoid the per-iteration communication overhead inherent in distributed settings. While a centralized controller might solve the problem in a relatively smaller number of iterations with minimal latency, by communicating only at problem the start and end, this method requires message exchanges at every iteration. When communication delays accumulate over thousands of iterations, this can lead to longer total solution times.

Nonetheless, distributed approaches provide practical benefits in dynamic, decentralized environments such as energy communities, where scalability, fault tolerance, and data privacy are crucial. The choice between centralized and distributed optimization should be guided by the specific constraints and performance requirements of the application. One promising approach to distributed control is the distributed-consensus alternating-direction method of multipliers (DC-ADMM). DC-ADMM is well-suited for microgrid applications, as it facilitates consensus among units with limited communication, thereby reducing the computational burden and communication overhead associated with centralized control.

An alternative to the centralized solution to the problem considered that was presented in this chapter is possible using DC-ADMM to implement a distributed optimization algorithm such as [102], as done in [103].

5.7.1 Assumptions

The considered scenario is very similar to the one depicted in Figure 5.1. Here, the converters can communicate only among neighbouring units. The communication network is assumed to be an undirected connected graph, that is all the communication links are bidirectional, and given two nodes there always exists a path that joins them.

5.7.2 Distributed Formulation and Solution Method

Since the cost function (5.1) is the sum of separable terms, each one belonging to a different agent, the problem can be written in a distributed form:

$$\begin{cases} \min\limits_{\boldsymbol{x}_{i\,i\in\mathcal{V}}} & \sum\limits_{i=0}^{N_x} P^i_{\text{loss}}(\boldsymbol{x}_i) \\ \text{s.t.} & \sum\limits_{i=0}^{N_x} \boldsymbol{x}_i - \boldsymbol{g} = \boldsymbol{0}; \\ & \text{for } i = 1, \dots, N_x : \\ & \boldsymbol{x}_i^e \boldsymbol{A} \left(\boldsymbol{x}_i^e\right)^\top \leq I^2_{\text{max},i} \\ & \boldsymbol{x}_i^e \boldsymbol{B} \left(\boldsymbol{x}_i^e\right)^\top \leq I^2_{\text{max},i} \\ & \boldsymbol{x}_i^e \boldsymbol{C} \left(\boldsymbol{x}_i^e\right)^\top \leq I^2_{\text{max},i} \end{cases} \tag{5.24}$$

The pseudocode of solution method for this problem is reported in Algorithm 2. Lines 2 and 3 are the ones that optimize the Lagrangian of the problem and compute the optimal solution, lines 5 and 6 are computing and sending the information to the neighbors, while line 7 is making use of the information received from the neighbors.

Algorithm 2: Distributed algorithm implemented by i-th agent.

Data: $\boldsymbol{x}_i^0 \in \mathbf{R}^n$, $\lambda_i^0 \in \mathbf{R}^m$, $\boldsymbol{z}_{ij}^0 \in \mathbf{R}^{2m}\ \forall j \in \mathcal{N}_i$

1 **for** $t = 0, 1, \dots$ **do**

2 $\quad \begin{bmatrix} \hat{\alpha}_i^x(\boldsymbol{x}_i^t, \boldsymbol{z}_i^t) \\ \hat{\alpha}_i^\lambda(\lambda_i^t, \boldsymbol{z}_i^t) \end{bmatrix} = \frac{1}{1+\rho \deg_i} \left(\begin{bmatrix} A_i \boldsymbol{x}_i^t - b \\ \lambda_i^t \end{bmatrix} + \sum_{j\in\mathcal{N}_i} \boldsymbol{z}_{ij}^t \right);$

3 $\quad \begin{bmatrix} \boldsymbol{x}_i^{t+1} \\ \lambda_i^{t+1} \end{bmatrix} = \begin{bmatrix} \boldsymbol{x}_i^t \\ \lambda_i^t \end{bmatrix} - \gamma \begin{bmatrix} \nabla f_i(\boldsymbol{x}_i^t) + A_i^\top \hat{\alpha}_i^\lambda(\lambda_i^t, \boldsymbol{z}_i^t) \\ \kappa(\hat{\alpha}_i^\lambda(\boldsymbol{\lambda}_i^t, \boldsymbol{z}_i^t) - \lambda_i^t) + \hat{\alpha}_i^x(\boldsymbol{x}_i^t, \boldsymbol{z}_i^t) \end{bmatrix};$

4 $\quad$ **for** $j \in \mathcal{N}_i$ **do**

5 $\quad\quad \boldsymbol{m}_{ij}^t = -\boldsymbol{z}_{ij}^t + 2\rho \begin{bmatrix} \hat{\alpha}_i^x(\boldsymbol{x}_i^t, \boldsymbol{z}_i^t) \\ \hat{\alpha}_i^\lambda(\lambda_i^t, \boldsymbol{z}_i^t) \end{bmatrix};$

6 $\quad\quad$ transmit $\boldsymbol{m}_{ij}^t$ to j and receive $\boldsymbol{m}_{ji}^t$ from j;

7 $\quad\quad \boldsymbol{z}_{ij}^{t+1} = (1-\alpha)\boldsymbol{z}_{ij}^t + \alpha \boldsymbol{m}_{ji}^t;$

8 $\quad$ **end**

9 **end**

5.8 Conclusions

The approach presented in this chapter optimizes the provision of unbalanced and reactive currents, encompassing grid and converter losses. In a microgrid control hierarchy, the proposal can implement a control layer receiving input from other higher-level economic policies that define ancillary service setpoints and energy transactions and providing references to lower-level inner and primary controllers (e.g., droop-like controllers) of distributed electronic converters. Being able to effectively deal with quadratic (or even pseudo-quadratic, as in this case) cost functions, the proposed method can be an effective solution in a very wide class of different problems. Moreover, with its light computational cost, it may not even need a dedicated controller carrying out its control tasks, but could be run alongside other control tasks on a local controller.

5.9 Summary

In this chapter:

- a method for the minimization of power losses due to unbalanced and reactive currents is proposed, that includes grid and converter losses;
- the formulation of the optimization problem as a Lagrange multipliers problem is discussed;
- a solution algorithm based on the primal-dual method is presented;
- the benchmark employed for the validation is presented and discussed;
- the simulation results that validate the approach are shown.

Test Setup for the Validation of Microgrid Control Methods

6

This chapter presents a benchmark designed for the validation of microgrid control methods. It emulates a microgrid scenario with multiple power electronic devices, with configurable interconnections that facilitate the creation of different topologies. The presence of a communication network allows the exchange of information among all the converters plus an additional microgrid-level controller. In this way, the interactions among the devices and their control actions can be fully tested, as well as the interplay among the control layers, taking the validation a step further toward a holistic approach. Section 6.2 introduces the scenario considered for demonstrating the setup functionalities; Section 6.3 details the experimental setup; Section 6.4 discusses the implemented control strategies; Section 6.5 presents the experimental results.

6.1 Introduction

The increasing presence of grid-tied three-phase EPCs in modern power systems, with a wide range of control techniques, enables functionalities far beyond basic power regulation. These include unbalanced compensation—long established capability in grid-following converters and now achievable in grid-forming ones [12, 19, 20, 53, 72]—as well as inertia emulation and fault-ride-through. Such advanced control features are being leveraged at the distribution level to enhance system stability, improve power quality, and support energy management objectives.

In EPC-dominated grids, the interplay between multiple layers of control—ranging from local converter controllers (e.g., current, voltage, and power control) to system-level coordination—significantly influences microgrid behavior. Proper coordination among these controllers is essential for achieving robust, reliable operation. This chapter presents the development of an experimental validation setup for a converter coordination method aimed at providing grid services such as unbalanced current and reactive power compensation in an optimal manner, as proposed in [15] and presented in Chapter 5.

To this end, a flexible and realistic microgrid test bench has been implemented. The setup includes eight 22 kW converters—five operating on the microgrid side and three serving as dc sources—along with two additional 6 kW dc sources. Plausible

line impedance values are incorporated to emulate realistic operating conditions. The control system under test includes all the relevant loops, from current and voltage control to higher-level coordination. In addition to reporting the developed experimental validation setup, this chapter presents experimental results that validate the performance of the proposed control strategy. The flexibility of the setup enables future investigations, including the validation of other distributed control architectures.

6.2 Converter Coordination Method

The studied algorithm optimally coordinates the provision of unbalanced and reactive currents in the microgrid by regulating the contributions of dispatchable EPCs and the main grid to minimize power losses. Notably, it does not impose constraints on the active current, allowing it to fulfill energy-related tasks (e.g. maximum power-point tracking, among others). The scenario includes both dispatchable elements (i.e., EPCs and the grid emulator) and non-dispatchable units (i.e., loads and generators), as illustrated in Figure 6.1. The grid emulator represents the connection to the upstream grid and is assumed to be equipped with a measurement unit at the PCC. A centralized controller, which can be located, for example, at the PCC, runs the microgrid control algorithm.

The algorithm periodically receives operating points from EPC1, EPC2, and the grid emulator. Under the assumptions considered in Section 5.2.1, the operating point can be conveniently represented as a six-element vector:

$$\boldsymbol{x}_i = \left[I^{+}_{d,i}, I^{+}_{q,i}, I^{-}_{d,i}, I^{-}_{q,i}, I^{0}_{d,i}, I^{0}_{q,i} \right] \tag{6.1}$$

where $i = 0, 1, 2$, with $i = 0$ for the grid emulator. Each vector contains the dq-axis symmetric components representing the reactive, negative-sequence, and zero-sequence currents, as well as the active current delivered by each dispatchable unit, prior to optimization. The algorithm then executes an optimization process, iteratively minimizing the following cost function using a primal-dual optimization method:

$$F = \sum_{i=0,1,2} a_i \|\boldsymbol{x}_i\|_2^2 + b_i \|\boldsymbol{x}_i\|_2 + c_i \tag{6.2}$$

where the coefficients $[a_i, b_i, c_i]$ define the converters' power losses as a function of $\boldsymbol{x}_i$ [90]. Herein, the optimization process runs for 1000 iterations, after which the microgrid controller dispatches updated reference signals for reactive, negative-

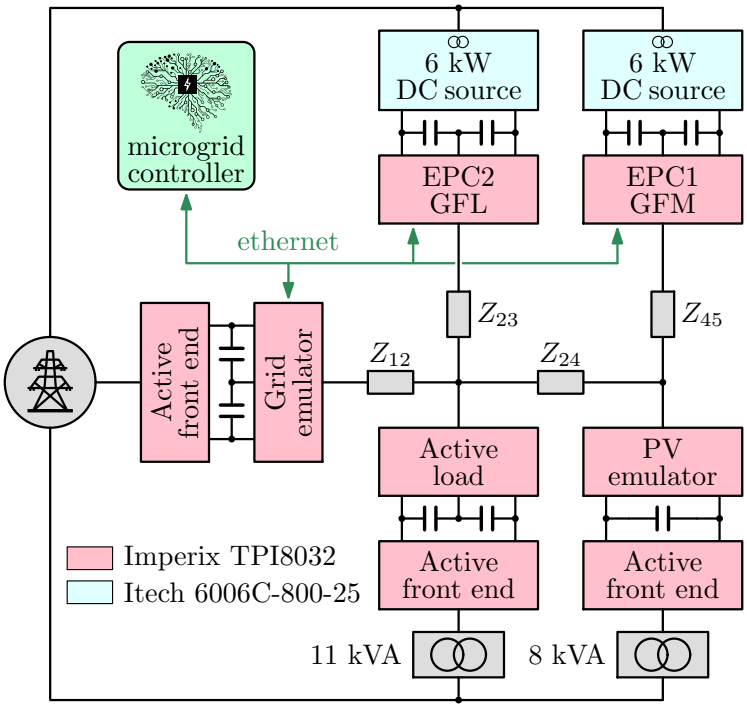

Figure 6.1: Validation scenario for the optimization algorithm. EPC1, EPC2, and the grid emulator are dispatchable units. Grey paths indicate communication lines.

sequence, and zero-sequence currents to EPC1 and EPC2. In practice, convergence occurs in fewer iterations, as demonstrated in Chapter 5.

The grid emulator acts as a slack bus and is treated as a dispatchable unit because adjusting the contributions of EPC1 and EPC2 implicitly determines its required contribution. The microgrid controller computes the emulator's reference values as the residual needed to satisfy the total compensation target, ensuring that the sum of dispatchable unit contributions matches the imbalance imposed by non-dispatchable units, based on Kirchhoff's current law. However, this value is not dispatched.

6.3 Description of the Experimental Setup

The experimental setup shown in Figure 6.2 is described in this section. To validate the algorithm, the benchmark must satisfy a set of requirements: *i)* reproduce a realistic microgrid scenario, with realistic line impedance values; *ii)* include both

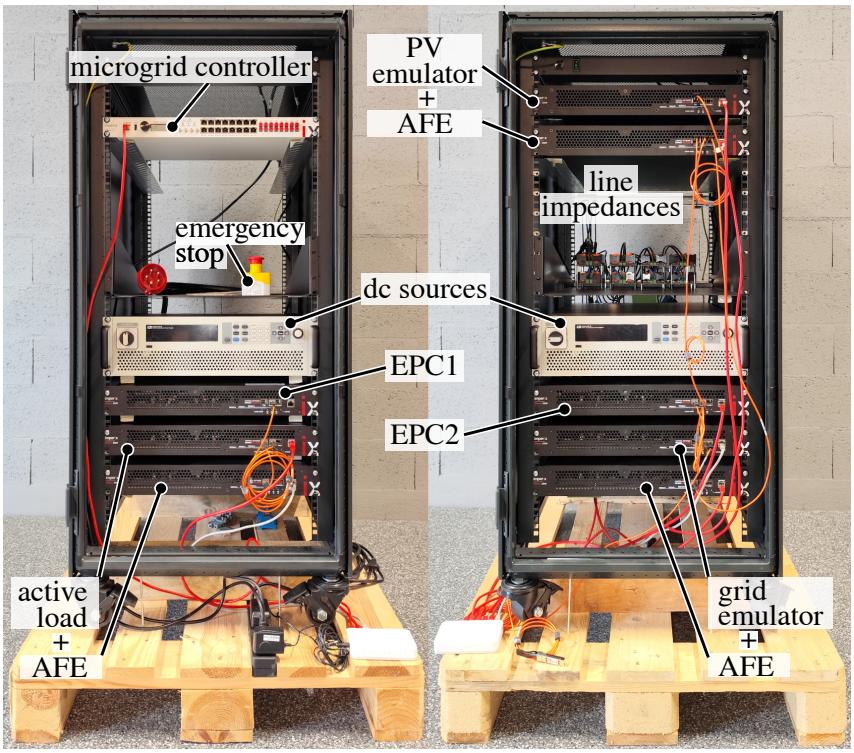

Figure 6.2: Proposed microgrid experimental setup, hosted in two cabinets.

dispatchable and non-dispatchable units; *iii)* include both grid-following and grid-forming converters.

6.3.1 Derivation of the Proposed Topology

The benchmark on European low-voltage distribution network presented in [55] serves as the foundation for the experimental setup. Given the availability of five converters on the microgrid side, the network topology from [55], illustrated in Figure 5.6, has been modified to yield the configuration shown in Figure 6.1. The existing loads have been aggregated into an active load that independently controls the absorbed power on each phase. The photovoltaic source has been retained, while the battery-interfacing converters are assigned to EPC1 and EPC2, which act as dispatchable units. A grid emulator is located at the PCC.

The line impedances Z_{12}, Z_{23}, Z_{24}, and Z_{45} are determined based on plausible line lengths, maintaining the same order of magnitude as those in Figure 5.6. The conductor types UG1 and UG2 are taken from the reference benchmark. Specifically,

Parameter	Value
Nominal line-to-neutral rms voltage	230 V
Nominal frequency	50 Hz
TPI8032 nominal power	22 kVA
TPI8032 nominal rms current	32 A
TPI8032 filter inductor	950 µH
TPI8032 output capacitor	12.9 µF
dc source nominal power	6 kW
Line impedances Z_{12}, Z_{24}	22 mΩ + 94 µH
Line impedances Z_{23}, Z_{45}	22 mΩ + 44 µH

Table 6.1: Parameters of microgrid benchmark in Figure 6.1

Z_{12} models the medium-to-low voltage transformer impedance plus a 100 m UG1 line, while Z_{24} corresponds to a 250 m UG1 line. Similarly, Z_{23} and Z_{45} represent 100 m UG2 lines. The impedance values have been rounded to match commercially available components and are listed in Table 6.1.

6.3.2 Devices and Hardware Elements

The experimental setup consists of two electrical domains, namely, the microgrid side and the main-grid side for the supply of the setup elements.

On the microgrid side, five TPI8032 converters [104] serve as the primary devices, as previously described. These are three-phase voltage source inverters rated 22 kVA with nominal rms current of 32 A.

On the main-grid side, three additional TPI8032 converters and two 6 kW dc sources [105] supply the dc buses that energize the microgrid-side devices. To avoid zero-sequence components exchange on the microgrid side through the active front ends, all the converters (except one, at most) are interfaced to the main grid through isolation transformers.

6.3.3 Management of the Zero-Sequence Components

A key challenge in the setup is managing the dc component of the zero-sequence current, whose control is critical for the regulation of the midpoint dc-link capac-

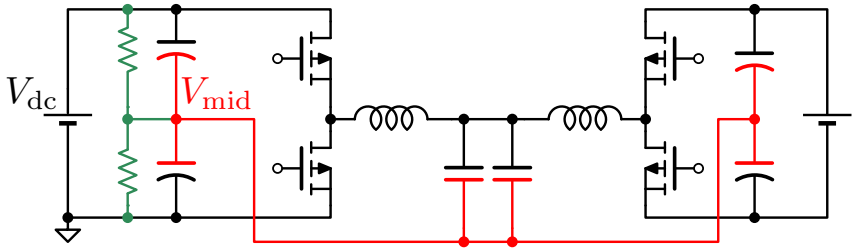

Figure 6.3: Simplified single-phase equivalent of two interconnected EPCs. The green balancing resistors are the only path for dc neutral-current flow.

itor voltages of the converters. However, since none of the TPI8032 converters include a fourth leg for zero-sequence current regulation, the neutral point remains galvanically isolated in dc, as illustrated in the simplified single-phase schematic in Figure 6.3.

As a result, the energy that balances one dc-link midpoint must come from another dc-link midpoint, unbalancing it. This makes simultaneous regulation of the midpoint voltage across all devices impossible. The solution is to provide an additional path for the zero sequence current, with balancing resistors in dc-link of the grid emulator, depicted in green in Figure 6.3. In this way, the converters can balance their midpoints sourcing energy from the midpoint of the grid emulator, which is in turn balanced by the resistors and left without any midpoint balancing loop. The selected resistance value is 10 kΩ.

6.3.4 Communication Network

All devices are connected to a shared Ethernet network, enabling communication between any pair of devices. However, since the algorithm under test relies on a centralized controller, only the communication channels between each dispatchable unit and the centralized controller are established herein. Data is exchanged periodically every 100 ms, ensuring that the algorithm, which runs every five seconds, always has up-to-date data available. An auxiliary network on SFP cables is used to propagate protection signals, and it can be potentially used for heavy and fast data exchange, if necessary.

6.4 Control of the Microgrid-Side Converters

This section describes the control strategies for the converters connected to the microgrid side. The related block schemes are displayed in Figure 6.4.

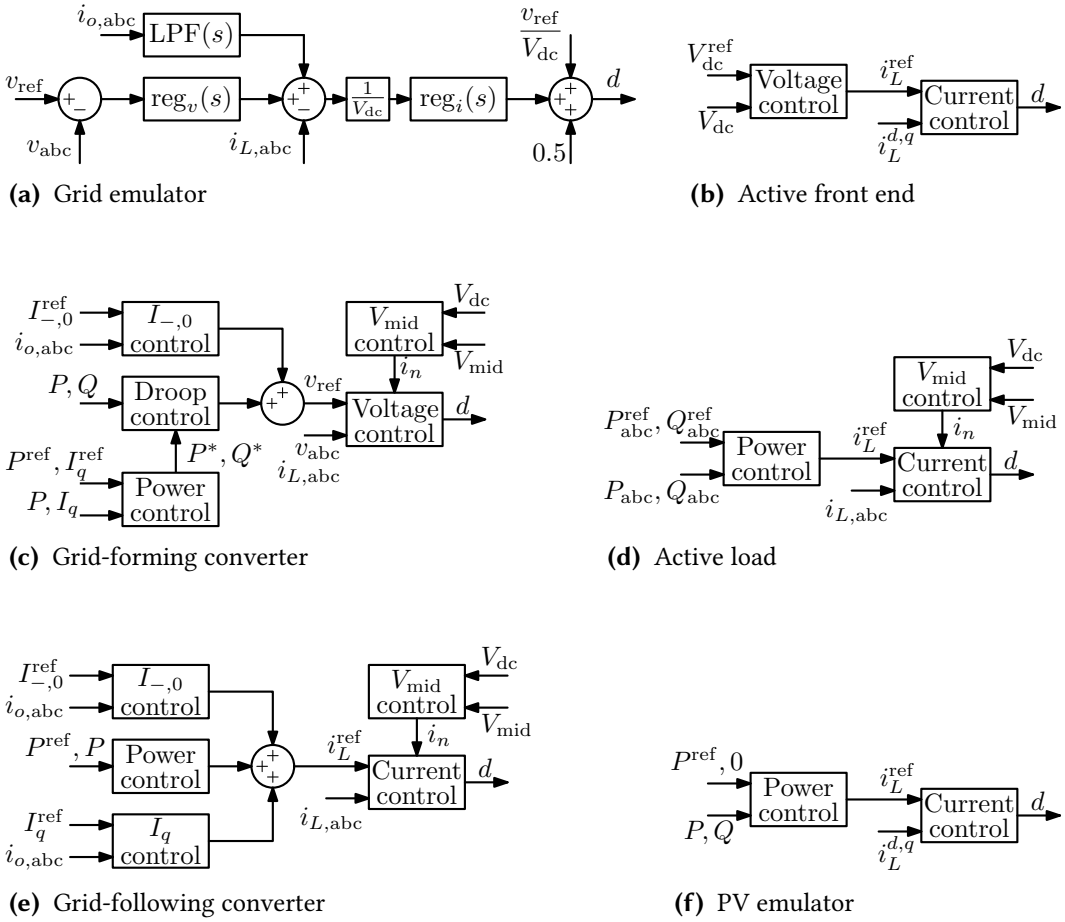

(a) Grid emulator

(b) Active front end

(c) Grid-forming converter

(d) Active load

(e) Grid-following converter

(f) PV emulator

Figure 6.4: Control schemes involved in the control of the converters system composing the experimental microgrid setup.

6.4.1 Grid Emulator

The grid emulator is controlled to behave as a stiff voltage source. A PI controller is used for current control. The voltage controller is implemented as a virtual admittance, following the approach in [106], and involves relevant considerations regarding the output impedance. Neglecting the interaction between the line impedances and the output capacitors of the converters may lead to undesired high-frequency resonances. This occurs when the voltage loop gain is unitary beyond the intended crossover frequency, resulting in an insufficient phase margin to dampen oscillations.

To mitigate this issue, the virtual admittance is designed as a series *R*-*L* circuit,

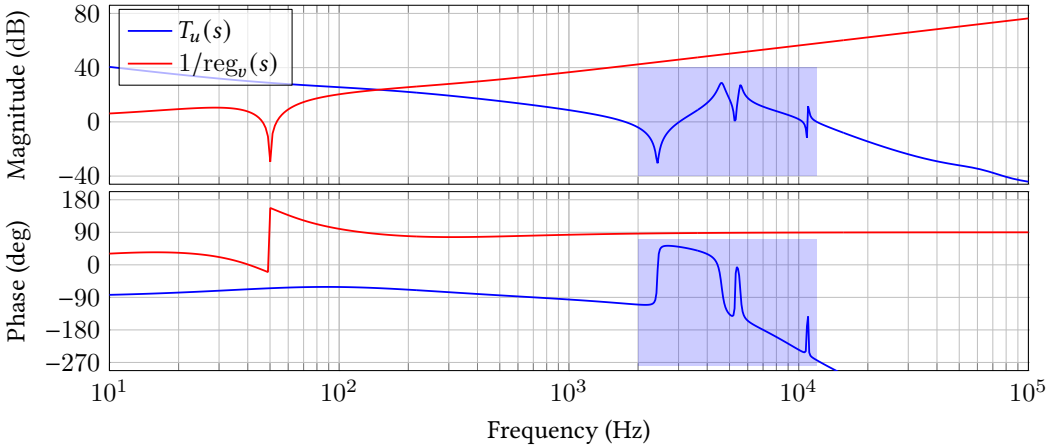

Figure 6.5: Bode plot of the uncompensated voltage loop gain (in blue), and the reciprocal of the voltage regulator transfer function (in red). The blue curve accounts for all the passive elements seen downstream the grid emulator's inductor, including the converters' output capacitors.

with a transfer function that tends to zero as frequency increases. A lead-lag compensator is applied around the crossover frequency to improve the phase margin. Additionally, a resonant term at the grid frequency is incorporated to minimize steady-state errors. The results of the design are shown in Figure 6.5, where no crossing is observed after the crossover frequency at about 150 Hz.

Notably, the phase margin at 150 Hz is approximately 30 deg, and its improvement would introduce one of the following drawbacks:

To improve control performance, feedforward of both the reference voltages and output currents is implemented. The voltage feedforward is achieved by adding the voltage reference, normalized by the dc-link voltage, to the output of the inductor current regulator, thereby reducing voltage regulation errors. The current feedforward is implemented by low-pass filtering the output currents and summing them with the current reference computed by the voltage control loop, which reduces the output impedance of the converter. The low-pass filter is employed to prevent high-frequency components from being fed-back, and a dc gain smaller than one (in this case, 0.8) is used to ensure the output impedance remains passive. This concept is clearly illustrated in Figure 6.6, which demonstrates that a gain smaller than one significantly reduces the active regions, represented by the shaded areas, of the output impedance as compared to unitary gain.

The overall control scheme is shown in Figure 6.4 (a).

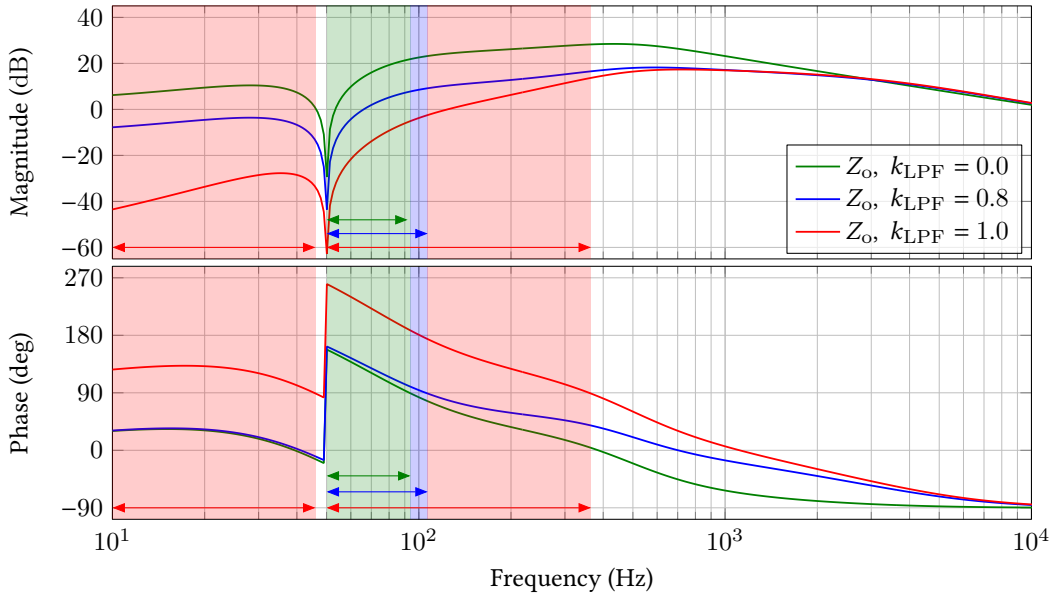

Figure 6.6: Grid emulator output impedance when the feed-forward of the output current is performed with unitary gain (red), with gain equal to 0.8 (blue), and without feed-forward (green). Optimal choice of k_{LPF} entails a suitable trade-off between magnitude of output impedance for regulation performance and width of the active region (shaded areas) for stability.

6.4.2 Grid-Forming Converter

The grid-forming converter implements the control strategy presented in [13] and discussed in Chapter 5, which is a droop-based controller that allows for the regulation of active and reactive power, as well as negative and zero-sequence currents.

The current controller uses a PI regulator, while the voltage controller is designed as a virtual admittance, similar to the grid emulator, emulating an *R-L* circuit. A PI regulator is employed to balance the dc-link capacitor voltages by measuring the midpoint voltage, comparing it to $V_{dc}/2$, and injecting neutral current as needed.

The droop controller is designed with a maximum frequency deviation of 0.5% and a maximum voltage amplitude deviation of 10%. The converter is powered by a dc source rated 6 kW, and its nominal power is assumed to be 5 kW, providing some headroom for the dc source to compensate for dc-link voltage oscillations caused by negative-sequence currents.

The outer loops regulate active power, reactive current, and negative and zero-sequence currents. Reactive currents are referred to instead of reactive powers

because they are the actual reference quantities dispatched by the microgrid controller. The reactive current control is still achieved by setting the reference value Q^* for the Q-V droop curve. The bandwidths are set to 0.3 Hz for active power, 1 Hz for reactive current, and 3 Hz for negative and zero-sequence currents.

Finally, initial synchronization with the voltage at the point of connection (PoC) of the converter is managed as described in [107], using the virtual admittance and the droop itself. The control scheme is illustrated in Figure 6.4 (c).

6.4.3 Grid-Following Converter

As commonly done in similar applications, the controller for the grid-following converter is composed of a PI regulator for the inductor current, an SRF-PLL for synchronization with the grid voltage, and PI regulators for output power and unbalanced currents.

Similar to the grid-forming controller, the midpoint voltage of the dc-link capacitors is set to $V_{dc}/2$ using a PI regulator. The control scheme is shown in Figure 6.4 (e).

6.4.4 Active Load

The active load operates by independently regulating active and reactive power at each phase. It uses the same current controller and PLL controller as the grid-following converter. The same power regulator is also employed, but it operates on the per-phase powers.

6.4.5 PV Emulator

The PV emulator is implemented in the dq reference frame and operates with a three-wire connection. It exchanges only positive-sequence components with the PoC. The emulator uses PI current controllers and a PI power regulator. The PLL employed is the same as the one used in the grid-following converter.

6.4.6 Active Front Ends

The active front ends implemented with the TPI8032 converters use the same current controller as the PV emulator. They are connected via a three-wire configuration. The dc-link voltage is regulated using a PI controller, which determines the amplitude and sign of the output current. The PLL used is the same as the one employed in the grid-following converter.

6.5 Experimental Validation

The experimental validation of the algorithm is carried out using a typical 24 h power profile for PV generation and the load absorptions. Specifically, the active load emulates three households with a single-phase connection. Their power profiles are generated using a Matlab® app [98], while the PV data is sourced from [96]. The profiles are shown in Figure 6.7.

The 24 h profile consists of 288 samples, each representing 5 min intervals. Herein power samples are reproduced at a higher pace, so that the entire dataset could be executed 12 times faster; the accelerated actual sampling time results 25 s. Acceleration is limited according to the slowest preserved dynamics of the original application, in this case, the converters' outermost control loops (i.e., power and unbalanced current loops) and the algorithm execution rate of once every 5 s. This means that multiple optimizations are performed at each operating point. This approach allows for the validation of the numerical stability of the algorithm and its robustness against non-idealities. In the equivalent original timescale, this corresponds to running the algorithm once every minute.

The algorithm has four different operating modes:

- **Mode 0**: the algorithm is inactive, and the grid emulator is the sole provider of reactive and unbalanced currents;
- **Mode 1**: the algorithm optimally shares the compensation effort for reactive and unbalanced currents;
- **Mode 2**: same as **Mode 1**, but with the constraint that no unbalanced currents are provided by the grid emulator;
- **Mode 3**: same as **Mode 2**, but with the constraint that no reactive current is provided by the grid emulator.

Figure 6.8 shows the experimental results of the algorithm. In particular, (a) shows the total power losses across all the different operating modes. (b) shows the relative variation in power losses of the different modes with respect to **Mode 0**. Finally, (b) and (c) show the unbalance factor and power factor computed in the different operating modes. The results show a peak reduction of power losses that exceeds 10%; they also validate the effectiveness of **Mode 2** and **Mode 3**: the unbalance factor goes to zero when operating in these two operating modes, while the power factor is unitary in **Mode 3**. What appears to be noise in the plots is actually caused by the delayed response of the microgrid controller to the variations

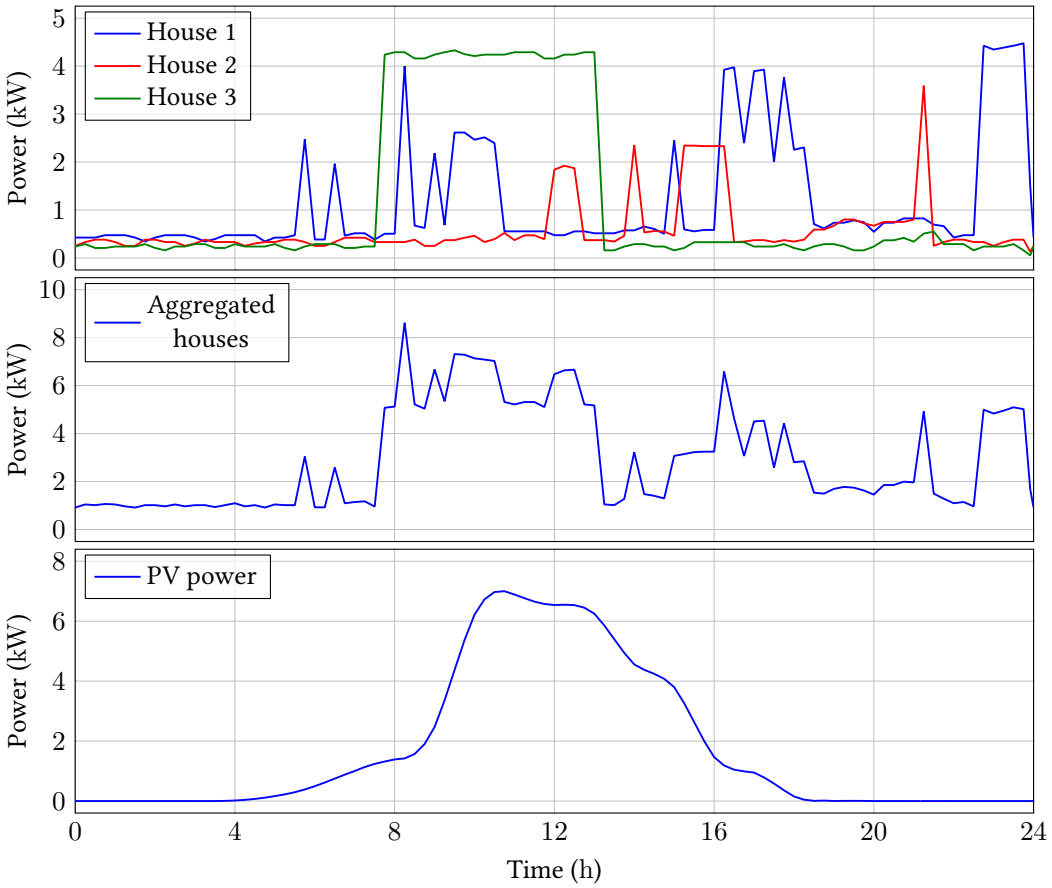

Figure 6.7: Electrical profiles used by the active load and the PV emulator in the experimental validation.

in the electrical profiles. Indeed, the microgrid controller needs to measure the new operating conditions before reacting to them.

Figure 6.9 shows the inductor currents of grid emulator, EPC1, and EPC2 while *i*) EPC1 and EPC2 absorb 2 kW of active power from the PoC, *ii*) the PV emulator injects 4 kW, and *iii*) the active load absorbs 2 kW on phase *a*, and 500 W on the other two phases. As expected, the grid emulator is subject to the highest unbalance in **Mode 0**, which is mitigated in **Mode 1**. In **Mode 2** and **Mode 3** the unbalanced components are provided solely by EPC1 and EPC2, thus the grid emulator injects only balanced currents. Remarkably, the active power output of all the units keeps unchanged across all the operating modes. Regarding the power losses for the operating point in Figure 6.9, **Mode 1** achieves a 3% reduction in the cost function

compared to **Mode 0**, consistently with the simulation results. In contrast, **Mode 2** and **Mode 3** exhibit a 3% increase in losses relative to **Mode 0**, due to additional constraints that restrict the solution space to higher-cost operating conditions. In the remaining part of the considered scenario, the algorithm could reduce the power loss due to the provision of grid services by up to 10%, when operating in **Mode 1**. Conversely, an increase of up to 5% was observed when running in **Mode 2** and **Mode 3**. Interestingly, EPC2 is contributing less than EPC1, because its cost function makes its use less favorable with respect to EPC1.

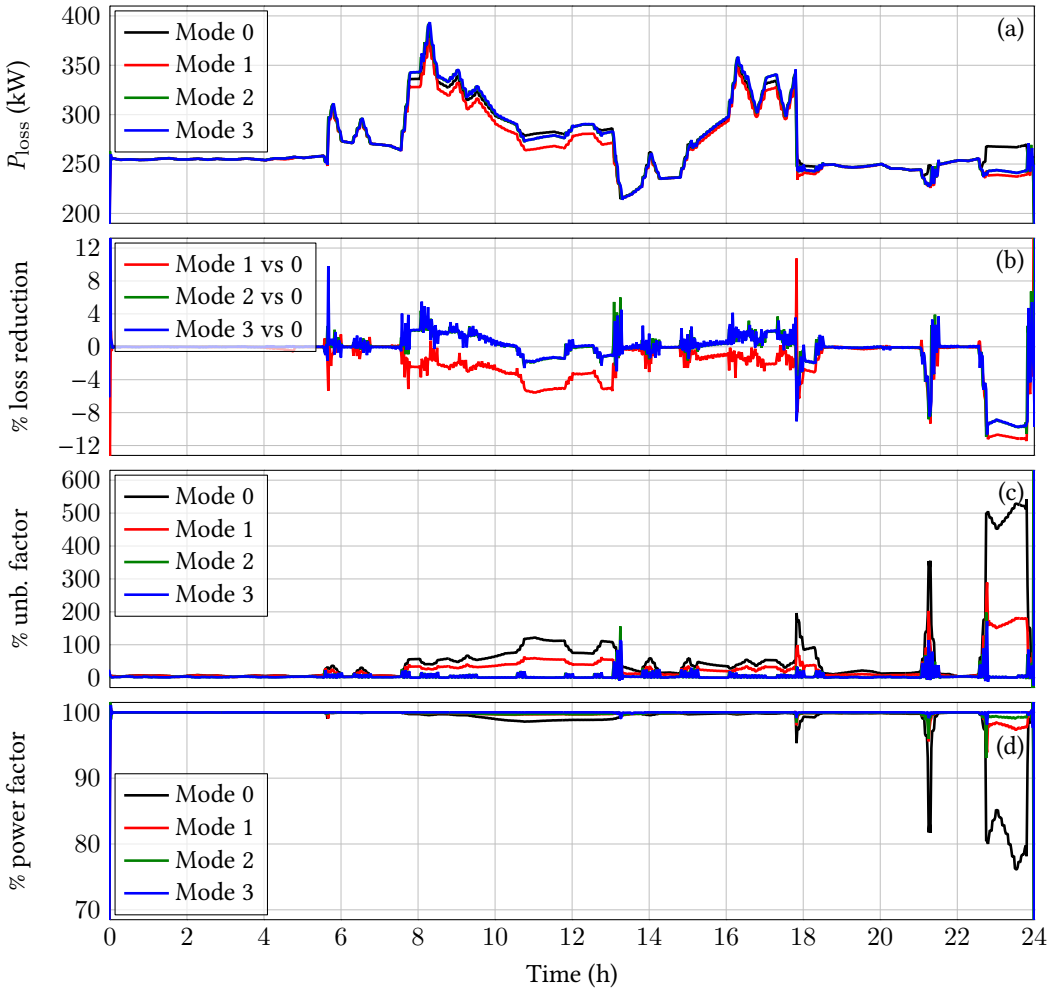

Figure 6.8: Experimental validation of the algorithm presented in Chapter 5.

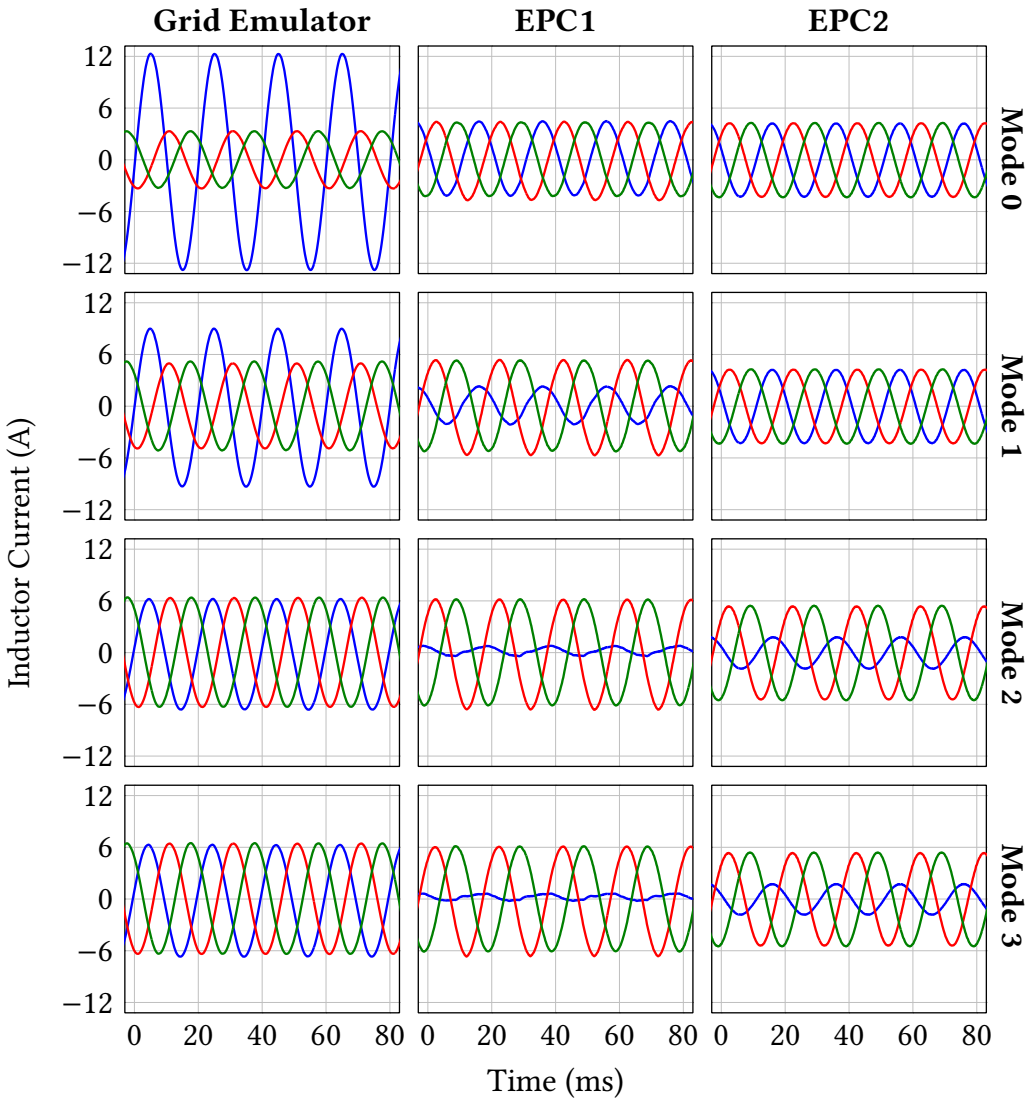

Figure 6.9: Experimental inductor current waveforms of dispatchable units, in a single operating point across all of the operating modes of the algorithm.

6.6 Conclusions

This chapter details the experimental infrastructure designed to validate a converter coordination strategy for the optimal provision of ancillary services in microgrids. The setup facilitates the emulation of a variety of grid conditions, with multiple converters operating in coordination. The optimal coordination algorithm for dis-

tributed electronic converters is outlined and experimentally validated through the presented setup. Its modular nature allows easy adaptation for testing of other control strategies or grid scenarios, such as low-voltage ride-through or microgrid islanding. By the developed dedicated setup the assessment of robustness and practical feasibility of the controller under real-world conditions was demonstrated. Practical implementation details, such as those related to communication, that are not easily captured in simulations, can accumulate and significantly impact validation results. In this case, for example, the need for filtering to extract fundamental-frequency quantities and the limitations of real converter control loops helped determine the practical upper limit of the algorithm's execution rate.

6.7 Summary

In this chapter:

- an experimental infrastructure for the validation of microgrid control methods is presented;
- the validation of the algorithm presented in Chapter 5 is performed using the proposed benchmark;
- the criteria followed during its conceptions have been outlined;
- the main challenges have been discussed;
- the experimental operation of the setup is shown and commented.

7 Conclusions & Outlook

This dissertation has addressed critical challenges in the integration of distributed energy resources within modern power systems, focusing on enhancing the control capabilities of GFM converters and developing coordination strategies for microgrid operation. The research work presented in this thesis contributes to the advancement of power electronics control techniques that are essential for the ongoing energy transition toward renewable energy sources and electrification. The primary contributions of this work can be summarized in four main areas.

Flexible Control of GFM Converters. This research successfully addressed the historical limitations of GFM converters in terms of control flexibility compared to their GFL counterparts. Through the development of two novel control approaches based on droop control techniques, this work has enabled GFM converters to achieve phase-by-phase power control and unbalanced current injection capabilities. These advancements represent a significant step toward bridging the gap between GFM and GFL converter functionalities, allowing GFM converters to maintain their inherent islanded operation capability while gaining the flexible control features traditionally associated with current-controlled converters.

Fault Ride-Through Capabilities. The research has tackled the critical challenge of maintaining system stability during adverse grid conditions for per-phase controlled GFM converters. The proposed fault ride-through methodology leverages the per-phase control capabilities to provide safe current limiting in both balanced and unbalanced fault scenarios while preventing transient instability and loss of synchronization. This contribution is particularly valuable as it allows GFM converters to support the grid during abnormal conditions.

Microgrid Optimization through Converter Coordination. This research has introduced a novel coordination method that optimizes microgrid operation by coordinating the reactive, negative, and zero sequence currents contributions between the converters in the microgrid and the main grid. This approach presents the significant advantage of achieving power losses minimization (and optional PCC currents balancing) without constraining the active power flow, which allows for seamless integration with other energy management strategies.

Comprehensive Experimental Validation. The establishment of an advanced experimental benchmark featuring 10 power electronics devices with programmable

controllers and flexible communication topologies provides a valuable platform for validating microgrid-level control approaches. This experimental setup addresses a significant gap in the literature where microgrid control methods are often validated using simplified converter models that do not capture the complex interactions between control loops and their impact on system performance.

Looking forward, technical contributions such as those presented in this work will become increasingly vital as power systems undergo fundamental transformation toward power-electronics-dominated, highly distributed architectures. The enhanced flexibility and fault ride-through capabilities of grid-forming converters will prove essential for maintaining grid stability and reliability as renewables increasingly share grid support responsibilities with traditional synchronous machines. Furthermore, the increasing reliance on electricity as an energy vector must be accompanied by solutions tackling the potential power quality issues. As the energy transition accelerates, these technical advances provide critical building blocks for more resilient, efficient, and economically viable distributed energy architectures that will define the future power grid.

A Appendix

Current-Limiting Constraints in Chapter 5

The matrices $\boldsymbol{A}, \boldsymbol{B}, \boldsymbol{C}$ used in (5.7) allow to obtain the squared absolute value of per-phase currents, namely $I^2_{a,i}, I^2_{b,i}, I^2_{c,i}$, from the vector $\boldsymbol{x}^e_i = \left[I^+_{d,i}, I^+_{q,i}, I^-_{d,i}, I^-_{q,i}, I^0_{d,i}, I^0_{q,i}\right]$. The derivation is simple but involves some calculations.

From symmetrical components, *abc* components can be obtained as:

$$\begin{bmatrix} \underline{I}_a \\ \underline{I}_b \\ \underline{I}_c \end{bmatrix} = \begin{bmatrix} 1 & 1 & 1 \\ \underline{a}^2 & \underline{a} & 1 \\ \underline{a} & \underline{a}^2 & 1 \end{bmatrix} \begin{bmatrix} \underline{I}^+ \\ \underline{I}^- \\ \underline{I}^0 \end{bmatrix}; \quad \underline{a} = e^{j\frac{2\pi}{3}} \tag{A.1}$$

where underline indicates complex quantities. By decomposing the symmetrical components in their *dq* components, from (A.1) one obtains:

$$\underline{I}_a = \underline{I}^+ + \underline{I}^- + \underline{I}^0 = I^+_d + I^-_d + I^0_d + j\left(I^+_q + I^-_q + I^0_q\right);$$

$$\begin{aligned} \underline{I}_b &= \underline{a}^2\underline{I}^+ + \underline{a}\,\underline{I}^- + \underline{I}^0 = \\ &= -\tfrac{1}{2}I^+_d + \tfrac{\sqrt{3}}{2}I^+_q - \tfrac{1}{2}I^-_d - \tfrac{\sqrt{3}}{2}I^-_q + I^0_d + \\ &+ j\left(-\tfrac{\sqrt{3}}{2}I^+_d - \tfrac{1}{2}I^+_q + \tfrac{\sqrt{3}}{2}I^-_d - \tfrac{1}{2}I^-_q + I^0_q\right); \end{aligned}$$

$$\begin{aligned} \underline{I}_c &= \underline{a}\,\underline{I}^+ + \underline{a}^2\underline{I}^- + \underline{I}^0 = \\ &= \tfrac{1}{2}I^+_d - \tfrac{\sqrt{3}}{2}I^+_q - \tfrac{1}{2}I^-_d + \tfrac{\sqrt{3}}{2}I^-_q + I^0_d + \\ &+ j\left(\tfrac{\sqrt{3}}{2}I^+_d - \tfrac{1}{2}I^+_q - \tfrac{\sqrt{3}}{2}I^-_d - \tfrac{1}{2}I^-_q + I^0_q\right); \end{aligned}$$

By squaring the absolute value of $\underline{I}_a, \underline{I}_b, \underline{I}_c$ one obtains the following expressions:

$$\begin{aligned}
I_a^2 &= (I_d^+)^2 + (I_q^+)^2 + (I_d^-)^2 + (I_q^-)^2 + (I_d^0)^2 + (I_q^0)^2 + \\
&\quad +2I_d^+I_d^- + 2I_d^+I_d^0 + 2I_q^+I_q^- + 2I_q^+I_q^0 + 2I_d^-I_d^0 + 2I_q^-I_q^0;
\end{aligned}$$

$$\begin{aligned}
I_b^2 &= (I_d^+)^2 + (I_q^+)^2 + (I_d^-)^2 + (I_q^-)^2 + (I_d^0)^2 + (I_q^0)^2 - \\
&\quad -I_d^+I_d^- - I_d^+I_d^0 - I_q^+I_q^- - I_q^+I_q^0 - I_d^-I_d^0 - I_q^-I_q^0 + \\
&\quad +\sqrt{3}I_d^+I_q^- - \sqrt{3}I_d^+I_q^0 - \sqrt{3}I_q^+I_d^- - \sqrt{3}I_q^+I_d^0 + \\
&\quad \sqrt{3} + I_d^-I_q^0 - \sqrt{3}I_q^-I_d^0;
\end{aligned}$$

$$\begin{aligned}
I_c^2 &= (I_d^+)^2 + (I_q^+)^2 + (I_d^-)^2 + (I_q^-)^2 + (I_d^0)^2 + (I_q^0)^2 - \\
&\quad -I_d^+I_d^- - I_d^+I_d^0 - I_q^+I_q^- - I_q^+I_q^0 - I_d^-I_d^0 - I_q^-I_q^0 + \\
&\quad -\sqrt{3}I_d^+I_q^- + \sqrt{3}I_d^+I_q^0 + \sqrt{3}I_q^+I_d^- + \sqrt{3}I_q^+I_d^0 - \\
&\quad \sqrt{3} - I_d^-I_q^0 + \sqrt{3}I_q^-I_d^0;
\end{aligned}$$

For the i-th controllable unit, the expressions of I_a^2, I_b^2, I_c^2 can be derived by

$$I_{x,i}^2 = \boldsymbol{x}_i^e \boldsymbol{X} \left(\boldsymbol{x}_i^e\right)^\top; \quad \boldsymbol{X} = \boldsymbol{A}, \boldsymbol{B}, \boldsymbol{C} \tag{A.2}$$

$$\boldsymbol{A} = \begin{bmatrix} 1 & 0 & 1 & 0 & 1 & 0 \\ 0 & 1 & 0 & 1 & 0 & 1 \\ 1 & 0 & 1 & 0 & 1 & 0 \\ 0 & 1 & 0 & 1 & 0 & 1 \\ 1 & 0 & 1 & 0 & 1 & 0 \\ 0 & 1 & 0 & 1 & 0 & 1 \end{bmatrix}; \quad \boldsymbol{B} = \begin{bmatrix} 1 & 0 & \frac{1}{2} & \frac{\sqrt{3}}{2} & \frac{1}{2} & -\frac{\sqrt{3}}{2} \\ 0 & 1 & -\frac{\sqrt{3}}{2} & \frac{1}{2} & \frac{\sqrt{3}}{2} & \frac{1}{2} \\ \frac{1}{2} & -\frac{\sqrt{3}}{2} & 1 & 0 & \frac{1}{2} & \frac{\sqrt{3}}{2} \\ \frac{\sqrt{3}}{2} & \frac{1}{2} & 0 & 1 & -\frac{\sqrt{3}}{2} & \frac{1}{2} \\ \frac{1}{2} & \frac{\sqrt{3}}{2} & \frac{1}{2} & -\frac{\sqrt{3}}{2} & 1 & 0 \\ -\frac{\sqrt{3}}{2} & \frac{1}{2} & \frac{\sqrt{3}}{2} & \frac{1}{2} & 0 & 1 \end{bmatrix}; \tag{A.3}$$

$$\boldsymbol{C} = \begin{bmatrix} 1 & 0 & \frac{1}{2} & -\frac{\sqrt{3}}{2} & \frac{1}{2} & \frac{\sqrt{3}}{2} \\ 0 & 1 & \frac{\sqrt{3}}{2} & \frac{1}{2} & -\frac{\sqrt{3}}{2} & \frac{1}{2} \\ \frac{1}{2} & \frac{\sqrt{3}}{2} & 1 & 0 & \frac{1}{2} & -\frac{\sqrt{3}}{2} \\ -\frac{\sqrt{3}}{2} & \frac{1}{2} & 0 & 1 & \frac{\sqrt{3}}{2} & \frac{1}{2} \\ \frac{1}{2} & -\frac{\sqrt{3}}{2} & \frac{1}{2} & \frac{\sqrt{3}}{2} & 1 & 0 \\ \frac{\sqrt{3}}{2} & \frac{1}{2} & -\frac{\sqrt{3}}{2} & \frac{1}{2} & 0 & 1 \end{bmatrix}$$

Bibliography

[1] Roberto Benato and Lorenzo Fellin. **Impainti Elettrici**. UTET, 2011 (see page 3).

[2] Frede Blaabjerg and Simon Round. *Power Electronics: Revolutionizing the world's future energy systems*. https://www.hitachienergy.com/news-and-events/perspectives/2021/08/power-electronics-revolutionizing-the-world-s-future-energy-systems. (Visited on 08/26/2021) (see page 3).

[3] IEA. **World Energy Outlook 2024**. Tech. rep. 2024 (see pages 3–5).

[4] IEA. **Integrating Solar and Wind**. Tech. rep. Sept. 2024 (see page 3).

[5] **What the duck curve tells us about managing a green grid**. Tech. rep. California ISO, 2015 (see page 4).

[6] Mostafa Farrokhabadi, Claudio A. Cañizares, John W. Simpson-Porco, Ehsan Nasr, Lingling Fan, Patricio A. Mendoza-Araya, Reinaldo Tonkoski, Ujjwol Tamrakar, Nikos Hatziargyriou, Dimitris Lagos, Richard W. Wies, Mario Paolone, Marco Liserre, Lasantha Meegahapola, Mahmoud Kabalan, Amir H. Hajimiragha, Dario Peralta, Marcelo A. Elizondo, Kevin P. Schneider, Francis K. Tuffner, and Jim Reilly. **Microgrid Stability Definitions, Analysis, and Examples**. *IEEE Transactions on Power Systems* 35:1 (Jan. 2020), 13–29. ISSN: 1558-0679. DOI: 10.1109/TPWRS.2019.2925703 (see page 4).

[7] Jose Ronaldo Silveira, Danilo Iglesias Brandao, Nicolas T.D. Fernandes, Wadaed Uturbey, and Braz Cardoso. **Multifunctional dispatchable microgrids**. *Applied Energy* 282 (2021), 116165. ISSN: 0306-2619. DOI: https://doi.org/10.1016/j.apenergy.2020.116165. URL: https://www.sciencedirect.com/science/article/pii/S0306261920315713 (see pages 4, 8).

[8] Augusto M. S. Alonso, Fernando P. Marafão, and Elisabetta Tedeschi. **Dispatchable Microgrids: An Extended Provision of Systemic Ancillary Services to Low-Voltage Distribution Grids**. *IEEE Access* 12 (2024), 76692–76706. ISSN: 2169-3536. DOI: 10.1109/ACCESS.2024.3406899 (see page 4).

[9] Francesco Simmini, Marco Agostini, Massimiliano Coppo, Tommaso Caldognetto, Andrea Cervi, Fabio Lain, Ruggero Carli, Roberto Turri, and Paolo Tenti. **Leveraging Demand Flexibility by Exploiting Prosumer Response to Price Signals in Microgrids**. *Energies* 13:12 (2020). ISSN: 1996-1073. DOI: 10.3390/en13123078. URL: https://www.mdpi.com/1996-1073/13/12/3078 (see pages 4, 8).

[10] Danilo I. Brandao, Willian M. Ferreira, Augusto M. S. Alonso, Elisabetta Tedeschi, and Fernando P. Marafão. **Optimal Multiobjective Control of Low-Voltage AC Microgrids: Power Flow Regulation and Compensation of Reactive Power and Unbalance**. *IEEE Transactions on Smart Grid* 11:2 (2020), 1239–1252. DOI: 10.1109/TSG.2019.2933790 (see page 4).

[11] Danilo I. Brandao, Tommaso Caldognetto, Fernando P. Marafão, Marcelo G. Simões, José A. Pomilio, and Paolo Tenti. **Centralized Control of Distributed Single-Phase Inverters Arbitrarily Connected to Three-Phase Four-Wire Microgrids**. *IEEE Transactions on Smart Grid* 8:1 (Jan. 2017), 437–446. ISSN: 1949-3061. DOI: 10.1109/TSG.2016.2586744 (see pages 4, 9).

[12] Andrea Lauri, Tommaso Caldognetto, Davide Biadene, Hossein Abedini, and Paolo Mattavelli. **Per-Phase Power Controller for Smooth Islanded Transitions in Three-Phase Three-Wire Systems**. *Energies* 16:2 (Jan. 2023), 672. ISSN: 1996-1073. DOI: 10.3390/en16020672. (Visited on 02/22/2023) (see pages 5, 21, 53, 76).

[13] Andrea Lauri, Tommaso Caldognetto, Davide Biadene, and Paolo Mattavelli. **An Unbalance and Power Controller Allowing Smooth Islanded Transitions in Three-Phase Microgrids**. *IEEE Transactions on Industrial Electronics* (2024), 1–11. ISSN: 1557-9948. DOI: 10.1109/TIE.2023.3347836. (Visited on 01/25/2024) (see pages 5, 43, 71, 84).

[14] Andrea Lauri, Tommaso Caldognetto, Davide Biadene, and Paolo Mattavelli. **Low-Voltage Ride Through of a Grid-Forming Converter using the Per-Phase Power Control**. In: *2024 Energy Conversion Congress & Expo Europe (ECCE Europe)*. Sept. 2024, 1–6. DOI: 10.1109/ECCEEurope62508.2024.10751888 (see page 6).

[15] Andrea Lauri, Tommaso Caldognetto, Ruggero Carli, Davide Biadene, and Paolo Mattavelli. **Ancillary Service Provision via Primal-Dual Based Coordination of Distributed Power Electronic Converters in Three-Phase Microgrids**. *IEEE Open Journal of Power Electronics* 5 (2024), 976–986. ISSN: 2644-1314. DOI: 10.1109/OJPEL.2024.3416339. (Visited on 09/09/2024) (see pages 6, 76).

[16] Shuang Xu, Yaosuo Xue, and Liuchen Chang. **Review of Power System Support Functions for Inverter-Based Distributed Energy Resources- Standards, Control Algorithms, and Trends**. *IEEE Open Journal of Power Electronics* 2 (2021), 88–105. ISSN: 2644-1314. DOI: 10.1109/OJPEL.2021.3056627 (see page 8).

[17] Hossein Abedini, Tommaso Caldognetto, Paolo Mattavelli, and Paolo Tenti. **Real-Time Validation of Power Flow Control Method for Enhanced Operation of Microgrids**. *Energies* 13:22 (Jan. 2020), 5959. ISSN: 1996-1073. DOI: 10.3390/en13225959. (Visited on 06/26/2023) (see pages 8, 22).

[18] Mohammad Hamidieh and Mona Ghassemi. **Microgrids and Resilience: A Review**. *IEEE Access* 10 (2022), 106059–106080. ISSN: 2169-3536. DOI: 10.1109/ACCESS.2022.3211511 (see page 8).

[19] Tommaso Caldognetto, Hossein Abedini, and Paolo Mattavelli. **A Per-Phase Power Controller for Smooth Transitions to Islanded Operation**. *IEEE Open Journal of Power Electronics* 2 (2021), 636–646. ISSN: 2644-1314. DOI: 10.1109/OJPEL.2021.3134714. (Visited on 01/05/2024) (see pages 8–10, 12, 15, 21, 43–45, 48, 53, 76).

[20] Enrique Espina, Mauricio Espinoza, and Roberto Cardenas. **Active Power Angle Droop Control per Phase for Unbalanced 4-Wire Microgrids**. In: *2017 IEEE Southern Power Electronics Conference (SPEC)*. Dec. 2017, 1–6. DOI: 10.1109/SPEC.2017.8333637 (see pages 8, 21, 53, 76).

[21] Baojin Liu, Zeng Liu, Jinjun Liu, Ronghui An, Haoyang Zheng, and Yidong Shi. **An Adaptive Virtual Impedance Control Scheme Based on Small-AC-Signal Injection for Unbalanced and Harmonic Power Sharing in Islanded Microgrids**. *IEEE Transactions on Power Electronics* 34:12 (Dec. 2019), 12333–12355. ISSN: 1941-0107. DOI: 10.1109/TPEL.2019.2905588 (see page 8).

[22] Seyed Mahdi Fazeli, Hew Wooi Ping, Nasrudin Bin Abd Rahim, and Boon Teck Ooi. **Individual-phase control of 3-phase 4-wire voltage–source converter**. *IET Power Electronics* 7:9 (2014), 2354–2364. DOI: https://doi.org/10.1049/iet-pel.2013.0973. eprint: https://ietresearch.onlinelibrary.wiley.com/doi/pdf/10.1049/iet-pel.2013.0973. URL: https://ietresearch.onlinelibrary.wiley.com/doi/abs/10.1049/iet-pel.2013.0973 (see page 8).

[23] Hao-Chun Hsu, Nien-Ting Chung, Yaow-Ming Chen, and Chih-Chao Hsu. **Grid Voltage Balancing Strategy Based on Per-Phase-Controlled Inverters**. In: *2021 IEEE International Future Energy Electronics Conference (IFEEC)*. Nov. 2021, 1–6. DOI: 10.1109/IFEEC53238.2021.9661897 (see pages 8, 9).

[24] Adrian Timbus, Marco Liserre, Remus Teodorescu, Pedro Rodriguez, and Frede Blaabjerg. **Evaluation of Current Controllers for Distributed Power Generation Systems**. *IEEE Transactions on Power Electronics* 24:3 (Mar. 2009), 654–664. ISSN: 1941-0107. DOI: 10.1109/TPEL.2009.2012527 (see pages 9, 21).

[25] Josep M. Guerrero, Juan C. Vasquez, José Matas, Luis García de Vicuna, and Miguel Castilla. **Hierarchical Control of Droop-Controlled AC and DC Microgrids—A General Approach Toward Standardization**. *IEEE Transactions on Industrial Electronics* 58:1 (Jan. 2011), 158–172. ISSN: 1557-9948. DOI: 10.1109/TIE.2010.2066534 (see page 9).

[26] Stefano Lissandron and Paolo Mattavelli. **A Controller for the Smooth Transition from Grid-Connected to Autonomous Operation Mode**. In: *2014 IEEE Energy Conversion Congress and Exposition (ECCE)*. Sept. 2014, 4298–4305. DOI: 10.1109/ECCE.2014.6953987 (see pages 9, 21).

[27] Ovidiu Ivanov, Bogdan-Constantin Neagu, Andrei-Ioan Nițu, and Mihai Gavrilaş. **An Improved Metaheuristic Algorithm for Load Balancing in LV Distribution Networks**. In: *2021 9th International Conference on Modern Power Systems (MPS)*. June 2021, 1–5. DOI: 10.1109/MPS52805.2021.9492680. (Visited on 12/04/2023) (see page 9).

[28] Ovidiu Ivanov, Bogdan-Constantin Neagu, Andrei Cibotărică, and Mihai Gavrilaş. **Multiobjective Prosumer Surplus Management for Optimal Microgrid Operation**. In: *2021 10th International Conference on ENERGY and ENVIRONMENT (CIEM)*. 2021, 1–5. DOI: 10.1109/CIEM52821.2021.9614729 (see page 9).

[29] Lenos Hadjidemetriou, Anastasis Charalambous, and Elias Kyriakides. **Control Scheme for Phase Balancing of Low-Voltage Distribution Grids**. In: *2019 International Conference on Smart Energy Systems and Technologies (SEST)*. Sept. 2019, 1–6. DOI: 10.1109/SEST.2019.8849069 (see page 9).

[30] Shangshu Guan, Shun Tao, and Yidan Song. **Application Research of IEEE Std.1459–2010 in Three-Phase Three-Wire System**. In: *2022 IEEE 6th Information Technology and Mechatronics Engineering Conference (ITOEC)*. Vol. 6. Mar. 2022, 511–515. DOI: 10.1109/ITOEC53115.2022.9734577 (see page 9).

[31] Danilo I. Brandao, Lucas S. Araujo, Augusto M. S. Alonso, Geovane L. dos Reis, Eduardo V. Liberado, and Fernando P. Marafão. **Coordinated Control of Distributed Three- and Single-Phase Inverters Connected to Three-Phase Three-Wire Microgrids**. *IEEE Journal of Emerging and Selected Topics in Power Electronics* 8:4 (Dec. 2020), 3861–3877. ISSN: 2168-6785. DOI: 10.1109/JESTPE.2019.2931122 (see pages 9, 21).

[32] Claudio Burgos-Mellado, Jacqueline Llanos, Enrique Espina, Doris Sáez, Roberto Cárdenas, Mark Sumner, and Alan Watson. **Single-Phase Consensus-Based Control for Regulating Voltage and Sharing Unbalanced Currents in 3-Wire Isolated AC Microgrids**. *IEEE Access* 8 (2020), 164882–164898. ISSN: 2169-3536. DOI: 10.1109/ACCESS.2020.3022488 (see page 9).

[33] Paolo Tenti and Tommaso Caldognetto. **Generalized Control of the Power Flow in Local Area Energy Networks**. *Energies* 15:4 (Jan. 2022), 1416. ISSN: 1996-1073. DOI: 10.3390/en15041416. (Visited on 06/26/2023) (see pages 9, 55).

[34] **IEEE Standard for the Specification of Microgrid Controllers**. *IEEE Std 2030.7-2017* (Apr. 2018), 1–43. DOI: 10.1109/IEEESTD.2018.8340204. (Visited on 04/30/2024) (see pages 9, 72).

[35] Karel De Brabandere, Bruno Bolsens, Jeroen Van den Keybus, Achim Woyte, Johan Driesen, and Ronnie Belmans. **A Voltage and Frequency Droop Control Method for Parallel Inverters**. *IEEE Transactions on Power Electronics* 22:4 (July 2007), 1107–1115. ISSN: 1941-0107. DOI: 10.1109/TPEL.2007.900456 (see page 10).

[36] Wei Yao, Min Chen, José Matas, Josep M. Guerrero, and Zhao-Ming Qian. **Design and Analysis of the Droop Control Method for Parallel Inverters Considering the Impact of the Complex Impedance on the Power Sharing**. *IEEE Transactions on Industrial Electronics* 58:2 (Feb. 2011), 576–588. ISSN: 1557-9948. DOI: 10.1109/TIE.2010.2046001 (see pages 10, 23).

[37] Qing-Chang Zhong and Dushan Boroyevich. **Structural Resemblance Between Droop Controllers and Phase-Locked Loops**. *IEEE Access* 4 (2016), 5733–5741. ISSN: 2169-3536. DOI: 10.1109/ACCESS.2016.2606348 (see pages 14, 22, 24).

[38] Mohammad B. Delghavi and Amirnaser Yazdani. **A Unified Control Strategy for Electronically Interfaced Distributed Energy Resources**. *IEEE Transactions on Power Delivery* 27:2 (Apr. 2012), 803–812. ISSN: 1937-4208. DOI: 10.1109/TPWRD.2011.2181430 (see pages 14, 27).

[39] Hirofumi Akagi, Edson H. Watanabe, and Mauricio Aredes. **Instantaneous Power Theory and Applications to Power Conditioning, 2nd Edition | Wiley**. Wiley-IEEE Press, Apr. 2017. (Visited on 12/18/2023) (see page 18).

[40] Paolo Tenti and Tommaso Caldognetto. **Integration of Local and Central Control Empowers Cooperation among Prosumers and Distributors towards Safe, Efficient, and Cost-Effective Operation of Microgrids**. *Energies* 16:5 (Jan. 2023), 2320. ISSN: 1996-1073. DOI: 10.3390/en16052320. (Visited on 06/26/2023) (see pages 20, 21, 55).

[41] Pierluigi Siano, Giuseppe De Marco, Alejandro Rolán, and Vincenzo Loia. **A Survey and Evaluation of the Potentials of Distributed Ledger Technology for Peer-to-Peer Transactive Energy Exchanges in Local Energy Markets**. *IEEE Systems Journal* 13:3 (Sept. 2019), 3454–3466. ISSN: 1937-9234. DOI: 10.1109/JSYST.2019.2903172 (see page 20).

[42] Mohsen Khorasany, Afshin Najafi-Ghalelou, and Reza Razzaghi. **A Framework for Joint Scheduling and Power Trading of Prosumers in Transactive Markets**. *IEEE Transactions on Sustainable Energy* 12:2 (Apr. 2021), 955–965. ISSN: 1949-3037. DOI: 10.1109/TSTE.2020.3026611 (see page 20).

[43] Sheetal Chandak and Pravat Kumar Rout. *Microgrids During the Outbreak of COVID-19 - IEEE Smart Grid*. https://smartgrid.ieee.org/bulletins/july-2020/microgrids-during-the-outbreak-of-covid-19. (Visited on 06/26/2023) (see page 20).

[44] Kumaraguru Prabakar. **Microgrids—Support for the electric grid during natural disasters [Essay]**. *IEEE Potentials* 42:1 (Jan. 2023), 51–52. ISSN: 1558-1772. DOI: 10.1109/MPOT.2014.2326073 (see page 20).

[45] Zunaib Ali, Nicholas Christofides, Lenos Hadjidemetriou, and Elias Kyriakides. **Diversifying the Role of Distributed Generation Grid-Side Converters for Improving the Power Quality of Distribution Networks Using Advanced Control Techniques**. *IEEE Transactions on Industry Applications* 55:4 (July 2019), 4110–4123. ISSN: 1939-9367. DOI: 10.1109/TIA.2019.2904678 (see page 21).

[46] Qing-Chang Zhong and Yu Zeng. **Universal Droop Control of Inverters With Different Types of Output Impedance**. *IEEE Access* 4 (2016), 702–712. ISSN: 2169-3536. DOI: 10.1109/ACCESS.2016.2526616 (see page 21).

[47] Masoud Karimi-Ghartemani, Sayed Ali Khajehoddin, Prasanna Piya, and Mohammad Ebrahimi. **Universal Controller for Three-Phase Inverters in a Microgrid**. *IEEE Journal of Emerging and Selected Topics in Power Electronics* 4:4 (Dec. 2016), 1342–1353. ISSN: 2168-6785. DOI: 10.1109/JESTPE.2016.2614956 (see pages 21, 43).

[48] Xin Meng, Zeng Liu, Haoyang Zheng, and Jinjun Liu. **A Universal Controller Under Different Operating States for Parallel Inverters With Seamless Transfer Capability**. *IEEE Transactions on Power Electronics* 35:9 (Sept. 2020), 9794–9812. ISSN: 1941-0107. DOI: 10.1109/TPEL.2020.2970971 (see page 21).

[49] Sayed Ali Khajehoddin, Masoud Karimi-Ghartemani, and Mohammad Ebrahimi. **Grid-Supporting Inverters With Improved Dynamics**. *IEEE Transactions on Industrial Electronics* 66:5 (May 2019), 3655–3667. ISSN: 1557-9948. DOI: 10.1109/TIE.2018.2850002 (see page 21).

[50] Vedantham Lakshmi Srinivas, Bhim Singh, and Sukumar Mishra. **Self-Synchronizing VSM With Seamless Operation During Unintentional Islanding Events**. *IEEE Transactions on Industrial Informatics* 16:9 (Sept. 2020), 5680–5690. ISSN: 1941-0050. DOI: 10.1109/TII.2019.2958735 (see page 21).

[51] Mahdi Ashabani and Jaesung Jung. **Synchronous Voltage Controllers: Voltage-Based Emulation of Synchronous Machines for the Integration of Renewable Energy Sources**. *IEEE Access* 8 (2020), 49497–49508. ISSN: 2169-3536. DOI: 10.1109/ACCESS.2020.2976892 (see page 21).

[52] Ritwik Ghosh, Narsa Reddy Tummuru, and Bharat Singh Rajpurohit. **Modified VOC Using Three Symmetrical Components for Grid-Supporting Operation During Unbalanced Grid Voltages and Grid-Forming Operation in Hybrid Single-Phase/Three-Phase Microgrid**. *IEEE Transactions on Industrial Electronics* 70:11 (Nov. 2023), 11276–11286. ISSN: 1557-9948. DOI: 10.1109/TIE.2022.3225839. (Visited on 11/15/2023) (see page 21).

[53] Ritwik Ghosh, Narsa Reddy Tummuru, and Bharat Singh Rajpurohit. **A New Virtual Oscillator-Based Grid-Forming Controller with Decoupled Control Over Individual Phases and Improved Performance of Unbalanced Fault Ride-Through**. *IEEE Transactions on Industrial Electronics* 70:12 (Dec. 2023), 12465–

12474. ISSN: 1557-9948. DOI: 10.1109/TIE.2023.3236069. (Visited on 11/14/2023) (see pages 21, 53, 76).

[54] Samrat Acharya, Mohamed Shawky El-Moursi, Amer Al-Hinai, Ameena Saad Al-Sumaiti, and Hatem H. Zeineldin. **A Control Strategy for Voltage Unbalance Mitigation in an Islanded Microgrid Considering Demand Side Management Capability**. *IEEE Transactions on Smart Grid* 10:3 (May 2019), 2558–2568. ISSN: 1949-3061. DOI: 10.1109/TSG.2018.2804954 (see page 22).

[55] Kai Strunz. **Benchmark Systems for Network Integration of Renewable and Distributed Energy Resources**. Tech. rep. 2009 (see pages 22, 66, 67, 79).

[56] Yunwei Ryan Li, Farzam Nejabatkhah, and Hao Tian. **Smart Hybrid AC/DC Microgrids: Power Management, Energy Management, and Power Quality Control**. Wiley-IEEE Press, Apr. 2023 (see page 23).

[57] J.M. Guerrero, Luis Garcia de Vicuna, J. Matas, M. Castilla, and J. Miret. **Output Impedance Design of Parallel-Connected UPS Inverters with Wireless Load-Sharing Control**. *IEEE Transactions on Industrial Electronics* 52:4 (Aug. 2005), 1126–1135. ISSN: 1557-9948. DOI: 10.1109/TIE.2005.851634 (see page 23).

[58] Jinwei He and Yun Wei Li. **Analysis, Design, and Implementation of Virtual Impedance for Power Electronics Interfaced Distributed Generation**. *IEEE Transactions on Industry Applications* 47:6 (Nov. 2011), 2525–2538. ISSN: 1939-9367. DOI: 10.1109/TIA.2011.2168592 (see page 23).

[59] Stefano Lissandron, Alessandro Costabeber, and Paolo Mattavelli. **A Generalized Method to Analyze the Small-Signal Stability for a Multi-Inverter Islanded Grid with Droop Controllers**. In: *2013 15th European Conference on Power Electronics and Applications (EPE)*. Sept. 2013, 1–10. DOI: 10.1109/EPE.2013.6634616 (see page 28).

[60] E.A.A. Coelho, P.C. Cortizo, and P.F.D. Garcia. **Small-signal stability for parallel-connected inverters in stand-alone AC supply systems**. *IEEE Transactions on Industry Applications* 38:2 (2002), 533–542. DOI: 10.1109/28.993176 (see page 28).

[61] Tommaso Caldognetto, Andrea Petucco, Andrea Lauri, and Paolo Mattavelli. **A Flexible Power Electronic Converter System with Rapid Control Prototyping for Research and Teaching**. *HardwareX* 14 (June 2023). ISSN: 2468-0672. DOI: 10.1016/j.ohx.2023.e00411. (Visited on 03/14/2023) (see pages 33, 51, 61).

[62] Kai Shi, Wentao Song, Peifeng Xu, Rongke Liu, Zhiming Fang, and Yi Ji. **Low-Voltage Ride-Through Control Strategy for a Virtual Synchronous Generator Based on Smooth Switching**. *IEEE Access* 6 (2018), 2703–2711. ISSN: 2169-3536. DOI: 10.1109/ACCESS.2017.2784846. (Visited on 02/29/2024) (see page 42).

[63] Roberto Rosso, Xiongfei Wang, Marco Liserre, Xiaonan Lu, and Soenke Engelken. **Grid-Forming Converters: Control Approaches, Grid-Synchronization, and Future Trends—A Review**. *IEEE Open Journal of Industry Applications* 2 (2021), 93–109. ISSN: 2644-1241. DOI: 10.1109/OJIA.2021.3074028. (Visited on 11/20/2023) (see page 42).

[64] Taoufik Qoria, François Gruson, Fréderic Colas, Xavier Kestelyn, and Xavier Guillaud. **Current Limiting Algorithms and Transient Stability Analysis of Grid-Forming VSCs**. *Electric Power Systems Research* 189 (Dec. 2020), 106726. ISSN: 03787796. DOI: 10.1016/j.epsr.2020.106726. (Visited on 02/07/2024) (see page 43).

[65] Han Deng, Yang Qi, Jingyang Fang, Yi Tang, and Vincent Debusschere. **A Robust Low-Voltage-Ride-Through Strategy for Grid-Forming Converters Based on Reactive Power Synchronization**. *IEEE Transactions on Power Electronics* 38:1 (Jan. 2023), 346–357. ISSN: 1941-0107. DOI: 10.1109/TPEL.2022.3204912. (Visited on 02/01/2024) (see page 43).

[66] Seyed Fariborz Zarei, Hossein Mokhtari, Mohammad Amin Ghasemi, and Frede Blaabjerg. **Reinforcing Fault Ride Through Capability of Grid Forming Voltage Source Converters Using an Enhanced Voltage Control Scheme**. *IEEE Transactions on Power Delivery* 34:5 (Oct. 2019), 1827–1842. ISSN: 1937-4208. DOI: 10.1109/TPWRD.2018.2844082 (see page 43).

[67] Roberto Rosso, Soenke Engelken, and Marco Liserre. **On The Implementation of an FRT Strategy for Grid-Forming Converters Under Symmetrical and Asymmetrical Grid Faults**. *IEEE Transactions on Industry Applications* 57:5 (Sept. 2021), 4385–4397. ISSN: 1939-9367. DOI: 10.1109/TIA.2021.3095025. (Visited on 02/29/2024) (see page 43).

[68] Zilin Li, Ka Wing Chan, Jiefeng Hu, and Siu Wing Or. **An Adaptive Fault Ride-Through Scheme for Grid-Forming Inverters Under Asymmetrical Grid Faults**. *IEEE Transactions on Industrial Electronics* 69:12 (Dec. 2022), 12912–12923. ISSN: 1557-9948. DOI: 10.1109/TIE.2021.3135641. (Visited on 02/29/2024) (see page 43).

[69] Mads Graungaard Taul, Xiongfei Wang, Pooya Davari, and Frede Blaabjerg. **Current Limiting Control With Enhanced Dynamics of Grid-Forming Converters During Fault Conditions**. *IEEE Journal of Emerging and Selected Topics in Power Electronics* 8:2 (June 2020), 1062–1073. ISSN: 2168-6785. DOI: 10.1109/JESTPE.2019.2931477. (Visited on 02/29/2024) (see page 43).

[70] Prasanna Piya, Mohammad Ebrahimi, Masoud Karimi-Ghartemani, and Sayed Ali Khajehoddin. **Fault Ride-Through Capability of Voltage-Controlled Inverters**. *IEEE Transactions on Industrial Electronics* 65:10 (Oct. 2018), 7933–7943. ISSN: 1557-9948. DOI: 10.1109/TIE.2018.2803765. (Visited on 02/29/2024) (see page 43).

[71] Anant Narula, Paul Imgart, Massimo Bongiorno, Mebtu Beza, Jan R. Svensson, and Jean-Philippe Hasler. **Voltage-Based Current Limitation Strategy to Preserve Grid-Forming Properties Under Severe Grid Disturbances**. *IEEE Open Journal of Power Electronics* 4 (2023), 176–188. ISSN: 2644-1314. DOI: 10.1109/OJPEL.2023.3246728 (see page 43).

[72] Reginaldo V. Ferreira, Sidelmo M. Silva, and Danilo I. Brandao. **Positive–Negative Sequence Synchronverter for Unbalanced Voltage in AC Grids**. *Journal of Control, Automation and Electrical Systems* 32:3 (June 2021), 711–720. ISSN: 2195-3899. DOI: 10.1007/s40313-021-00690-4. (Visited on 01/12/2024) (see pages 53, 76).

[73] Thaís M. Blasi, Thelma S. P. Fernandes, Alexandre R. Aoki, and Fabrício H. Tabarro. **Multiperiod Optimum Power Flow for Active Distribution Networks With Provisioning of Ancillary Services**. *IEEE Access* 9 (2021), 110371–110395. ISSN: 2169-3536. DOI: 10.1109/ACCESS.2021.3101419 (see page 53).

[74] Yijia Cao, Yi Tan, Canbing Li, and Christian Rehtanz. **Chance-Constrained Optimization-Based Unbalanced Optimal Power Flow for Radial Distribution Networks**. *IEEE Transactions on Power Delivery* 28:3 (July 2013), 1855–1864. ISSN: 1937-4208. DOI: 10.1109/TPWRD.2013.2259509 (see page 53).

[75] Sergio F. Contreras, Camilo A. Cortes, and Johanna M. A. Myrzik. **Optimal Microgrid Planning for Enhancing Ancillary Service Provision**. *Journal of Modern Power Systems and Clean Energy* 7:4 (July 2019), 862–875. ISSN: 2196-5420. DOI: 10.1007/s40565-019-0528-3 (see page 53).

[76] Stavros Karagiannopoulos, Jannick Gallmann, Marina González Vayá, Petros Aristidou, and Gabriela Hug. **Active Distribution Grids Offering Ancillary Services in Islanded and Grid-Connected Mode**. *IEEE Transactions on Smart Grid* 11:1 (Jan. 2020), 623–633. ISSN: 1949-3061. DOI: 10.1109/TSG.2019.2927299 (see page 53).

[77] Ampolu Maneesha and K. Shanti Swarup. **Stochastic Optimal Bidding Strategy for Energy and Ancillary Services in Microgrid**. *IEEE Transactions on Industry Applications* 57:6 (Nov. 2021), 5698–5705. ISSN: 1939-9367. DOI: 10.1109/TIA.2021.3112936 (see page 53).

[78] I. G. Marneris, A. V. Ntomaris, P. N. Biskas, C. G. Baslis, D. I. Chatzigiannis, C. S. Demoulias, K. O. Oureilidis, and A. G. Bakirtzis. **Optimal Participation of RES Aggregators in Energy and Ancillary Services Markets**. *IEEE Transactions on Industry Applications* 59:1 (Jan. 2023), 232–243. ISSN: 1939-9367. DOI: 10.1109/TIA.2022.3204863 (see page 53).

[79] Mohammed AM Messilem, Diego Deplano, Mauro Franceschelli, Elio Usai, and Ruggero Carli. **Distributed optimization for networks of battery energy storage systems in energy communities with shared energy incentives**. In: *2024 IEEE 20th International Conference on Automation Science and Engineering (CASE)*. IEEE. 2024, 2745–2751 (see page 53).

[80] Messilem A. Mohamed, Ruggero Carli, and Sandro Zampieri. **MPC-Based Centralised Power Control in EV Charging Station with Battery Storage System and PV Coordination**. In: *2024 European Control Conference (ECC)*. June 2024, 224–230. DOI: 10.23919/ECC64448.2024.10590967 (see page 53).

[81] Ahmad Nikpour, Abolfazl Nateghi, and Miadreza Shafie-Khah. **Stochastic-Risk Based Approach for Microgrid Participation in Joint Active, Reactive, and Ancillary Services Markets Considering Demand Response**. *IEEE Open Access Journal of Power and Energy* 10 (2023), 2–13. ISSN: 2687-7910. DOI: 10.1109/OAJPE.2022.3206495 (see page 53).

[82] C. Opathella, Ayman Elkasrawy, Amr A. Mohamed, and B. Venkatesh. **Optimal Scheduling of Merchant-Owned Energy Storage Systems With Multiple Ancillary Services**. *IEEE Open Access Journal of Power and Energy* 7 (2020), 31–40. ISSN: 2687-7910. DOI: 10.1109/OAJPE.2019.2952811 (see page 53).

[83] Yiwei Wu, Jian Shi, Gino J. Lim, Lei Fan, and Anahita Molavi. **Optimal Management of Transactive Distribution Electricity Markets With Co-Optimized Bidirectional Energy and Ancillary Service Exchanges**. *IEEE Transactions on Smart Grid* 11:6 (Nov. 2020), 4650–4661. ISSN: 1949-3061. DOI: 10.1109/TSG.2020.3003244 (see page 53).

[84] L. R. Araujo, D. R. R. Penido, S. Carneiro, and J. L. R. Pereira. **A Three-Phase Optimal Power-Flow Algorithm to Mitigate Voltage Unbalance**. *IEEE Transactions on Power Delivery* 28:4 (Oct. 2013), 2394–2402. ISSN: 1937-4208. DOI: 10.1109/TPWRD.2013.2261095 (see page 53).

[85] Daniele M. Ferreira, Danilo I. Brandao, Gilbert Bergna-Diaz, Elisabetta Tedeschi, and Sidelmo M. Silva. **Distributed Control Strategy for Low-Voltage Three-Phase Four-Wire Microgrids: Consensus Power-Based Control**. *IEEE Transactions on Smart Grid* 12:4 (July 2021), 3215–3231. ISSN: 1949-3061. DOI: 10.1109/TSG.2021.3065910 (see page 54).

[86] Sriparna Roy Ghatak, Surajit Sannigrahi, and Parimal Acharjee. **Multiobjective Framework for Optimal Integration of Solar Energy Source in Three-Phase Unbalanced Distribution Network**. *IEEE Transactions on Industry Applications* 56:3 (May 2020), 3068–3078. ISSN: 1939-9367. DOI: 10.1109/TIA.2020.2968046 (see pages 54, 72).

[87] Lexuan Meng, Fen Tang, Mehdi Savaghebi, Juan C. Vasquez, and Josep M. Guerrero. **Tertiary Control of Voltage Unbalance Compensation for Optimal Power Quality in Islanded Microgrids**. *IEEE Transactions on Energy Conversion* 29:4 (Dec. 2014), 802–815. ISSN: 1558-0059. DOI: 10.1109/TEC.2014.2363687 (see page 54).

[88] Stephen P. Boyd and Lieven Vandenberghe. **Convex Optimization**. Cambridge University Press, 2023. ISBN: 978-0-521-83378-3 (see pages 54, 58).

[89] Yajie Jiang, Yun Yang, Siew-Chong Tan, and Shu-Yuen Ron Hui. **Lagrange Multiplier-Based Optimization Control for Distribution Power Loss Minimization of Islanded Three-Phase AC Microgrids**. In: *2021 IEEE/IAS Industrial and Commercial Power System Asia (I&CPS Asia)*. July 2021, 489–494. DOI: 10.1109/ICPSAsia52756.2021.9621641. (Visited on 01/12/2024) (see page 54).

[90] Yajie Jiang and Yun Yang. **Dual Ascent Algorithm-Based Improved Droop Control for Efficient Operation of AC Microgrid**. *Frontiers in Electronics* 3 (2022). ISSN: 2673-5857. (Visited on 04/25/2023) (see pages 54, 59–61, 72, 77).

[91] Kasım Sinan Yıldırım, Ruggero Carli, Luca Schenato, and Marco Todescato. **A Distributed Dual-Ascent Approach for Power Control of Wireless Power Transfer Networks**. In: *2017 IEEE 56th Annual Conference on Decision and Control (CDC)*. Dec. 2017, 3507–3512. DOI: 10.1109/CDC.2017.8264173. (Visited on 01/12/2024) (see page 59).

[92] Stephen Boyd, Neal Parikh, Eric Chu, Borja Peleato, and Jonathan Eckstein. **Distributed Optimization and Statistical Learning via the Alternating Direction Method of Multipliers**. *Foundations and Trends® in Machine Learning* 3:1 (July 2011), 1–122. ISSN: 1935-8237, 1935-8245. DOI: 10.1561/2200000016. (Visited on 01/17/2024) (see page 59).

[93] J. A. Nelder and R. Mead. **A Simplex Method for Function Minimization**. *The Computer Journal* 7:4 (Jan. 1965), 308–313. ISSN: 0010-4620. DOI: 10.1093/comjnl/7.4.308. (Visited on 03/16/2023) (see page 59).

[94] Andrea Lauri, Tommaso Caldognetto, Ruggero Carli, Davide Biadene, and Paolo Mattavelli. **Dual-Ascent Optimization for the Provision of Ancillary Services in Three-Phase Low-Voltage Microgrids**. In: *2023 8th IEEE Workshop on the Electronic Grid (eGRID)*. Oct. 2023, 1–6. DOI: 10.1109/eGrid58358.2023.10380958. (Visited on 01/17/2024) (see page 59).

[95] Sulaiman A. Alghunaim and Ali H. Sayed. **Linear Convergence of Primal–Dual Gradient Methods and Their Performance in Distributed Optimization**. *Automatica* 117 (July 2020), 109003. ISSN: 0005-1098. DOI: 10.1016/j.automatica.2020.109003. (Visited on 01/26/2024) (see page 60).

[96] Ani Kannal. *Solar Power Generation Data*. https://www.kaggle.com/datasets/anikannal/solar-power-generation-data. (Visited on 04/04/2025) (see pages 66, 86).

[97] *Wind Turbine Scada Dataset*. https://www.kaggle.com/datasets/berkerisen/wind-turbine-scada-dataset. (Accessed on Dec 3, 2024) (see page 66).

[98] Daniel A. Broden, Kaveh Paridari, and Lars Nordstrom. **Matlab Applications to Generate Synthetic Electricity Load Profiles of Office Buildings and Detached Houses**. In: *2017 IEEE Innovative Smart Grid Technologies - Asia (ISGT-Asia)*. Auckland: IEEE, Dec. 2017, 1–6. ISBN: 978-1-5386-4950-3. DOI: 10.1109/ISGT-Asia.2017.8378371. (Visited on 12/19/2023) (see pages 66, 86).

[99] Fronius. *Technical Details - Fronius Symo 17.5*. Accessed: May 12, 2023. URL: https://www.fronius.com/it-it/italy/energia-solare/installatori-e-partner/dati-tecnici/tutti-i-prodotti/inverter/fronius-symo/fronius-symo-17-5-3-m (see pages 68, 69).

[100] Aurora. *PVI-12.5-OUTD Inverter Datasheet*. https://www.solarchoice.net.au/wp-content/uploads/Power-One-Aurora-pvi-10.0-12.5-outdoor-au.pdf. Accessed: September 17, 2025. 2010 (see pages 68, 69).

[101] *Inverter Control Board - B-Board PRO Converter Controller - Imperix*. https://imperix.com/products/control/inverter-control-board/. (Visited on 04/26/2024) (see page 71).

[102] A. Mohamed Messilem, Guido Carnevale, and Ruggero Carli. **Distributed Constraint-Coupled Optimization: Harnessing ADMM-consensus for robustness**. *IFAC-PapersOnLine* 59:4 (2025). 10th IFAC Conference on Networked Systems NECSYS 2025, 193–198. ISSN: 2405-8963. DOI: https://doi.org/10.1016/j.ifacol.2025.07.067. URL: https://www.sciencedirect.com/science/article/pii/S2405896325004136 (see page 73).

[103] A. Mohamed Messilem, Andrea Lauri, Guido Carnevale, Davide Biadene, Tommaso Caldognetto, and Ruggero Carli. **Ancillary Services through Coordinated Distributed Power Electronic Converters in Three-Phase Microgrids**. *IFAC-PapersOnLine* 59:9 (2025). 1st IFAC Workshop on Smart Energy System for efficient and sustainable smart grids and smart cities - SENSYS 2025, 333–338. ISSN: 2405-8963. DOI: https://doi.org/10.1016/j.ifacol.2025.08.159. URL: https://www.sciencedirect.com/science/article/pii/S2405896325007499 (see page 73).

[104] Imperix ltd. *TPI8032 22kW: All-in-one Programmable Inverter*. (Visited on 03/07/2024) (see page 80).

[105] ITECH. *IT6000C Bidirectional Programmable DC Power Supply*. Mar. 2025 (see page 80).

[106] Pedro Rodríguez, Costantino Citro, J. Ignacio Candela, Joan Rocabert, and Alvaro Luna. **Flexible Grid Connection and Islanding of SPC-Based PV Power Converters**. *IEEE Transactions on Industry Applications* 54:3 (May 2018), 2690–2702. ISSN: 1939-9367. DOI: 10.1109/TIA.2018.2800683. (Visited on 03/31/2025) (see page 82).

[107] Qing-Chang Zhong, Phi-Long Nguyen, Zhenyu Ma, and Wanxing Sheng. **Self-Synchronized Synchronverters: Inverters Without a Dedicated Synchronization Unit**. *IEEE Transactions on Power Electronics* 29:2 (Feb. 2014), 617–630. ISSN: 1941-0107. DOI: 10.1109/TPEL.2013.2258684. (Visited on 04/02/2025) (see page 85).